INVESTIGATION OF TIME-DIFFERENCE-OF-ARRIVAL LOCALIZATION METHOD FOR NON-LINE-OF-SIGHT SCENARIOS

A Dissertation

Presented to

the Faculty of the Department of Electrical and Computer Engineering

University of Houston

In Partial Fulfillment

of the Requirements for the Degree

Doctor of Philosophy

in Electrical Engineering

by

Mengna Yang

December 2016

INVESTIGATION OF TIME-DIFFERENCE-OF-ARRIVAL

LOCALIZATION METHOD FOR NON-LINE-OF-SIGHT SCENARIOS

_____

Mengna Yang

Approved:

_____

Chair of the Committee
David R. Jackson, Professor,
Electrical and Computer Engineering

Committee Members:

_____

Ji Chen, Professor,
Electrical and Computer Engineering

_____

Stuart A. Long, Professor,
Electrical and Computer Engineering

_____

Jeffery T. Williams,
Sandia National Laboratories

_____

Giles Auchmuty, Professor,
Mathematics

_____

Suresh K. Khator, Associate Dean,
Cullen College of Engineering

_____

Badrinath Roysam,
Professor and Chair,
Electrical and Computer Engineering

Acknowledgements

I would like to express my profound appreciation to my advisors, Prof. David R. Jackson and Prof. Ji Chen for their continuous support of my Ph.D. study and related research, for their patience, encouragement, and immense knowledge. They have been tremendous mentors for me, both in my academic study and daily life. I feel extremely fortunate to work with such eminent professors, and I could never imagine having better advisors and mentors in my life.

A special thanks go to the sponsor of this project at Sandia National Laboratories, Dr. Jeffery T. Williams, who first suggested this project and then helped tremendously by collaborating on the research and design, and in conducting the experiment. His innovative and valuable suggestions have also significantly improved the quality of my dissertation.

I would also like to thank the rest of my committee, Dr. Stuart A. Long and Dr. Giles Auchmuty, for their insightful comments and inspiration, but also for the questions and comments that they offered along the way that gave me the incentive to widen my research from various perspectives. I offer my sincere appreciation for the learning opportunities provided by my committee.

I would also like to thank my dear friends Qi Zeng, Xinyu Liu, Dr. Zubiao Xiong, Jingshen Liu, Dr. Sohini Sengupta, Dr. Krishna Kota, and all the lab-mates in W301, W444, and W442, for their unending support and insightful discussions related to the research.

Last but not least, I want to thank my parents, Shiwu Yang and Suping Zhang, for their endless love and spiritual support. Thanks to my grandma, Shiqing Geng, for raising

me up and loving me more than anyone else. Thanks to my sister, Mengmeng Yang, for her spiritual communications and devout prayers for me. Thanks to my fiancé, Jiajun Jiang, and my future parents-in-law, Weimin Jiang, and Shengxia Lei, for their powerful inspiration and patience. Without the love from my loving family and friends, I would never have been able to conquer all of the difficulties and be a better me.

Thanks to my Lord, for letting me persist through all the difficulties. You have taught me how to treasure my brothers and sisters, and live within Your Spirit. I have experienced Your guidance day by day, and I want to love You and believe in You for the rest of my life.

INVESTIGATION OF TIME-DIFFERENCE-OF-ARRIVAL LOCALIZATION METHOD FOR NON-LINE-OF-SIGHT SCENARIOS

An Abstract

of a

Dissertation

Presented to

the Faculty of the Department of Electrical and Computer Engineering

University of Houston

In Partial Fulfillment

of the Requirements for the Degree

Doctor of Philosophy

in Electrical Engineering

by

Mengna Yang

December 2016

Abstract

A novel localization concept, which considers non-line-of-sight (NLOS) propagation, is proposed in this dissertation. By introducing a transfer function that relates the field at a given receiver to the source as a function of frequency and position, the NLOS effects can be mitigated and the propagation channel can be calibrated back to free space.

The conventional Time Difference of Arrival (TDOA) method under Line-of-Sight (LOS) and noisy conditions is implemented first, and then the theory is extended to the proposed method, which de-embeds the transfer function and extends the TDOA method to account for NLOS effects. A global search method and an iterative method are both introduced, based on the concept of de-embedding the transfer function. This involves using processed received signals (received signals after de-embedding the corresponding transfer functions). The localization accuracy achieved using the iterative method for various NLOS scenarios is investigated, including a refraction problem, a near field problem, and a scattering problem.

Subsequently, the study is further extended to allow for multiple reflection effects. Three different models are provided. First, a parallel-wall model considers the case when the reflections are basically coming from a single horizontal direction. A 3D localization model and 2D enclosed wall model are then also presented to illustrate cases when the reflections come from either the vertical or the two horizontal directions. A hybrid iterative method, combining the iterative method and the global search method, is proposed to solve the problem of convergence that occurs when the transmitted signal is

operating at high frequencies (so that the enclosed area of interest is large compared with a wavelength), especially with a narrow frequency bandwidth.

Simulation results demonstrate that the proposed algorithm performs much better than the usual TDOA localization method, and the accuracy is only limited by the sampling frequency. An experiment (performed at Sandia National Laboratories) is set up to verify the improvement in using the proposed method vs. the usual TDOA method.

Table of Contents

List of Figures

List of Tables

Chapter 1

Introduction

1.1 Background and Motivation

The wireless positioning (localization) problem has been addressed in recent years within a wide range of military and civilian applications using wireless sensor networks. The general problem consists of trying to localize accurately the position of a radiating source (often called the “target”) by means of signals recorded at various sensors (receivers) located in space. The signals recorded from the radiating source at the receivers are used to estimate the location of the source.

Surveys of the various techniques and applications for wireless positioning can be found in [1]-[4]. With precise position estimation, a variety of applications and services, such as enhanced-911, health/traffic monitoring, improved fraud detection, vehicle tracking, and inventory management can become achievable for cellular networks [2]. In addition, wireless networked sensors have a broad spectrum of applications in the defense area, generating new competencies for reconnaissance and surveillance, as well as other strategic applications [4].

Wireless techniques in wireless sensor network localization can be generally classified into three categories [5]: Angle-of-Arrival (AOA) measurements [6]-[8], distance-related measurements [9]-[21], and Received-Signal-Strength (RSS) profiling-based techniques [22]-[24]. Distance-related measurements are further categorized into one-way propagation time [9]-[11] and roundtrip propagation time measurements [12]-[13], connectivity measurements [14]-[15], RSS-based distance measurements [16]-[17],

the lighthouse approach [18] and time-difference-of-arrival (TDOA) measurements [19]-[21]. The localization algorithm proposed in this dissertation is based on the TDOA method. Chapter 2 discusses the principle of the TDOA method and how it is implemented.

1.2 Review of Localization Algorithms for Non-Line-of-Sight Scenarios

A common problem in many localization techniques is that non-line-of-sight (NLOS) errors can arise when either the line-of-sight (LOS) between the transmitter and the receivers is obstructed, perhaps by a building or other obstacle, or when the LOS measurements are contaminated by refracted, reflected and/or diffracted signals, as shown in Fig. 1.1. In general, the NLOS definition can even be broadly extended to include the effects of near-field transmission, where the transmitting signal is not propagating at the speed of light. Compared with LOS errors, NLOS errors are typically recognized as much more significant [25]-[26]. A field test has demonstrated that the average NLOS range error can be as large as 0.589 km in an IS-95 code-division multiple access (CDMA) system [27].

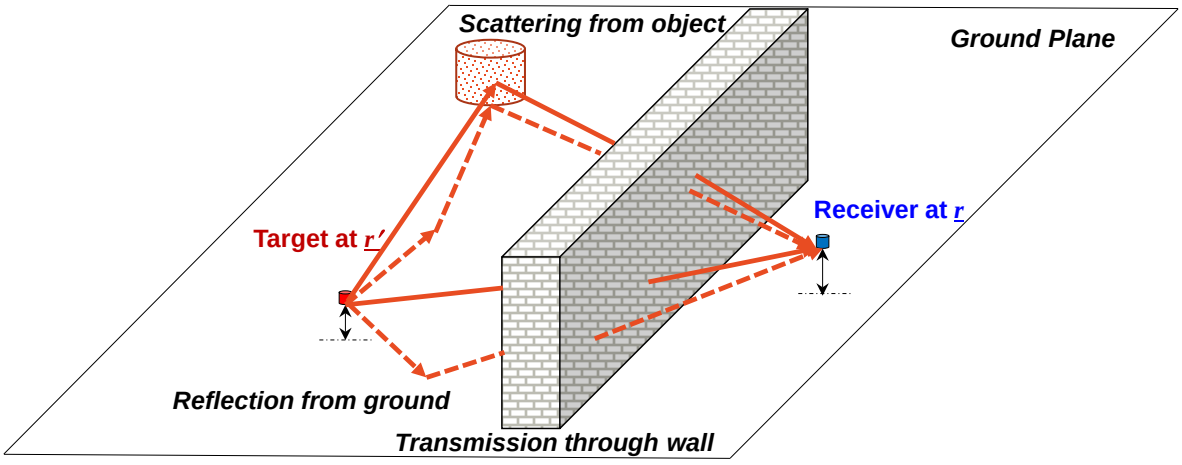

Figure 1.1. A radiating target is within an NLOS environment.

Various approaches have been proposed to protect location estimates from NLOS error corruption. Basically, NLOS methods are classified into NLOS identification, mitigation and localization techniques [28]. Comprehensive overviews can be found in [29], [30].

In essence, NLOS identification is a statistical detection problem, where NLOS and LOS are two hypotheses. The main task is to find out metrics and enable a binary hypothesis test so that NLOS and LOS conditions can be differentiated. After differentiation, the localization accuracy can be improved by removing the NLOS base nodes and incorporating only LOS nodes [31]-[33].

Identification techniques can be divided into three groups: i) those based on range statistics; ii) those based on channel characteristics (received signal power, Rician K factor, and so on); and iii) hybrid approaches that explore the consistency between time-of-arrival (TOA) measurement and path loss for LOS/NLOS. Typically, NLOS identification techniques can be further classified into cooperative, which are based on multi-node channel measurements, and non-cooperative, which are based on single node channel measurements [34].

Cong and Zhuang [31] proposed a typical cooperative approach that takes into account the fact that an NLOS error is always positive. Based on the assumption that an LOS error is Gaussian-distributed, the residual ei is calculated by a function containing the TDOA between different base nodes and the square root of the measurement noise variance. The higher the residual, the more likely the signal is biased by NLOS errors. A threshold is defined, and compared with the residual. If the base node's residual is larger than the threshold, the node would be labeled as an NLOS base node.

Yarkan and Arslan [32] proposed an algorithm to identify the existence of LOS propagation for time-varying, frequency selective radio channels for coherent receivers. Using coherent reception algorithms, the channel and delay acquisition estimates are provided, and the identification algorithm is then performed, comparing second-order statistical characteristics (autocorrelation coefficients) of underlying processes in channel taps.

Xu [33] proposed an NLOS identification technique that utilizes the statistics of the phase difference across two antenna elements. Based on the assumption that the phases received across the two antenna elements are uncorrelated, the channel Rician K-factor is a function of the phase difference variance, which is calculated by a phase-wrapping selection algorithm. By exploiting the K-factor distribution, a threshold is derived and the NLOS can be efficiently distinguished from the LOS scenarios. The performance of the proposed phase-difference-based K estimator is compared with that of the envelope-based K estimator.

Approaches using localization techniques often include received signal strength indicator (RSSI) [35], bidirectional TOA-DOA fusion [36], and single-base node TOA-DOA fusion with the assistance of the environment map [37], and multi-node TOA-DOA fusion [38]. Localization techniques can also be classified into cooperative and non-cooperative.

Konrad and Matt [35] present a robust, decentralized approach to RF-based location tracking called MoteTrack. The location of each mobile node is computed using a received radio signal strength signature from numerous beacon nodes to a database of signatures that is replicated across the beacon nodes themselves.

Seow and Tan [36] presented a comprehensive NLOS localization scheme and a least-square estimator that leverages on the bidirectional estimation of the angle of arrival (AOA) and time of arrival (TOA) of signals between mobile and reference devices. The proposed scheme needs two or more either LOS or NLOS multipath signals. It has been proven that multiple-bound scattering can be efficiently discarded by the multipath selection scheme so that a one-bound scattering NLOS signal can be utilized.

Song et al. [37] proposed a localization scheme based on the unitary ESPRIT (UESPRIT) algorithm using back ray tracing techniques with the assistance of city electronic maps. The UESPRIT algorithm is utilized to estimate the direction of arrival (DOA) and time of arrival (TOA). With the estimated angles and lengths of the signal paths, the back ray tracing technique emits signals from the receiver, then the transmitting waves move forward, and do not stop until the path lengths reach the estimated ones. The stop positions are the source locations and the final estimated target position is the average of those.

Wang and Zakavat [38] presented an omnidirectional mobile target-node (TN) localization technique for NLOS scenarios. It is assumed that the proposed system has two types of nodes: base nodes (BNs) and target nodes (TNs). The basic idea is that TNs cooperate with BNs to allow BNs to find their position in NLOS environments based on DOA and TOA. This technique demands the determination and localization of the reflection points that are shared between BNs and TNs.

NLOS mitigation methods usually attempt to compensate for the positive bias introduced by the NLOS scenarios. These methods can be roughly classified into four

categories: maximum likelihood (ML) [39], least squares [40], and constrained optimization [41], as well as robust statistics [42].

Gven et al. [39] proposed an NLOS identification technique based on the amplitude, captured by kurtosis, and delay statistics of UWB channels, evaluated by the mean excess delay and the root-mean-square (RMS) delay spread of the received multipath components. Based on the IEEE 802.15.4a UWB channel models, three different weighted least-squares localization techniques that are used to exploit the statistics of multipath components are investigated.

Chan and Ho [40] proposed a localization technique based on intersections of hyperbolic curves defined by TDOA. With more than three sensors, the TDOA equations are composed into set of equations that are linear and have an extra variable. Then, after an initial solution is given by a weighted linear least squares method, a second weighted least squares gives a more accurate estimated target position by utilizing the known constraints between the source coordinate and the extra variable.

Wang, Wang and O'Dea [41] proposed a location algorithm to reduce the induced error from NLOS scenarios. Mathematical programming is used to find the maximum likelihood estimate of the target position in a restricted domain, which is defined by the inequalities induced by the NLOS propagation. The constrained condition is applied based on the results of the LOS algorithms.

The main drawbacks of existing NLOS identification and mitigation techniques are outlined by Marano et al. [43]: i) instead of channel pulse responses, only the ranges are utilized, and thus a significant amount of information is wasted; ii) the joint probability distributions required by many statistics-based approaches are difficult to be

determined; and iii) while waiting for the collection of range estimates to establish a statistical history, latency will incur. An NLOS localization technique is feasible when additional information is provided, such as the RSSI signature map, the environment map, and the fact that all reflections are specular. The final localization accuracy depends on map resolution.

1.3 Proposed De-embedding Transfer Function Method for Non-Line-of-Sight Scenarios

To date, almost all the localization methods in the research literature have treated the NLOS effects as statistical; they only work well with a large sample size and a small number of outliers (NLOS measurements). However, if the NLOS environment (propagation channel characteristic) is known, a transfer function (channel pulse response) for the signal propagation can be acquired and utilized. This dissertation proposes and examines a novel localization method based on TDOA that incorporates information about the NLOS transfer function in an iterative process.

The physical explanation for the usual TDOA localization method is that each sensor pair predicts a hyperbola on which the transmitting emitter or source (target) lies, and this hyperbola is the set of points at a constant range-difference from the two foci (the pair of sensors); the estimated emitter location is then at the intersection of all of the hyperbolas (Fig. 1.2). From a mathematical point of view, three sensors are usually enough for 2D localization (i.e., locating a source with an unknown location that lies in a plane) in the absence of noise.

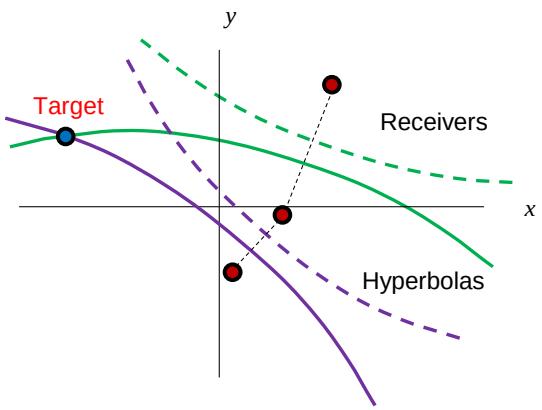

Figure 1.2. A physical explanation of the TDOA method for 2D localization.

It should be noted that this TDOA localization method is based on the assumption of free-space propagation, and the presence of an obstacle will add bias to the system due to refraction effects, reflections and transmission or scattering effects, unless it is accounted for. Here an iterative method based on TDOA localization is proposed, to acco0unt for these effects. Instead of using the signals directly received by the sensors (receivers) in the TDOA localization process, a “processed” set of signals is used, in which the transfer function of the system that accounts for the NLOS effects is de-embedded. Therefore, the received signals are modified to emulate what the receivers would have received had there been no obstacles present. That is, the effects of signal distortion due to reflections and scattering from the obstacles are removed, and the channel is calibrated back to free-space propagation. The proposed algorithm can be further extended to TOA, AOA, and hybrid mobile localization, since it directly rearranges the received signals and removes the NLOS effects.

The main interest in the present research is in localizing an arbitrary radiating source (target) inside an enclosed building. The basic parameters of the building were predetermined, such as the building size, wall permittivity, wall conductivity, and wall

thickness. Because the additional information of the propagation scenarios has to be identified ahead of time, this algorithm can be categorized into a NLOS localization technique. To simplify the geometry, several simplified models were assumed in order to examine the efficacy of the proposed method. These include an infinite front-wall model, an infinite parallel-wall model, a near-field model, and a 3D PEC ground plane model. In all of these cases it is possible to incorporate an analytical solution for the transfer function. A more complicated 2D enclosed-wall model and a 3D scattering-object model were then simulated using XFDTD, a commercial software based on the finite-difference time-domain (FDTD) method, to obtain the transfer function numerically. An experiment at Sandia National Laboratories was also conducted to verify the feasibility of our proposed method.

Although the mathematical models proposed here tend to focus on indoor localization, the proposed iterative method has great potential for wider use; as long as the propagation route is known and the computation complexity is manageable by the computational resources used, the transfer function for any propagation system can be obtained using numerical methods such as the finite-difference time-domain (FDTD), method, the finite element method (FEM), the method of moments (MoM), or other techniques such as high-frequency ray methods. The localization accuracy can then be significantly improved by de-embedding the transfer function in the TDOA method, using the proposed method.

1.4 Dissertation Outline

The goal of this research is to detect the location of an electronic device (the source or “target”) intentionally or unintentionally radiating a signal by using the

proposed method involving the de-embedding of the transfer function. The target is typically located within an enclosed area, nearby scattering objects or behind obstacles.

Chapter 2 first describes and analyzes the traditional LOS TDOA method, and studies this scheme in free space with either noise free or noisy conditions. This chapter provides an overview of the TDOA algorithm, and presents in detail a flow chart of how the algorithm is employed and implemented here, including signal modulation, TDOA determination and down conversion and filtering. Localization results are compared and evaluated, using both modulated and demodulated signal forms at the receiving sensors. Influence from different parameters contained in the system, as well as the effect known as the geometric dilution of precision (GDOP) are discussed. Several denoising methods are proposed, such as a moving average filter, coherent accumulation and averaging of the estimated location vectors; these are used when the TDOA localization system is contaminated by different levels of Gaussian white noise.

Chapter 3 proposes the novel algorithm for TDOA localization under generalized NLOS effects. This chapter provides an overview of the proposed method that involves de-embedding the transfer function; it then presents a global search method and an iterative method based on this concept. To validate the feasibility of the proposed theory, we introduce different canonical NLOS scenarios, including the near field, scattering and diffraction problems. Simplified corresponding models are obtained and investigated: the near-field model, the single-wall model, and the scattering-object model. We examine and discuss the effects of uncertainty in the physical parameters for the single-wall model, and modify the transfer function to improve the results when using a vertical dipole model for the source.

Chapter 4 investigates localization under multiple reflections. Three models are proposed: the parallel-wall model, a 3D localization model and a 2D enclosed-wall model. We thoroughly explore the convergence problem that arises in using the iterative method when multiple reflections are present, when the carrier frequency is high enough so that the size of the enclosure becomes significant. This problem is magnified when the bandwidth of the radiated signal is low. We present an effective solution to this problem by incorporating time gating and a hybrid iterative method. The transfer functions are obtained from either analytic solutions using a transverse equivalent network together with image theory and reciprocity, or from numerical solutions using commercial software, in particular XFDTD.

Chapter 5 presents an experiment designed and conducted at Sandia National Laboratories to validate the feasibility of the proposed approach. Results from a simulation are also presented to go along with the results from the experiment, to help strengthen the conclusions. We discuss how the results from both the experiment and the simulation show significant improvement in the stability of the localization, and then provide an explanation for this.

Chapter 6 discusses the results presented in this dissertation. A brief description of possible future work is also included.

Chapter 2

TDOA Localization

This chapter focuses on the analysis of the traditional time-difference-of-arrival (TDOA) localization system under both free space and noisy conditions. The entire system presented here is the basis for the proposed de-embedding transfer function approach that is introduced in Chapter 3.

In this chapter, the problem is assumed to be two-dimensional (planar), and the effects of the building/scattering object/obstacles are ignored (LOS). Also, the effects of the ground are ignored (i.e., the ground is assumed to be a perfect conductor, so that image theory reduces the problem to that of free-space propagation between the target and the receivers). Section 2.2 provides the implementation system of the TDOA, and Section 2.3 illustrates several denoising methodologies for Gaussian white noise. The last section discusses the corresponding simulation results in Matlab, including the sanity check, the influence of the system parameters, and the denoising methods.

2.1 Overview of Algorithms

Figure 2.1 shows the process of directly using the modulated (received) signal or demodulated signal to obtain the TDOA and hence get the target position. The baseband (modulating) signal is a Gaussian pulse for the result here, and the carrier signal is a sinusoidal wave with an initial phase shift (Section 2.2). The modulated signal transmits through an LOS propagation system and then arrives at different receivers. After passing through the Analog-to-Digital Converter (ADC), a cross-correlation is employed to get the TDOA between each pair of different receivers from either using the modulated

signal (received signal) or the demodulated signal (baseband signal). Then the Levenberg–Marquardt algorithm is used to determine the source position by minimizing the objective function associated with the unknown source position. The localization method using the demodulated signal for the cross-correlation process is called the demodulation method, while the one using the modulated signal is called the modulation method.

To obtain the demodulated signal, an extra low pass filter (shown in Figure 2.1 in the dotted box) is added to get rid of the carrier signal, leaving only the baseband part of the signal. The advantages of using a demodulated signal is that the sampling frequency can be reduced, and the accuracy in the near field might also be increased; the main disadvantage is that computation time will also be increased. When the baseband frequency is comparable to the carrier frequency, the demodulation process is not necessary.

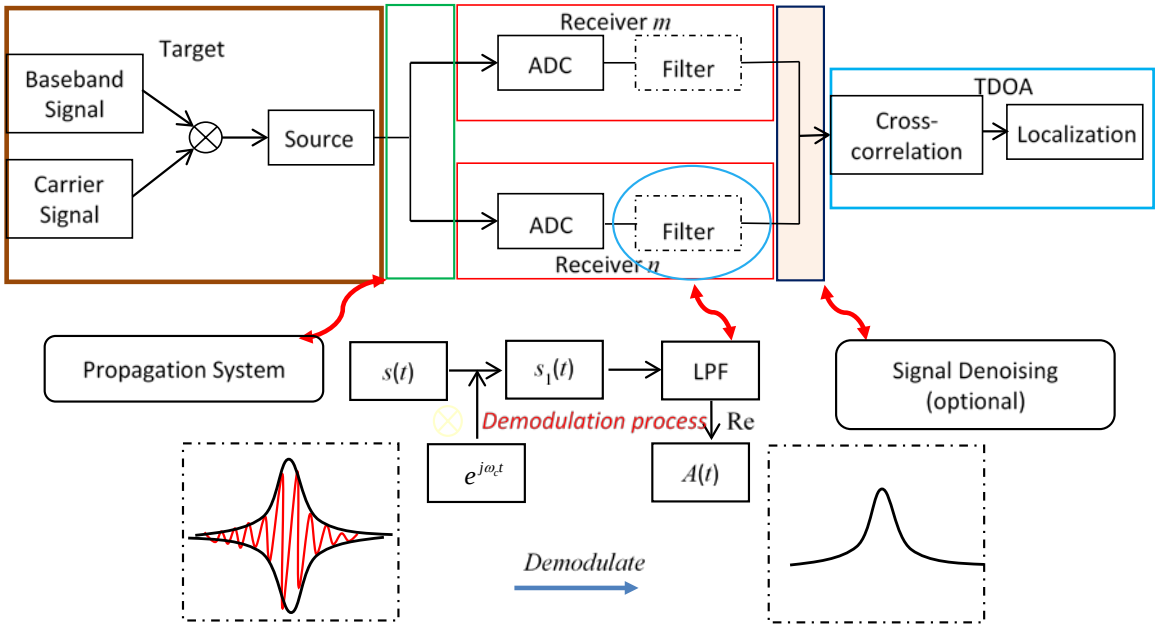

Figure 2.1. Algorithm for source localization using the received (modulated) signal.

A more detailed discussion of the implementation details in the TDOA method is given in the next section.

2.2 Implementation of Algorithms

2.2.1 Modeling of the Signal

A) Transmitting signal

The transmitting signal $m(t)$ used here is a sinusoidal carrier wave modulated by a Gaussian modulating amplitude (envelope) function $A_m(t)$, which is expressed as

$$m(t) = A_m(t)\cos(\omega_c t + \phi_m), \tag{2.1}$$

where

$$A_m(t) = e^{-\left(\frac{t}{t_{base}}\right)^2}.$$

In this notation ω_c and ϕ_m are the carrier frequency and phase, respectively. The "baseband frequency" (in Hertz) is defined from

$$f_{base} = \frac{1}{t_{base}}.$$

The complex form of the signal is

$$m_a(t) = A_m(t)e^{j(\omega_c t + \phi_m)} \ . \tag{2.2}$$

A typical result showing the transmitting signal and its specturm is shown in Fig. 2.2. It can be seen that the spectrum is highy localized to the frequency of the carrier wave, since the frequency of the carrier is much higher than that of the baseband signal (Gaussian envelope).

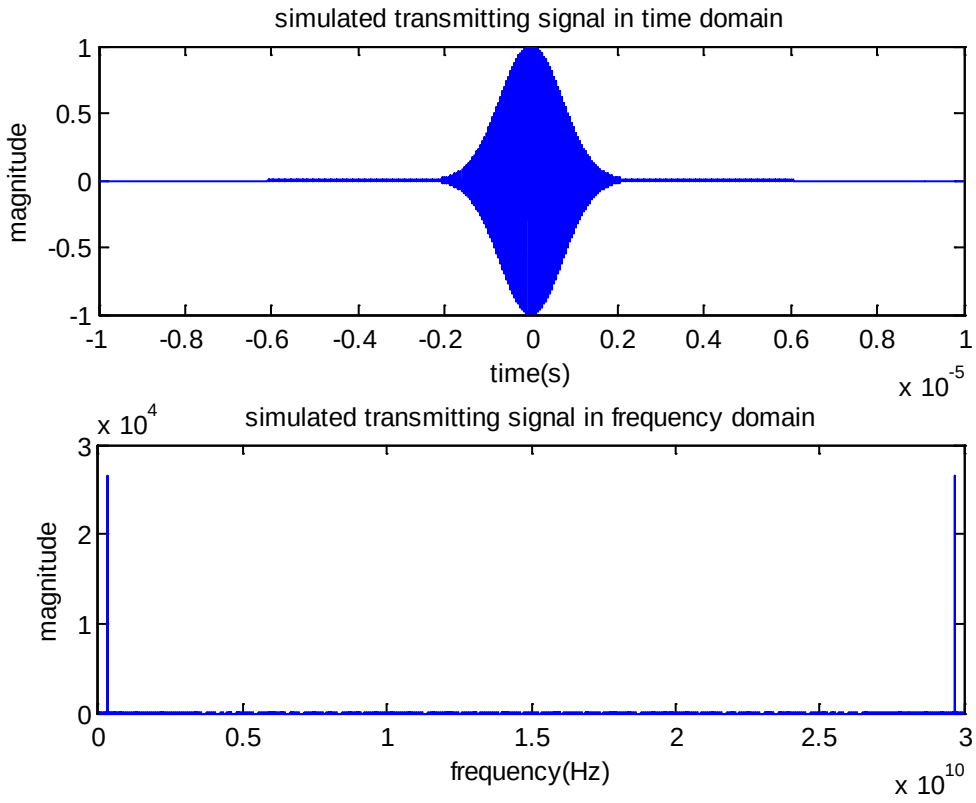

Figure 2.2. Time and frequency domain plots for the transmitting signal.

B) Transfer Function

For a *z*-directed infinitesimal dipole in free space, the fields are given as

$$E_r = \frac{Il}{2\pi}\eta e^{-jkr}\left(\frac{1}{r^2}\right)\left[1+\frac{1}{jkr}\right]\cos\theta$$
$$E_\theta = \frac{Il}{4\pi}(j\omega\mu)e^{-jkr}\left(\frac{1}{r}\right)\left[1+\frac{1}{jkr}+\frac{1}{(jkr)^2}\right]\sin\theta \qquad (2.3)$$
$$H_\phi = \frac{Il}{4\pi}(jk)e^{-jkr}\left(\frac{1}{r}\right)\left[1+\frac{1}{jkr}\right]\sin\theta.$$

In the *x*-*y* plane, i.e., $\theta = 90^\circ$, there only exists an E_θ and hence E_z component (E_z = -E_θ) for the electric field, and an H_ϕ component of the magnetic field, given as

$$E_z = Il\left(-\frac{j\omega\mu_0}{4\pi}\right)\left(\frac{1}{r}-\frac{j}{kr^2}-\frac{1}{k^2r^3}\right)e^{-jkr},$$
$$H_\phi = \frac{Il}{4\pi}(jk)\left(\frac{1}{r}\right)\left[1+\frac{1}{jkr}\right]e^{-jkr}. \quad (2.4)$$

The electric field corelates with the signal that would be received by an electric field sensor, such as a short dipole antenna, while the magnetic field indicates the information that would be received by a magnetic field sensor, such as a small loop antenna. Normalizing by the dipole moment $m(t) = I(t)l$, where l is the length of the (small) transmitting dipole and $I(t)$ is the current in the dipole, we define the transfer function $T(\omega, r)$ in the frequency domain for the electric field as

$$T(\omega, r) = -\frac{j\omega\mu_0}{4\pi r}\left[1-\frac{j}{kr}-\frac{1}{(kr)^2}\right]e^{-jkr}, \quad (2.5)$$

and the transfer function for the magnetic field as

$$T(\omega, r) = \frac{jk}{4\pi r}\left[1-\frac{j}{kr}\right]e^{-jkr}. \quad (2.6)$$

Henceforth, we focus on the vertical electric field.

If the PEC ground is taken into consideration, the transfer function for E_z becomes (with the factor of 2 added from image theory)

$$T(\omega, r) = -\frac{j\omega\mu_0}{2\pi r}\left[1-\frac{j}{kr}-\frac{1}{(kr)^2}\right]e^{-jkr}. \quad (2.7)$$

C) Received Signal

The Fourier and inverse Fourier transform relation between $m(t)$ and its transform $\tilde{m}(\omega)$ is given by

$$\tilde{m}(\omega) = \int_{-\infty}^{\infty} m(t)e^{-j\omega t}dt, \quad (2.8)$$

$$
\begin{aligned}
m(t) &= \frac{1}{2\pi}\int_{-\infty}^{\infty} \tilde{m}(\omega)\, e^{+j\omega t} d\omega \\
&= \frac{1}{\pi}\,\mathrm{Re}\int_{0}^{\infty} \tilde{m}(\omega)\, e^{+j\omega t} d\omega \\
&= \int_{0}^{\infty} \mathrm{Re}\left(\frac{1}{\pi}\tilde{m}(\omega)\, e^{+j\omega t} d\omega\right).
\end{aligned}
\tag{2.9}
$$

The phasor dipole moment Il is thus

$$
Il = \frac{1}{\pi}\tilde{m}(\omega) d\omega . \tag{2.10}
$$

The *z*-directed time-varying electric field signal at the receiver can then be expressed as

$$
s(t) = E_z(r,t) = \frac{1}{\pi}\,\mathrm{Re}\int_{0}^{\infty} \tilde{m}(\omega) T(\omega, r)\, e^{+j\omega t} d\omega . \tag{2.11}
$$

With noise added, the signal received at the *n*th receiver can be calculated with the transfer function as

$$
z_n(t) = s_n(t) + n_n(t) = F^{-1}\left\{F\left[m(t)\right] T\left(\omega, r_n\right)\right\} + n_n(t). \tag{2.12}
$$

Here $z_n(t)$ denotes the received signal E_z at the *n*th receiver, $m(t)$ denotes the transmitting signal dipole moment amplitude, and $n_n(t)$ denotes the additive Gaussian white noise in the *n*th receiver with a zero mean value and a Root Mean Square (RMS) standard deviation of σ_n. The signal and noise are mutually uncorrelated. Here *F* and F^{-1} denote the Fourier Transform and Inverse Fourier Transform. From the frequency domain expression, we can obtain the time domain expression for $s_n(t)$ in closed form if we wish, as

$$
s_n(t) = \left(-\frac{\mu_0}{2\pi r_n}\right)\left[s_{n1}(t) + s_{n2}(t) + s_{n3}(t)\right], \tag{2.13}
$$

where

$$
\begin{aligned}
s_{n1}(t) &= \frac{d}{dt} m(t-\tau_n) \\
s_{n2}(t) &= \frac{1}{\tau_n} m(t-\tau_n) \\
s_{n3}(t) &= \frac{1}{\tau_n^2} \int_{-\infty}^{t} m(t-\tau_n) dt,
\end{aligned}
\tag{2.14}
$$

where

$$
\tau_n = r_n / c, \tag{2.15}
$$

with r_n being the distance between the transmitter and the nth receiver. In the results, the Fourier transform method was used to calculate the received signal, since it is more general and extends to non-free-space propagation.

In the far field (where we keep only the $1/r$ term in the transfer function), the time-domain expression for the received signal is

$$
s_n(t) = 2\left(\frac{\tau_n - t}{t^2_{base}}\right) e^{-\left(\frac{t-\tau_n}{t_{base}}\right)^2} \cos(\omega_c(t-\tau_n)+\phi_m) - \omega_c e^{-\left(\frac{t-\tau_n}{t_{base}}\right)^2} \sin(\omega_c(t-\tau_n)+\phi_m). \tag{2.16}
$$

The complex form of this is

$$
\begin{aligned}
s_{na}(t) &= 2\left(\frac{\tau_n - t}{t^2_{base}}\right) e^{-\left(\frac{t-\tau_n}{t_{base}}\right)^2} e^{j(\omega_c t - \omega_c \tau_n + \phi_m)} \\
&\quad + j\omega_c e^{-\left(\frac{t-\tau_n}{t_{base}}\right)^2} e^{j(\omega_c t - \omega_c \tau_n + \phi_m)} \\
&= [A'_m(t) + j\omega_c A_m(t)] e^{j(\omega_c t - \omega_c \tau_n + \phi_m)}.
\end{aligned}
\tag{2.17}
$$

2.2.2 TDOA Determination

The true time difference of arrival (TDOA) between a pair of receivers i and j is given by

$$
\Delta t_{ij} \equiv t_i - t_j = \frac{1}{c}\left(\left|\underline{r_i} - \underline{r_t}\right| - \left|\underline{r_j} - \underline{r_t}\right|\right),\ i \neq j. \tag{2.18}
$$

By making a cross-correlation of the signals received by any pair of receivers, the estimated time delay between the two receivers can be determined. The cross-correlation function between two received signals $z_i(t)$ and $z_j(t)$ is given by

$$R_{z(i,j)}(\tau) = \left\langle z_i\left(t\right), z_j\left(t+\tau\right)\right\rangle = \frac{1}{T}\int_{\tau_A - T/2}^{\tau_A + T/2} z_i(t) z_j(t+\tau)\, dt, \tag{2.19}$$

where T is the time duration of the observation window and τ_A is the central time in the observation window. Since the transmitter's location is unknown, the transmitter's initial location is set at the center of the enclosed area for determining τ_A. If the shape of the signal is the same at the two receivers, then the TDOA is given by the value of τ that maximizes the cross-correlation. This is seen by using

$$\begin{aligned} z_i(t) &= s_i(t) + n_i(t) \\ z_j(t) &= s_j(t) + n_j(t) = s_i(t - \Delta t) + n_j(t). \end{aligned} \tag{2.20}$$

Because white noise is orthogonal to the signal and other noise, we have

$$R_{z(i,j)}(\tau) = \frac{1}{T}\int_{\tau_A - T/2}^{\tau_A + T/2} s_i(t) s_i(t+\tau-\Delta t)\, dt = R_{s(i,i)}(\tau - \Delta t). \tag{2.21}$$

According to property of the correlation function, $R_{s(i,j)}(0)$ reaches a maximum when $\tau = \Delta t = -TDOA_{ij}$.

Maximizing the cross-correlation will give the TDOA and hence the correct source location if there is no distortion of the signal during the propagation, or if the distortion is the same at both receivers. This will not be the case in the near field, since the signal shape predicted by Eq. (2.14) will depend of the value of τ and hence the distance from the source. In the far field, the received signal will be the derivative of the transmitted signal, as seen by the first term in Eq. (2.14). In this case the signal will be

the same at all receivers except for a time delay, and the TDOA method should give perfect localization, in the absence of noise and numerical errors.

When performing the cross-correlation, a time step Δt is typically used. This can be the same as the time step in the ADC sampling, or different. The accuracy of the source localization (in meters) will then be limited to around $c\Delta t$. For example, a 1 GHz sampling frequency in the cross-correlation corresponds to $\Delta t = 10^{-9}$ seconds, and this will correspond to a location error of around 0.3 meters.

It is possible to increase the localization accuracy by using spline interpolation to fit the sampled data points, so that a finer sampling can then be used in the cross-correlation than is used in the ADC. This is explored in Chapter 3.

2.2.3 Localization using TDOA

In principle, only three receivers (two pairs of receivers) are needed to determine the source (target) location. In this case, there are two TDOA equations (coming from the two pairs of receivers) and two unknowns (the x and y coordinates of the target). Geometrically, each TDOA equation localizes the target to lie on one branch of a hyperbola, since a hyperbola is a curve that corresponds to having the difference in distances from the curve to two fixed points (the two receivers) fixed. (Only one branch of the hyperbola is needed, since it is also known whether the TDOA is positive or negative. In the absence of noise, only two pairs of receivers would be sufficient, and all other pairs would give redundant information. In the presence of noise, the localization is usually done by minimizing the localization function $F(x,y)$, defined as

$$F(x,y)=\sum_{i=1}^{N}\sum_{j\neq i}\left[c\cdot TDOA_{ij}-\begin{pmatrix}\sqrt{(x_i-x)^2+(y_i-y)^2}\\-\sqrt{(x_j-x)^2+(y_j-y)^2}\end{pmatrix}\right]^2. \quad (2.22)$$

Note that this function accounts for all possible pairs of receivers, and thus takes advantage of all of the available information. The Levenberg–Marquardt algorithm can be used to solve this nonlinear minimization problem.

In the TDOA algorithm using the demodulated signal, it is helpful to know the carrier frequency, and possibly the phase of the carrier signal. Possible approaches are outlined in Section 2.2.4.

2.2.4 Down Conversion and Filtering

A) Carrier frequency determination

Under noise-free conditions, the frequency that maximizes the magnitude of the Fourier transform of the signal is the carrier frequency. Under noisy conditions, algorithms such as the MUSIC algorithm can be used to obtain the carrier frequency.

B) Phase determination

There are at least two methods to get the phase of the carrier signal. The first is using orthogonal demodulation and the second is based on using special points in the frequency domain. These methods are outlined in flowchart form in Fig. 2.3. From numerical experiments it was found that there is no need to figure out the phase of the carrier signal, as this information does not help in the TDOA localization process.

B1) Orthogonal demodulation method

A flowchart of the orthogonal demodulation scheme is shown in Fig. 2.3.

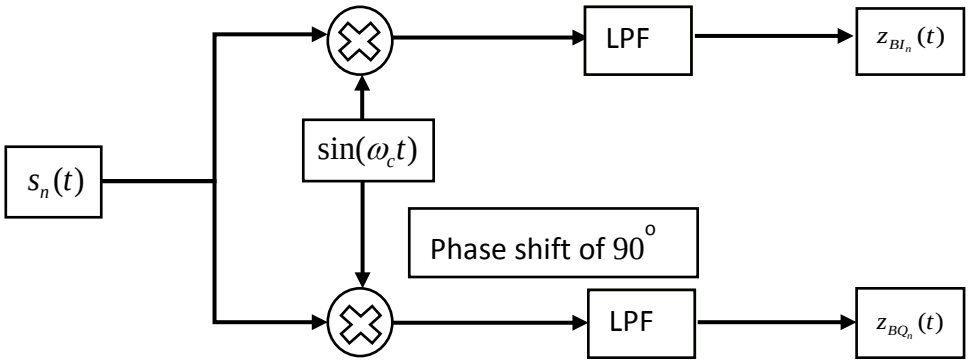

Figure 2.3. Orthogonal demodulation process.

The received signal is denoted as

$$s_n(t) = A(t)\cos(\omega_c t + \phi), \tag{2.23}$$

and after passing through the process in Fig. 2.3, we obtain

$$\begin{aligned} z_{BI_n}(t) &= \frac{1}{2}A(t)\cos(\phi) \\ z_{BQ_n}(t) &= \frac{1}{2}A(t)\sin(\phi), \end{aligned} \tag{2.24}$$

so that

$$\phi = \tan^{-1}\left(\frac{z_{BQ_n}(t)}{z_{BI_n}(t)}\right). \tag{2.25}$$

However, since the low pass filter will not ideally filter out all of the high frequencies, the phase is not always accurate.

B2) Carrier sampling method

The received signal can be expressed as

$$s(t) = \frac{1}{2}A(t)e^{j(\omega_c t+\phi)} + \frac{1}{2}A(t)e^{-j(\omega_c t+\phi)}, \tag{2.26}$$

and in the frequency domain, the transform is

$$\tilde{s}(\omega) = \frac{1}{2} e^{j\phi} \tilde{A}(\omega - \omega_c) + \frac{1}{2} e^{-j\phi} \tilde{A}(\omega + \omega_c), \tag{2.27}$$

hence,

$$\frac{\tilde{s}(\omega_c)}{\tilde{s}(-\omega_c)} = e^{j2\phi_m}, \tag{2.28}$$

so that

$$\phi = \frac{\cos^{-1}\left(\mathrm{Re}\left(\frac{\tilde{s}(\omega_c)}{\tilde{s}(-\omega_c)} \right) \right)}{2}. \tag{2.29}$$

C) Demodulation

The down conversion and filter process is used in the demodulation method. A low-pass filter is used to filter the carrier signal out, and the baseband signal is used in the cross-correlation to get the TDOA. Adding this down conversion and filtering process will increase the computation time, though with a low sampling rate it will increase the accuracy, as results will show later. There are two methods that have been implemented, one in the frequency domain and the other in the time domain.

C1) Demodulation using time-domain filter

Figure 2.4 shows the process using the time-domain filter. The received signal is represented as

$$\begin{aligned} s(t) &= A(t)\cos(\omega_c t + \phi) \\ &= \frac{1}{2} A(t) e^{j(\omega_c t + \phi)} + \frac{1}{2} A(t) e^{-j(\omega_c t + \phi)}. \end{aligned} \tag{2.30}$$

After multiplying the signal by $2e^{j\omega_c t + j\phi}$, the received signal becomes $s_1(t)$, i.e.,

$$s_1(t) = A(t) e^{j2(\omega_c t + \phi)} + A(t). \tag{2.31}$$

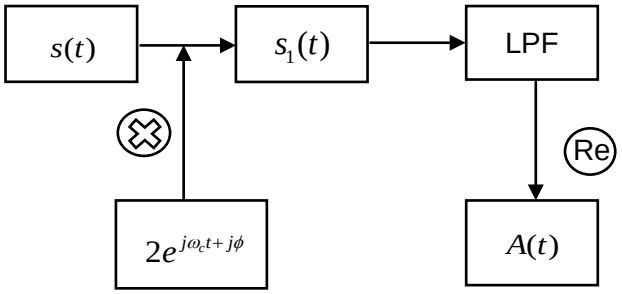

Figure 2.4. Time-domain filter process used to filter out the carrier signal.

Passing the signal through the low pass filter, the first term is filtered out, so that we are left with the term $A(t)$, the amplitude of the baseband signal. In theory, the result should be a real signal, but since the filter will not always behave ideally, the real part should be taken to recover a real-valued baseband signal.

It was found that it is sufficient to multiply the received signal by $e^{j\omega_c t}$. After filtering, the result will then be a complex baseband signal that contains a complex phase-shift term $e^{j\phi}$, but this does affect the accuracy of the TDOA when using the cross-correlation. Note that the time-domain filtering can be used when software (such as Matlab) is available that can perform filtering directly on a time-domain signal.

C2) Demodulation using frequency-domain filter

Figure 2.5 shows the process of using a frequency-domain filter to filter out the carrier frequency. The difference between the frequency-domain filter and the time-domain filter is that the input signal for the low-pass filter is transformed into the frequency domain, so the filtering is done in the frequency domain.

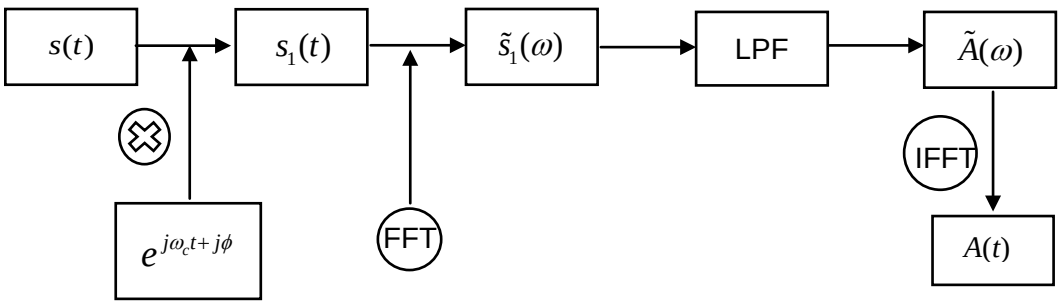

Figure 2.5. Frequency-domain filter process used to filter out the carrier signal

2.3 Denoising Methodology

Figure 2.6 presents a flow chart of the denoising process implemented for Gaussian white noise. As shown in the chart, $N \times M$ trials for each sensor are needed in order to achieve one particular result. In the coherent accumulation part, M trials produce one signal trial for TDOA localization. It has been shown that this process gives a much more accurate localization in the following numerical result part. However, the disadvantage is that many trials are needed to get one final localization result.

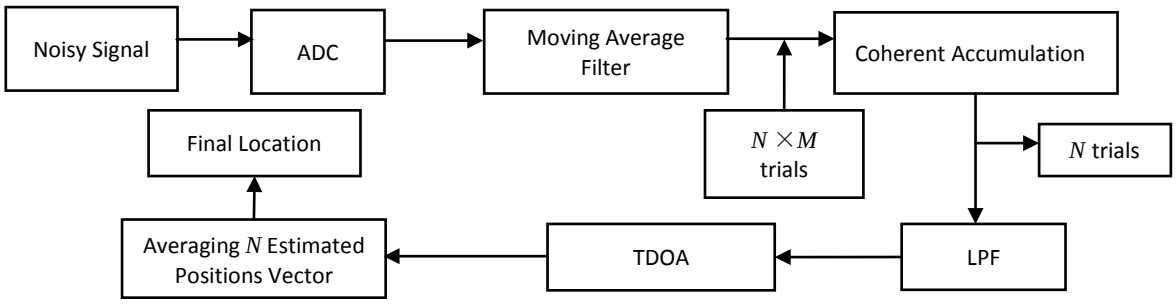

Figure 2.6. Flow chart of denoising process.

2.3.1 Moving Average Filter

The moving average filter operates by averaging a number of points from the input noisy signal (after the ADC, the signal is always a discrete sequence) to produce each point in the output signal, which is written as

$$z_n'[i] = \frac{1}{2m+1} \sum_{j=-m}^{m} z_n[i+j], \tag{2.32}$$

where z_n [i] denotes the received signal at the nth receiver, and z'_n [i] denotes the output of the moving average filter. Here, a five-point moving average filter is used (m = 2). The span is adjusted for data points that cannot accommodate the specified number of neighbors on either side. The end points are not smoothed because a span cannot be defined. Since the noise is additive and random at each point, the moving average filter can efficiently reduce the noise in the time domain.

2.3.2 Coherent Accumulation

Coherent accumulation is also used for improving the SNR. Since in the frequency domain the amplitude of the noise is much smaller compared with the signal, and also each trial has a different noise spectrum, accumulating the trials together in the frequency domain will thus increase the amplitude of the signal compared to the noise. The SNR thus can be improved by $\sqrt{N}$. In equation form,

$$z_n^{co}[i] = \frac{1}{M} F^{-1}\left(\sum_{j=0}^{M} F\left(z_{nj}'[i] \right) \right), \tag{2.33}$$

where z_{nj} [i] means the jth trial used for coherent accumulation at the nth receiver, F denotes Fourier Transform, and F^{-1} denotes the Inverse Fourier Transform. Every M trial produces one single result for TDOA localization.

If the trials have a different time shift, the signals produced from the accumulation process will have a phase shift in the frequency domain, lowering the improvement in the SNR and hence the localization accuracy. In Section 2.4.4, more details on the effect of a random time shift in the trials are given.

2.3.3 Averaging Estimated Location Vector

This process makes use of the statistical property of the localization. We use

$$[x_{est}, y_{est}] = \left[\frac{1}{N} \sum_{i=1}^{N} x_i, \frac{1}{N} \sum_{i=1}^{N} y_i \right], \tag{2.34}$$

where (x_i, y_i) is the estimated target location vector for each trial used in the TDOA process. Since the noise is random, for each trial the estimated location is different. However, the averaging process acts like shooting a target; the more holes that are on the target, the more chance there is that the holes will cover the target with equal probability. Thus averaging the hole positions will yield the true bull's eye position.

2.4 Numerical Results and Discussion

A) Definition of Localization Accuracy

The localization error is defined as

$$Error = \sqrt{\left(x_{est} - x_{true} \right)^2 + \left(y_{est} - y_{true} \right)^2}, \tag{2.35}$$

where (x_{true}, y_{true}) is the true target location, and (x_{est}, y_{est}) is the estimated location by minimizing the objective function in Eq. (2.22). This error is used to characterize the localization accuracy in the case of no noise.

When noise exists, the Monte Carlo method is applied to study the localization accuracy in order to provide more reliable statistical estimates of the error. The added

Gaussian white noise has a zero mean, and the power (which for Gaussian white noise is the same as the variance) is calculated by the specified signal-to-noise ratio (SNR) as

$$SNR = \frac{P_{signal}}{P_{noise}}. \tag{2.36}$$

The signal power for a real-valued signal consisting of N sampled time values is defined as

$$P_{signal} = \frac{1}{N}\sum_{n=1}^{N} x_n^2 . \tag{2.37}$$

Instead of showing individual random errors, an RMS error, which aggregates them into a single measure, is defined as

$$RMSE = \sqrt{\frac{1}{Q}\sum_{q=1}^{Q}(x_{est}^{(q)} - x_{true})^2 + (y_{est}^{(q)} - y_{true})^2}, \tag{2.38}$$

where Q is the number of simulations used in the Monte Carlo trials and $(x_{est}^{(q)}, y_{est}^{(q)})$ is the estimated location in the qth simulation. Figure 2.7 shows the basic assumptions used to obtain the results.

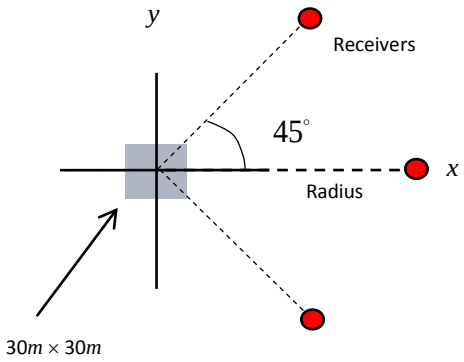

Figure 2.7. Top view showing the positions of the target and the receivers.

B) Simulation Assumptions

- The geometry consists of a square domain (simulating a square building footprint) that is 30 meters by 30 meters, centered at the origin.
- A single vertical dipole is used as the source.
- The dipole radiates a carrier wave that is modulated by a lower frequency baseband Gaussian signal. The carrier frequency is 300 MHz, and the base band frequency is 1 MHz. The carrier signal has a phase of 45˚.
- The receivers are located at a distance from the origin that varies from 1 meter to 1 km. If not stated otherwise, the baseline case is three sensors positioned on a circle with a radius of 100 meters, centered at the origin. The position angles with respect to the *x* coordinate are -45˚, 0, and 45˚, respectively.
- The TDOA for a pair of receivers is estimated using a cross-correlation between the signals obtained from each pair of receivers. The cross-correlation is done using either the original (modulated) signal or the demodulated signal. If not mentioned, the baseline corresponds to using the demodulated signal, the sampling frequency is 1 GHz, and the bit resolution is 14.
- Gaussian white noise is added to the signals to simulate a noisy environment. If not mentioned, the baseline condition is noise-free.
- The receivers are outside of the building, which means the distance to the center of the building is larger than 15 meters.

2.4.1 Sanity Check

As a "sanity check" we examine the localization accuracy when the target is located at different positions inside the domain of interest when there is no noise and the

sampling frequency in the ADC is very high. Table 2.1 shows the parameters used for the sanity check simulation. Figure 2.8 shows that the average localization error is quite small when the sampling frequency is 100 GHz, around a few millimeters. This error is expected based on the corresponding Δt, as predicted by the term $c\Delta t$, where $\Delta t = 10^{-11}$ seconds.

Table 2.1. Parameters used for the sanity check.

Target	A *z*-directed dipole moving in the *x*-*y* plane within an area of 30 meters × 30 meters with a step size of 0.5 meters in the *x*-direction and 0.5 meters in the *y*-direction.
ADC	Sampling frequency is 100 GHz (Fig. 2.8) or 1 GHz (Fig. 2.9),

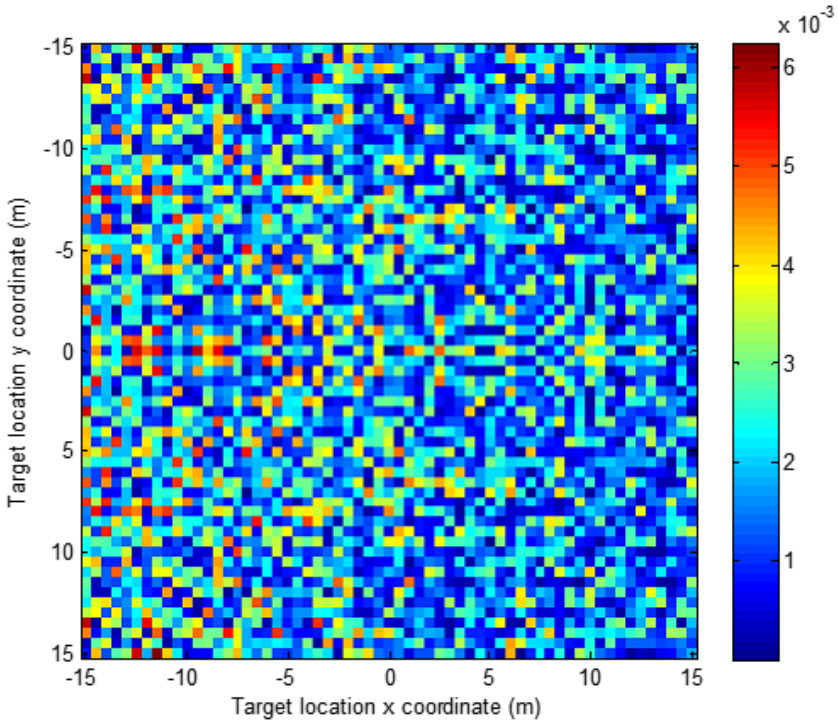

Figure 2.8. Sanity check when the sampling frequency is 100 GHz.

When the sampling frequency is reduced to 1 GHz, the sanity check result is as shown in Fig. 2.9. The average error in the localization has now increased to around 0.3 meters, as expected.

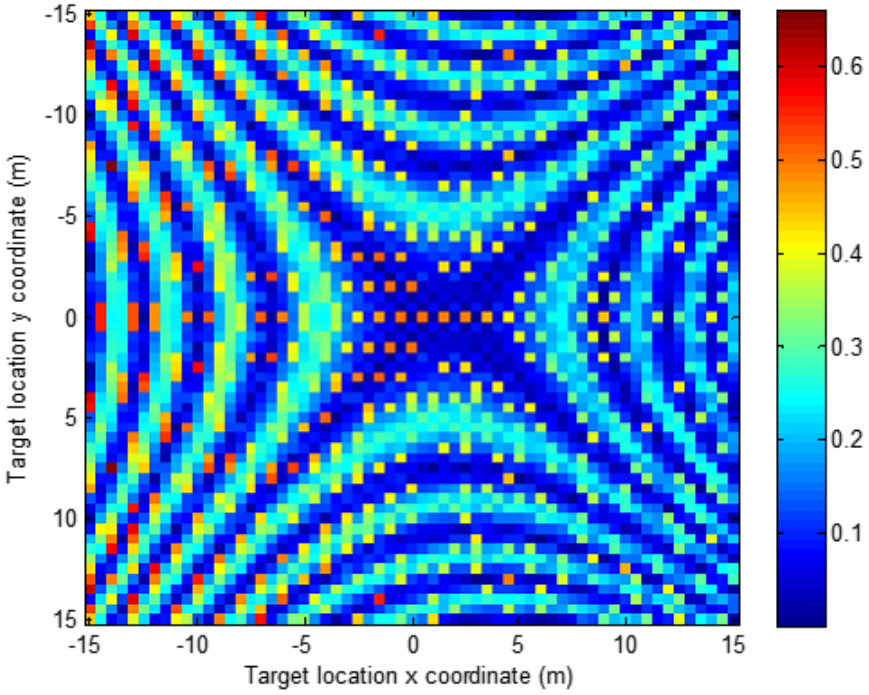

Figure 2.9. Sanity check when the sampling frequency is 1 GHz.

The next section presents our investigation into the effects of changing various parameters and methods on the localization accuracy, and the results.

2.4.2 Comparison between Modulation and Demodulation Signals

The modulated and demodulated methods are first compared for a sampling frequency of 1 GHz. Figure 2.10 shows that for most distances, the demodulated method is more accurate than the modulated one. Table 2.2 shows the involved parameters in this simulation.

Table 2.2. Parameters for the comparison of methods at 1 GHz.

Target	A *z*-directed dipole is placed inside the enclosed region. The target is at (-5, 0) meters.
Method	Using demodulated method or modulated method
ADC	Sampling frequency is 30 GHz (Fig. 2.11), or 1 GHz (Fig. 2.10).

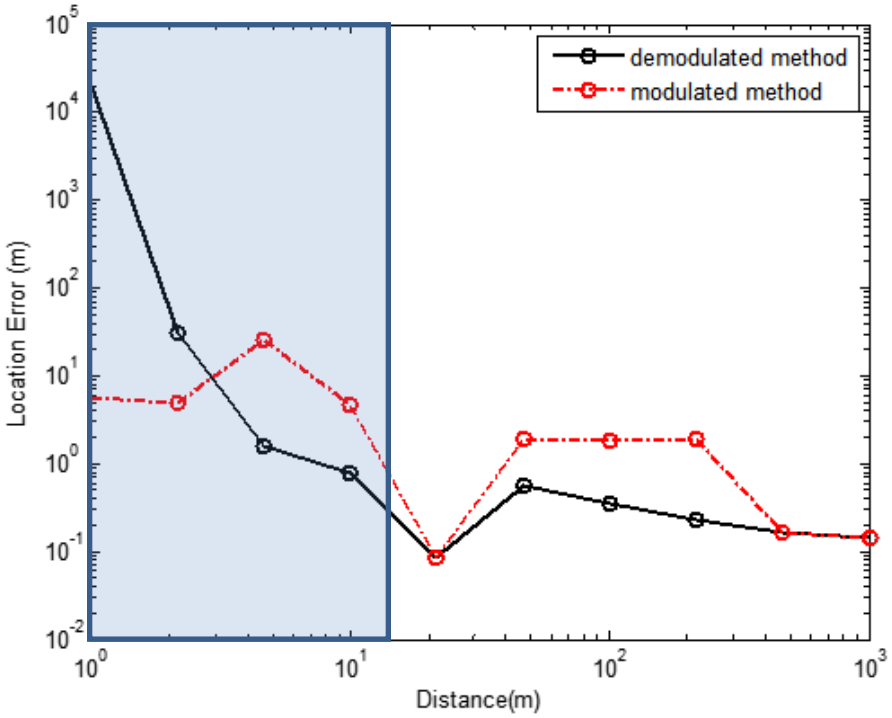

Figure 2.10. Comparison between different methods for a target at (-5, 0) meters, with a sampling frequency of 1 GHz.

The modulated and demodulated methods are then compared at a sampling frequency of 30 GHz. Figure 2.11 shows that with a very high sampling frequency, the demodulated and the modulated methods give the same accuracy.

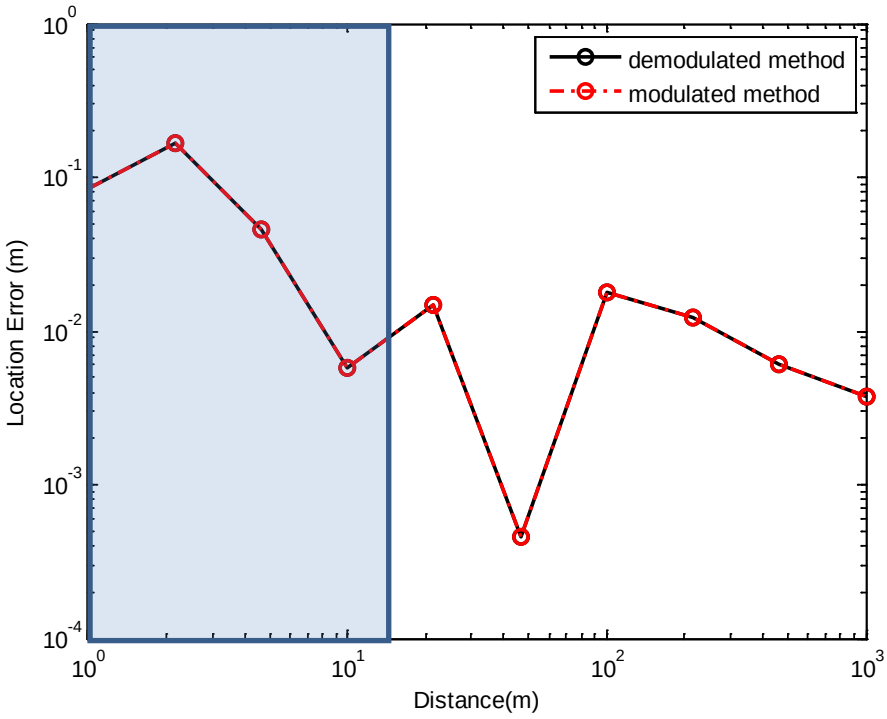

Figure 2.11. Comparison between different methods for a target at (-5, 0) meters, with a sampling frequency of 30 GHz.

2.4.3 Influence of System Parameters

A) Effects of sampling frequency

Although the plot has many oscillations, Fig. 2.12 shows the trend that the location error is inversely proportional to the sampling frequency. Table 2.3 shows the involved parameters in this sampling frequency study.

Table 2.3. Parameters for the sampling frequency study.

Target	A *z*-directed dipole is placed inside the enclosed region. The target is at (-5, 0) meters.
ADC	The sampling frequency is from 1 GHz to 100 GHz, and the bit resolution is 14 bits.

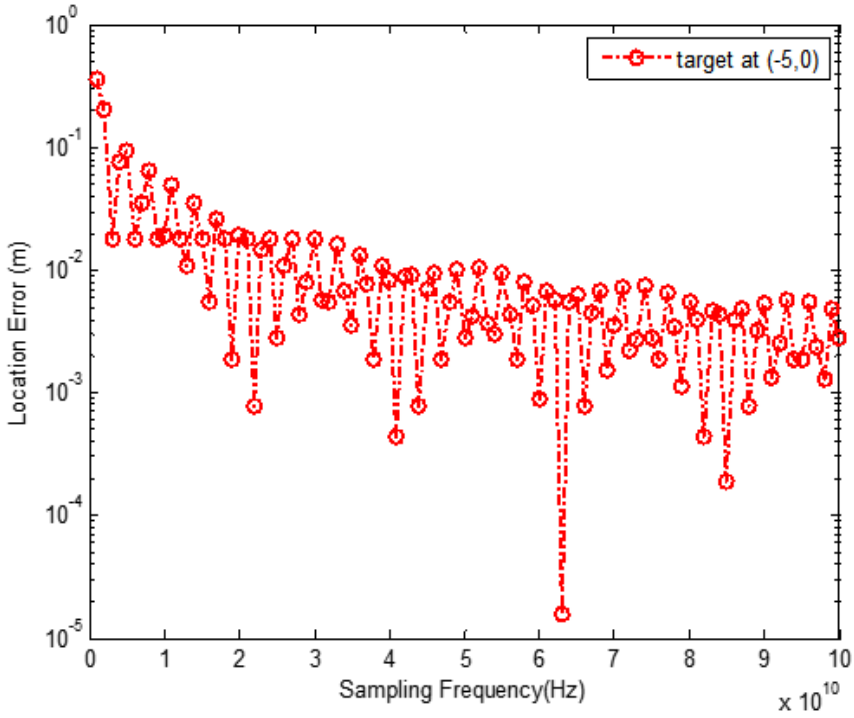

Figure 2.12. Effects of sampling frequency.

B) Effects of bit quantization

Figure 2.13 shows when the resolution is below six bits, the location error starts increasing. The error is always very small when the target is located at the origin, but this is evidently due to the symmetry of the problem, which is not typical for a general target. Table 2.4 shows the involved parameters in this bit quantization study.

Table 2.4. Parameters for the bit quantization study.

Target	A *z*-directed dipole is placed inside the enclosed region. Two positions are studied: (0, 0) meters and (-5, 0) meters, respectively.
ADC	The sampling frequency is 1 GHz, and the bit resolution is from 1 bit to 14 bits.

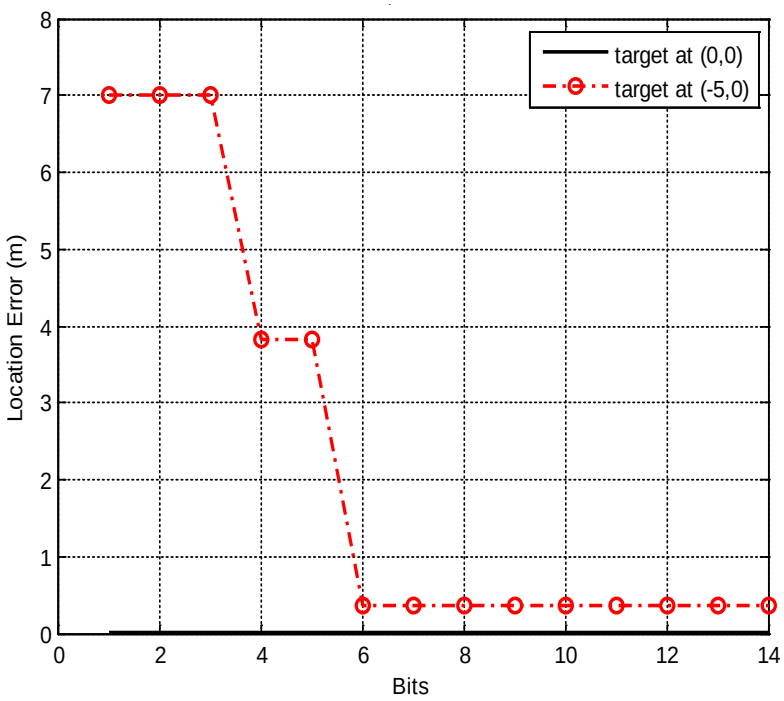

Figure 2.13. Effects of bit resolution.

C) Effects of noise

Here we present results showing the effects of the SNR on localization accuracy. Table 2.5 shows the involved parameters under noisy conditions.

Table 2.5. Parameters under noisy conditions.

Target	A *z*-directed dipole is placed inside the closed region. Target position is (-5, 4) meters.
Noise	The SNR is from -20 dB to 20 dB, added in front of the ADC in each receiver. Each receiver has the same SNR level.

The results are shown in Fig. 2.14; it can be seen that the SNR should be larger than about 20 dB so that the localization accuracy is not significantly affected by noise.

In Section 2.4.4, denoising methods are used to suppress the noise and improve signal-to-noise ratio; these include the moving average filter (here called the smoothing method), coherent accumulation, and the averaging of the location vector method.

The Monte Carlo method is used to obtain a prediction. 100 trials of the signal are applied for each SNR in the Monte Carlo method.

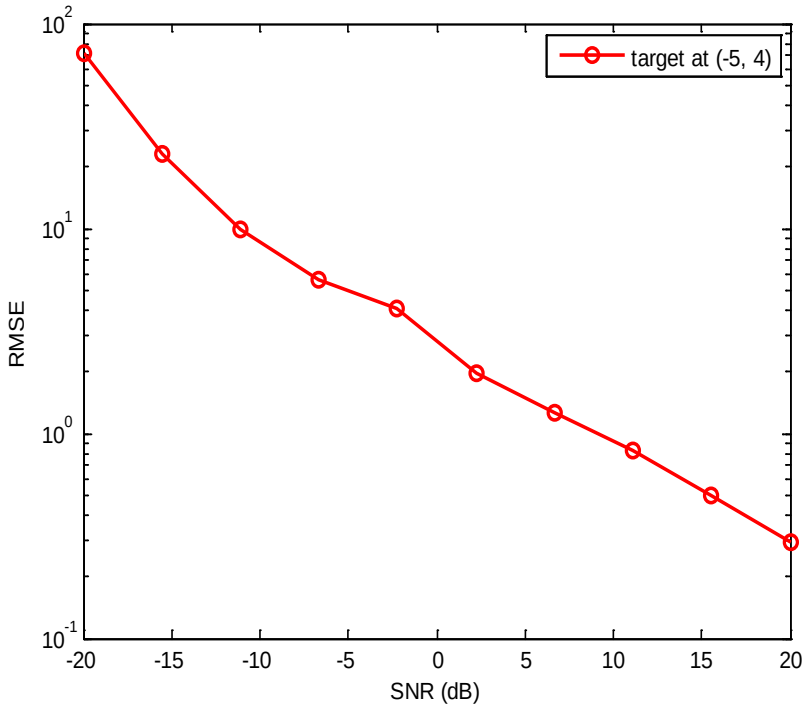

Figure 2.14. The RMS error (RMSE) under noisy conditions, versus the noise level (SNR), for a sampling frequency of 1 GHz.

D) Effects of sensor geometry

Table 2.6 shows the parameters used for the geometry of the receivers study. Figure 2.15 shows the top view of the different geometries for different cases. Results in Fig. 2.16 show the effect from the geometry of the receivers under noisy conditions.

Table 2.6. Parameters used for the geometry of the receivers study.

Target	A *z*-directed dipole is placed inside the closed region. Target position is (-5, 4) meters.
Receivers	Three sensors are positioned on a circle with a radius of 100 m, centered at the origin. The position angles with respect to the *x* coordinate are -120˚, 0, and 120˚, respectively for Case 1; -90˚, 0, and 90˚, respectively for Case 2; -45˚, 0, and 45˚, respectively for Case 3; -10˚, 0, and 10˚, respectively for Case 4.
SNR	SNR from -20 dB to 20 dB, added in front of the ADC in each receiver. (The sampling frequency is 1 GHz, without interpolation to save computation time.) Each receiver has the same SNR level. (To save computation time, only 10 trials are counted.)

It can be seen from these results that when the number of sensors is fixed, the smaller the viewing angle of the sensors is, as seen by the target, the larger the localization error becomes. The accuracy of the localization degrades quickly as the angular spread of the sensors becomes smaller, when noise is present. For example, in Case 4, the SNR has to be larger than 20 to get reasonable results. This is consistent with the well-known “Geometric Dilution of Precision” (GDOP) that occurs in localization problems, including, e.g., GPS [44].

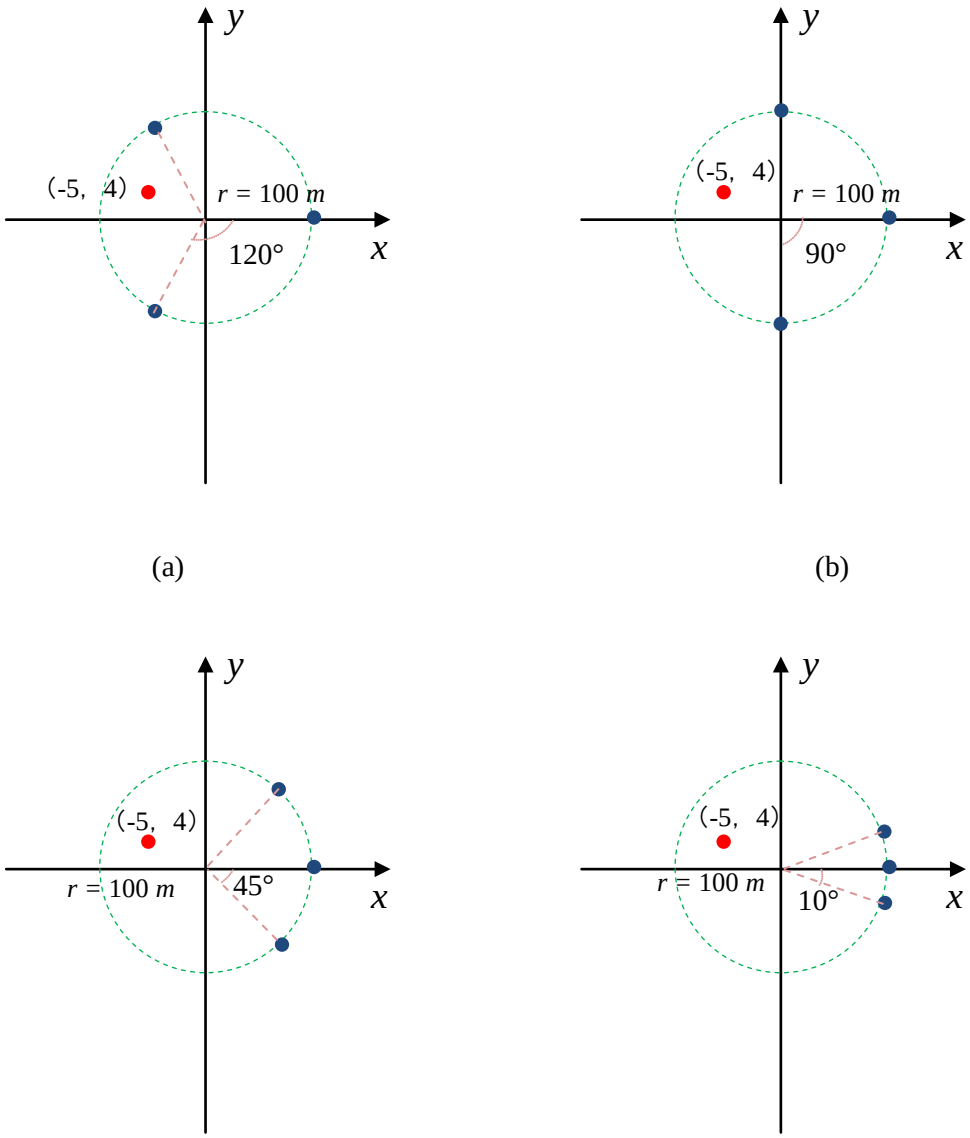

Figure 2.15. Top view showing the different geometries of the 3 receivers: (a) Case 1; (b) Case 2; (c) Case 3; (d) Case 4.

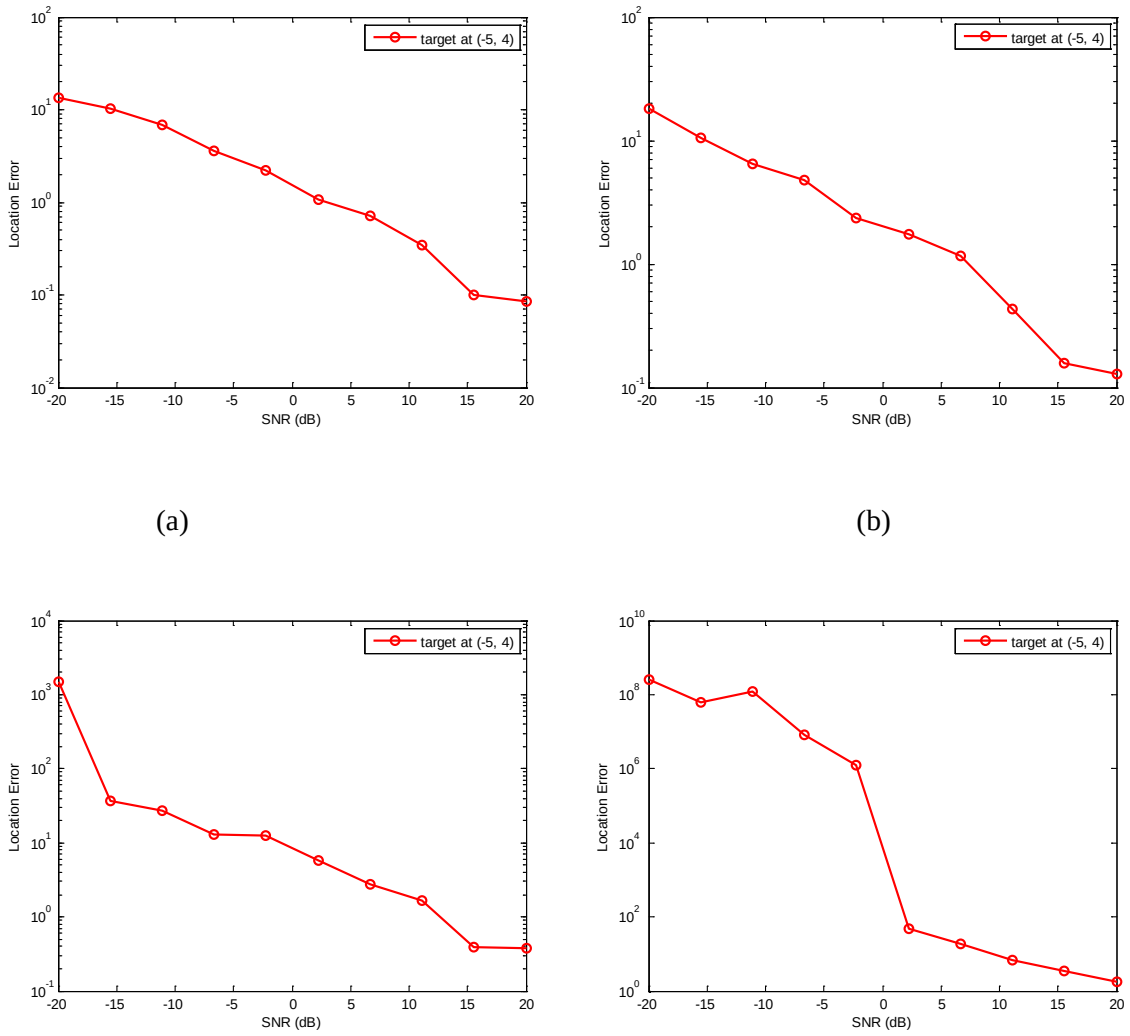

Figure 2.16. Effect of the number of receivers on location accuracy, when keeping the total angle at 360˚.

To explain the GDOP working principle, we define functions $f_i(x, y)$ as $f_i = \sqrt{(x_i - x)^2 + (y_i - y)^2} - ct_i,\ i = 1,2,3$ (three sensors are assumed), where t_i represents the time of arrival from a point at (x, y) to the ith sensor at (x_i, y_i).

The functions f_i (x, y) are assumed to have an error in the cross-correlation (due to the sampling frequency), and hence an error in t_i (called Δt, assumed to be the same for all sensors, for simplicity). The function f_i is then linearized by using a Taylor's series around the true target position (x_0, y_0) and by neglecting the higher-order terms. We can then write

$$f_i = a_{xi}\Delta x + a_{yi}\Delta y - c\Delta t, \;\; i = 1,2,3, \tag{2.39}$$

where

$$\begin{aligned} &a_{\xi i} = \frac{\xi_i - \xi_0}{r_i}, \; \xi = x, y, \qquad\qquad r_i = \sqrt{\left(x_i - x_0\right)^2 + \left(y_i - y_0\right)^2}, \;\; i = 1,2,3. \\ &\Delta\xi = \xi - \xi_0, \;\; \xi = x, y, \end{aligned} \tag{2.40}$$

and we can then write the above result in a complex matrix formulation as

$$\left(\Delta f\right) = \begin{pmatrix} \Delta f_1 \\ \Delta f_2 \\ \Delta f_3 \end{pmatrix} = \begin{pmatrix} a_{x1} & a_{y1} & 1 \\ a_{x2} & a_{y2} & 1 \\ a_{x3} & a_{y3} & 1 \end{pmatrix} \begin{pmatrix} \Delta x \\ \Delta y \\ -c\Delta t \end{pmatrix} = \left[H\right]\left(\Delta p\right), \tag{2.41}$$

where

$$\left[H\right] \equiv \begin{pmatrix} a_{x1} & a_{y1} & 1 \\ a_{x2} & a_{y2} & 1 \\ a_{x3} & a_{y3} & 1 \end{pmatrix}, \;\; \left(\Delta p\right) \equiv \begin{pmatrix} \Delta x \\ \Delta y \\ -c\Delta t \end{pmatrix}. \tag{2.42}$$

The condition number of H decides whether the sensor geometry is good for localization. The larger the condition number, the more digits of accuracy will be lost in the localization due to error in the Δf vector, which comes from the cross-correlation error.

As shown in Table 2.7, when the viewing angle of the sensors decreases, the condition number of the *H* matrix increases rapidly, which means more loss of accuracy in the localization.

Table 2.7. Condition number of the *H* matrix vs. sensor array aperture angle.

Aperture	360˚	180˚	90˚	36˚	18˚	12˚
Condition Number	1.47	2.26	10.85	75.94	309.49	698.82

2.4.4 Denoising Results

Figure 2.17 shows that the moving average filter improves the accuracy of TDOA localization, especially when the SNR is lower than -10 dB. In this section, all simulations are under noisy conditions, in which Gaussian white noise is added in front of the ADC in each receiver. Each receiver has the same SNR level.

A.1) Moving average filter (smoothing method)

Table 2.8 shows the information used for the denoising study using the moving average filter.

Table 2.8. Information used for the denoising study using the moving average filter.

Target	A *z*-directed dipole is placed inside the closed region. The target position is (-5, 4) meters.
Method	Demodulation method, using a moving average filter.

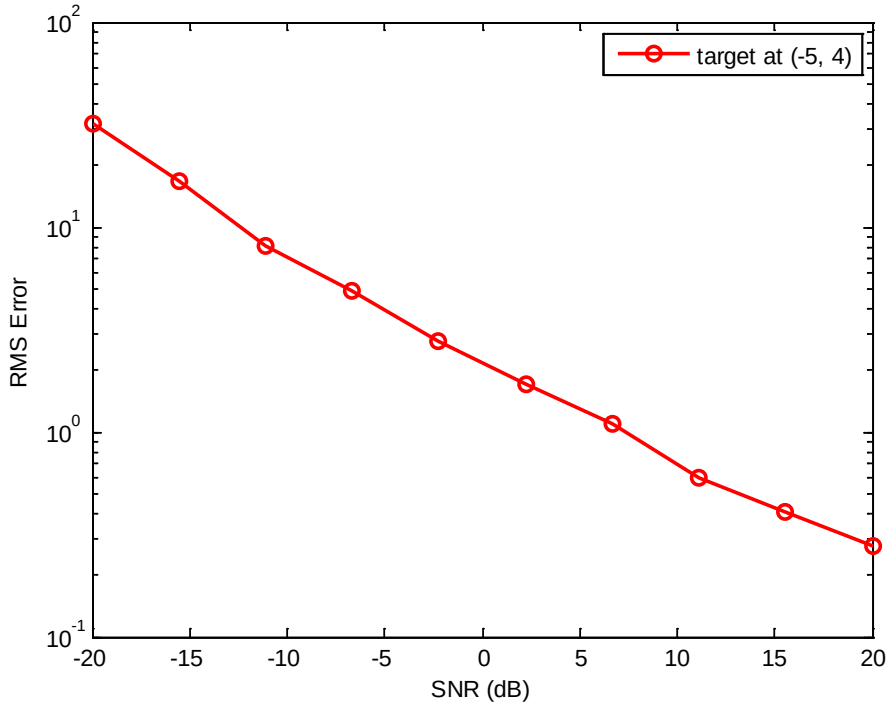

Figure 2.17. The RMS error (RMSE) under noisy conditions, versus the noise level (SNR), using a moving average filter.

A.2) Coherent accumulation

Table 2.9 shows the information used for the denoising study using coherent accumulation. Figure 2.18 shows a great improvement in the accuracy when using coherent accumulation.

Table 2.9. Information used for the denoising study using coherent accumulation.

Target	A *z*-directed dipole is placed inside the closed region. The target position is (-5, 4) meters.
Method	Demodulation method, using coherent accumulation (16 trials).

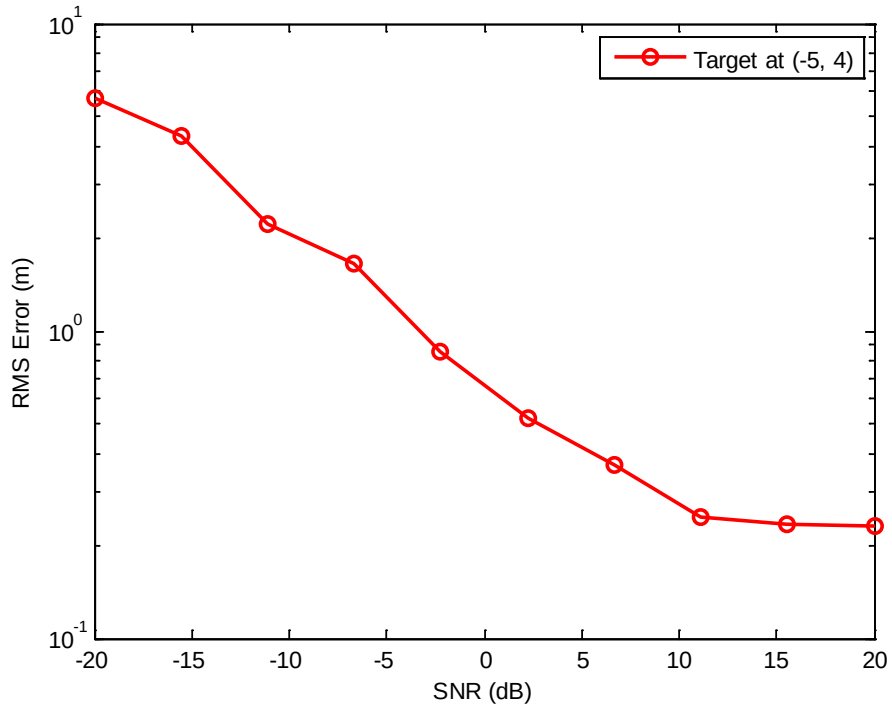

Figure 2.18. The RMS error (RMSE) under noisy conditions, versus the noise level (SNR), using coherent accumulation.

As can be seen in Fig. 2.18, when the SNR is -20 dB, the error is reduced to be below 10 m. When the SNR is greater than 10 dB, the accuracy tends to be a constant around 0.23 m (the same accuracy as for the noise-free case).

A.3) Moving average filter + averaging of location vector

Figure 2.19 shows the results of combining the moving average filter and averaging of the location vector together; it can be seen that the results behave not as good as using coherent accumulation method when the SNR is extremely low (-20 dB). However, adding the averaging of the location vector method to the moving average filter can improve accuracy when the SNR is relatively high. Moreover, there is a trend that when the SNR is between 10 dB and 20 dB, the accuracy even gets higher than for the

noise-free case (around 0.23 meters). This is because when the SNR is around 20 dB, the contribution from the moving average filter has made the signal behave like a noise-free case (shown in Fig. 2.17, when the error went to 0.23 meters); thus each trial used for TDOA localization has the same error, and it does not have a statistical property anymore. Table 2.10 shows the information used for the denoising study using moving average filter and averaging location vector.

Table 2.10. Information used for the denoising study using moving average filter and averaging location vector.

Target	A *z*-directed dipole is placed inside the closed region. The target position is (-5, 4) meters.
Method	Demodulation method, moving average filter, averaging location vector (50 trials).

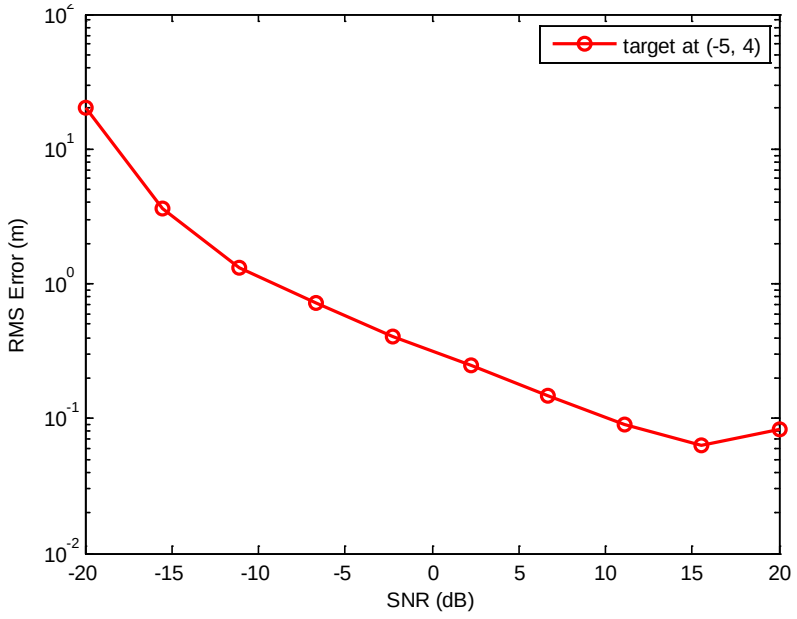

Figure 2.19. The RMS error (RMSE) under noisy conditions, versus the noise level (SNR), using a moving average filter and averaging of the location vector.

A.4) Moving-average filter + coherent accumulation +averaging of location vector

Combining the three methods together apparently has even more benefits for accuracy. As was explained in Section 2.4.2 A.3), contributions from coherent accumulation and the moving average filter make the noisy localization improve; thus as shown in Fig. 2.20, when the SNR is around 0 dB, the error reaches its smallest value. However, when the SNR is greater than 5 dB, the error begins to lose its statistical property, and more and more trials result in exactly the same estimated location vector. When the SNR is 20 dB, all trials result in the same location vector. Table 2.11 shows the information used for the denoising study using moving average filter, coherent accumulation and averaging location vector.

Table 2.11. Information used for the denoising study using moving average filter, coherent accumulation and averaging of the location vector.

Target	A *z*-directed dipole is placed inside the closed region. The target position is (-5, 4) meters.
Method	Demodulation method, moving average filter, coherent accumulation (16 trials), averaging location vector (50 trials).

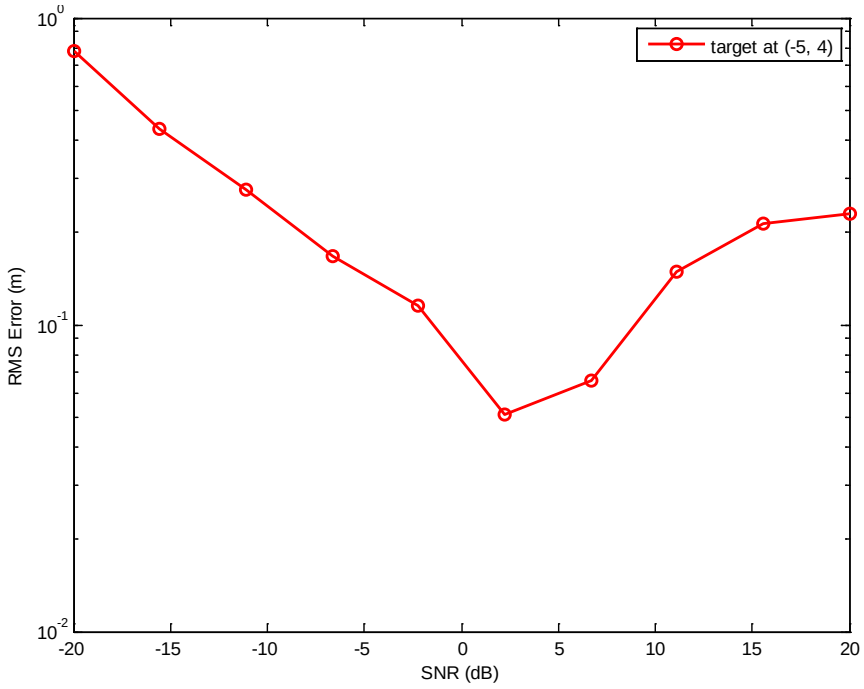

Figure 2.20. The RMS error (RMSE) under noisy conditions, versus the noise level (SNR), using coherent accumulation, a moving average filter, and averaging of the location vector.

B) Random time-shift effect for different trials used in coherent accumulation

In practical situations, each trial may possibly have a different time shift. Here we discuss the effect of having different time shifts for each trial.

B.1) Directly use time-shifted trials (baseline)

TDOA is to measure the time difference of arrival for the different receivers. When each receiver has a different added random time shift, this gives interference to the TDOA measurement. Table 2.12 shows information used for the time-shift study. Figure 2.21 shows how the TDOA then fails to locate the true target location.

Table 2.12. Information used for the different time-shift study.

Target	A *z*-directed dipole is placed inside the closed region. The target position is (-5, 4) meters.
Method	Demodulation method, moving average filter, coherent accumulation (16 trials), averaging location vector (50 trials). A random time shift is used for each trial (maximum is 10% of the time sequence) .

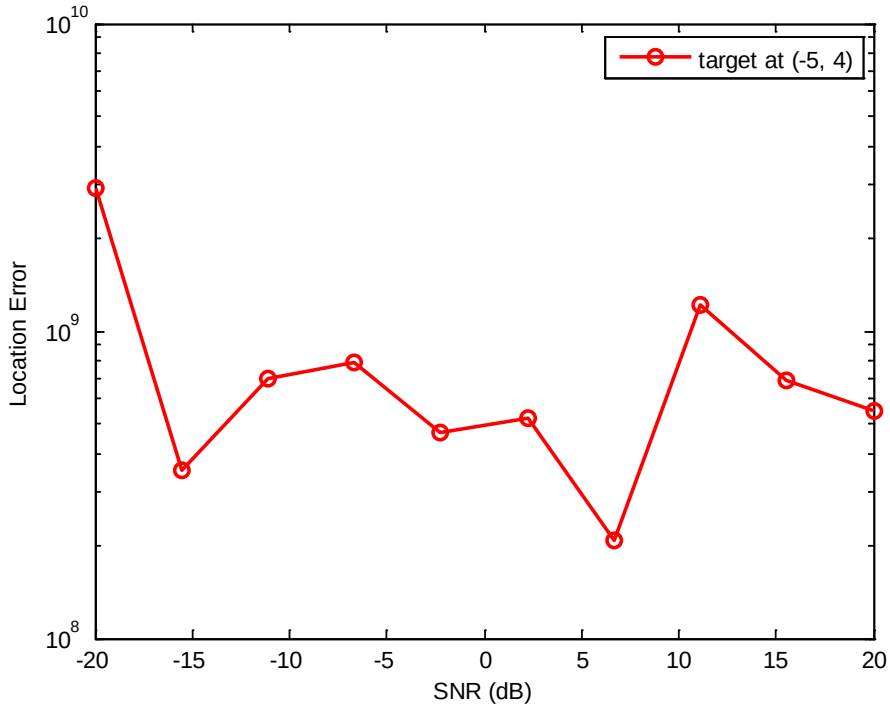

Figure 2.21. Localization error versus SNR (dB) under the condition that each trial used in the accumulation has a different time shift.

B.2) Use cross-correlation to offset the time shift

Cross-correlation does not help when the SNR is lower than -20 dB. However, when the SNR is higher than -10 dB, the effect from the time shift is almost eliminated. Table 2.13 shows the information for the time shift effect study.

Table 2.13. Information used for the time shift effect study.

Target	A *z*-directed dipole is placed inside the closed region. The target position is (-5, 4) meters.
Method	Demodulation method, moving average filter, coherent accumulation (16 trials), averaging location vector (50 trials). A random time shift is used for each trial (the maximum 10% of the time sequence), a cross-correlation between the 1st and each subsequent trial is used to offset the time shift.

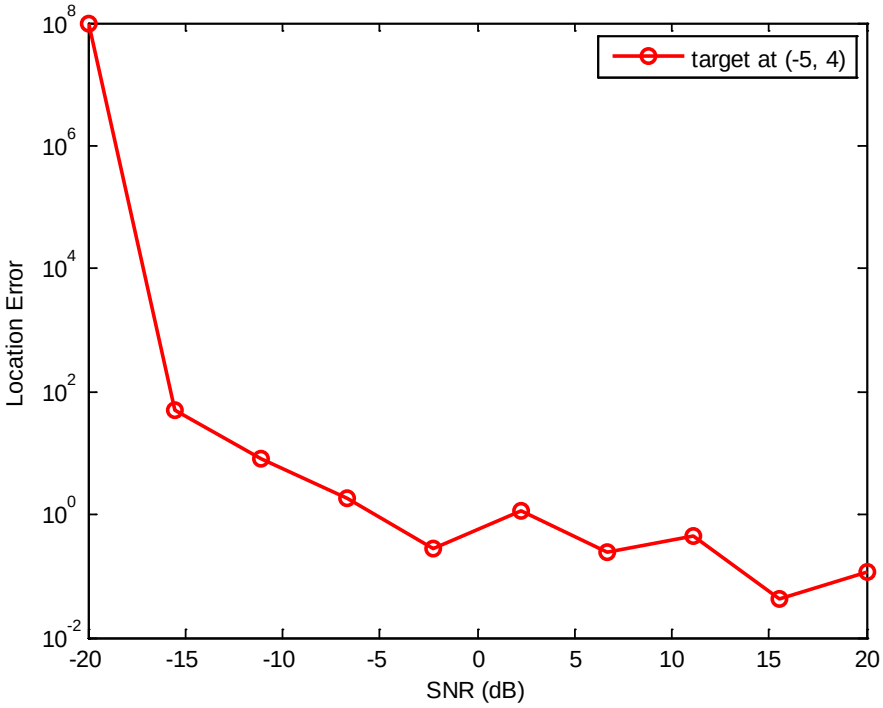

Figure 2.22. Localization error versus SNR (dB) under the condition of using the cross-correlation to offset the time-shift effect in the coherent accumulation process.

C) Number of coherent accumulation trials effect

Figure 2.23 shows that when the number of accumulated signals increases, the SNR needed to flatten the curves becomes lower. For the case when 64 trials are used, the lowest SNR needed to get the error to be constant is 5 dB. Table 2.14 shows the parameters for number of coherent accumulation trials effect study.

Table 2.14. Information used for number of coherent accumulation trials effect study.

Target	A *z*-directed dipole is placed inside the closed region. The target position is (-5, 4) meters.
Method	Demodulation method, moving average filter, coherent accumulation.
Compare	Number of trials for coherent accumulation: 2, 4, 8, 16, 32, 64.

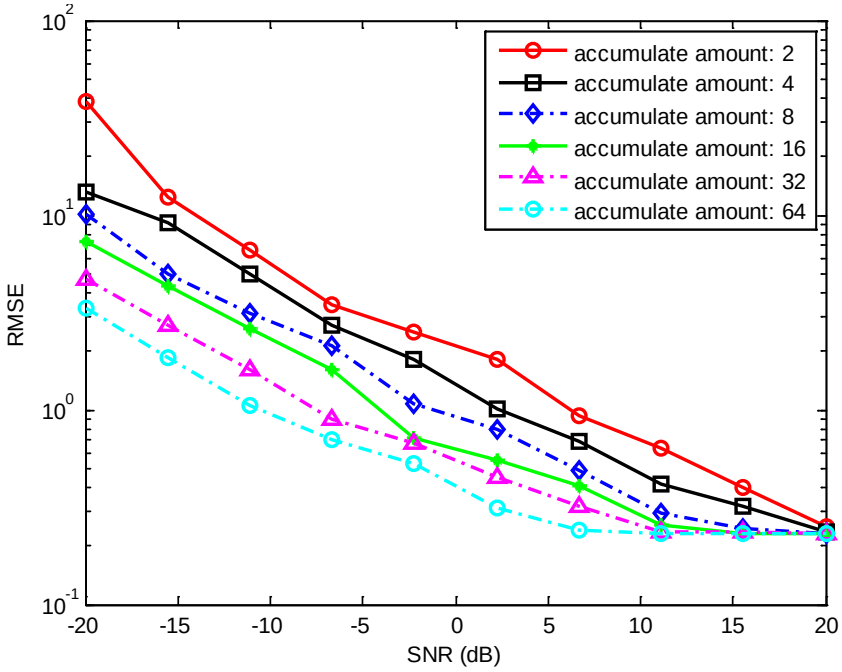

Figure 2.23. Comparison between different numbers of trials in coherent accumulation.

D) Number of averaging position vector trials effect

D.1) with coherent accumulation method

Figure 2.24 shows that accuracy increases in the localization results as more trials are used for averaging the location vector. Table 2.15 shows the information used for number of averaging of the position vector trials study.

Table 2.15. Information used for the number of averaging position vector trials study.

Target	A *z*-directed dipole is placed inside the closed region. The target position is (-5, 4) m.
Method	Demodulation method, moving average filter, coherent accumulation (8 trials), averaging location vector
Compare	Number of trials for averaging location vector4, 8, 16, 32, 64, 128.

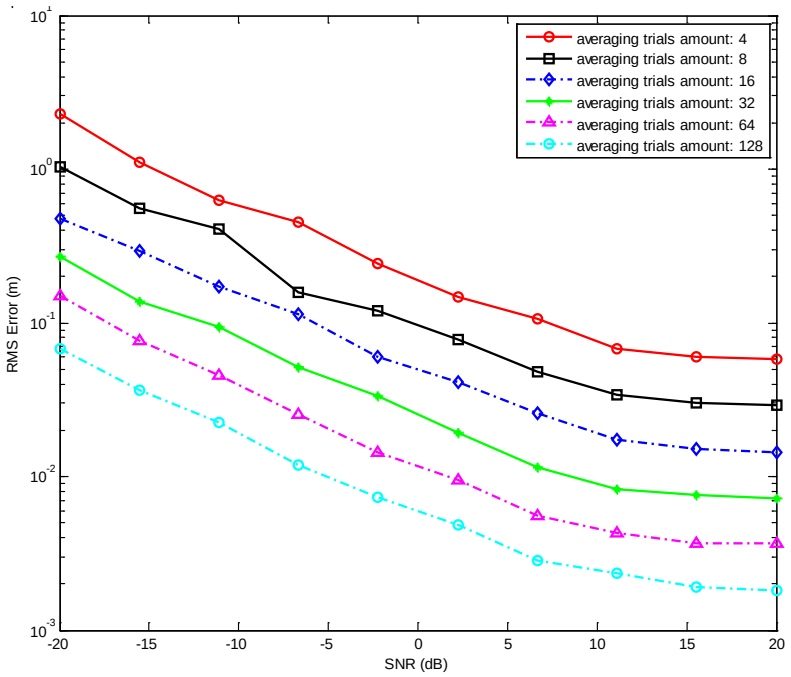

Figure 2.24. Comparison between different numbers of trials used in the averaging of the position vectors, with 8 trials applied to coherent accumulation.

D.2) without coherent accumulation method

Figure 2.25 shows that when there is no coherent accumulation involved, for extremely low SNR, the number of trials used in averaging the location vector will not affect the accuracy too much. The general trend is that when more trials are used, a higher accuracy will be achieved.

In Fig. 2.24, the black line represents the same number of trials as the blue-green line in Fig. 2.23, and the pink line in Fig. 2.25. By comparing the results represented by these three lines, we can conclude that separating trials into both methods can achieve better accuracy than simply applying either of these two methods to all of the trials. Table 2.16 shows the information used for number of averaging position vector trials study.

Table 2.16. Information used for number of averaging position vector trials study.

Target	A *z*-directed dipole is placed inside the closed region. The target position is (-5, 4) meters.
Method	Demodulation method, moving average filter, averaging location vector.
Compare	Number of trials for averaging location vector: 4, 8, 16, 32, 64, 128.

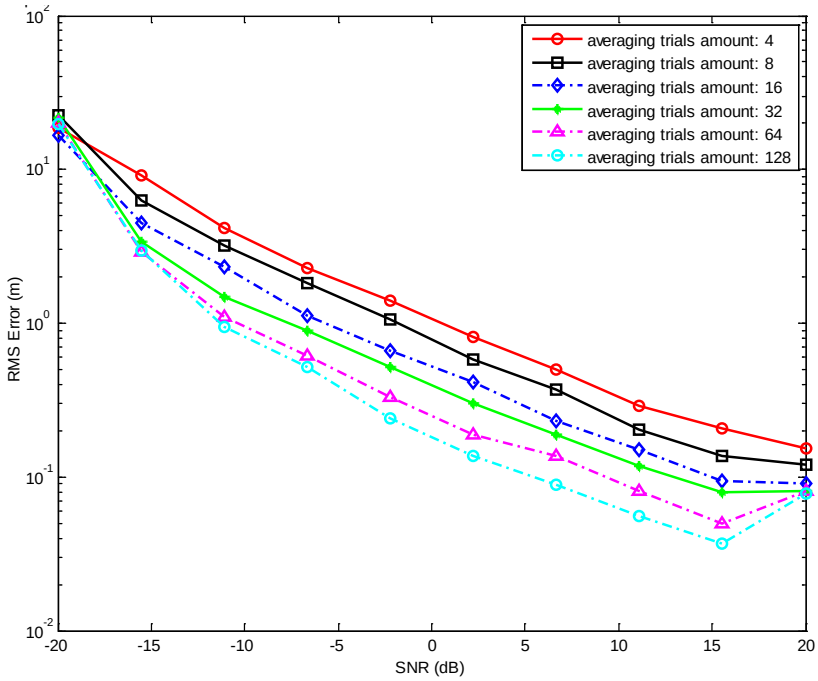

Figure 2.25. Comparison between different numbers of trials in the averaging of the position vectors, without coherent accumulation.

2.5 Conclusion

In this chapter, the flow chart of the TDOA implementation is provided. The details of the signal modeling and the TDOA determination and localization are presented in detail. Several denoising methods are also discussed.

Section 2.4 gives the detailed results and discussion. We conclude that, in the absence of noise, the location error is due to error in the cross-correlation process, and this error is inversely proportional to the sampling frequency. When using a moderate sampling frequency, the demodulated method is more accurate than using the original modulated signal. When the sampling frequency is high enough, both methods give almost the same error (which is determined mainly by the sampling frequency). The resolution bit needs to be higher than 5 in order to have a minimal effect on the

localization accuracy. The localization accuracy is limited by GDOP. The larger the aperture of the sensors is, the more accurate the localization is.

Under noisy conditions, the SNR should be higher than about 20 dB in order to obtain a result that is not significantly affected by the noise. When the SNR is high enough, an increase in the sampling frequency will improve the localization accuracy considerably.

The use of a moving average filter, coherent accumulation, and averaging of the location vector can improve the TDOA localization accuracy in the presence of noise.

Regarding the efficiency of the denoising methods, given a certain number of trials, when the SNR is extremely low, applying the coherent accumulation method to all of the trials is more efficient than applying the vector location averaging vector method to all of the trials. However, when the SNR is higher than 0 dB, applying the vector location averaging process to all of the trials is more efficient. Splitting the trials into both methods usually gives the best accuracy.

Chapter 3

TDOA Localization with Generalized NLOS Effects

Chapter 3 proposes a novel de-embedding transfer function concept based on traditional TDOA localization. The transfer function of the propagation system is introduced in Section 3.1, and then a global search method and an iterative method are defined using the processed signals (signals obtained after de-embedding the corresponding transfer functions). Sections 3.2, 3.3 and 3.4 present localizations using the iterative method for a refraction problem, a near field problem, and a scattering problem.

3.1 Overview of Proposed Algorithms

The TDOA localization process for an NLOS condition (e.g., with one or more walls present) is essentially the same as for a case without NLOS effects. The overview of the implementation is as shown in Fig 3.1. The main difference is that the propagation system now includes obstacles and hence the signal at the receivers is not the same as it would be for the free-space case without such obstacles.

The signal is modulated at the target, and travels through the NLOS propagation system to be received by the receivers. In the receiver part, the signal is sampled by an analog-to-digital converter, and then demodulated by a low-pass filter. The proposed “processed signal” is formed by manipulating the received signal and the transfer function of the propagation system. A cross-correlation is used to determine the TDOA between the processed signals at any pair of receivers and then the Levenberg–Marquardt algorithm is used to determine the source position by minimizing the objective function associated with the unknown source position.

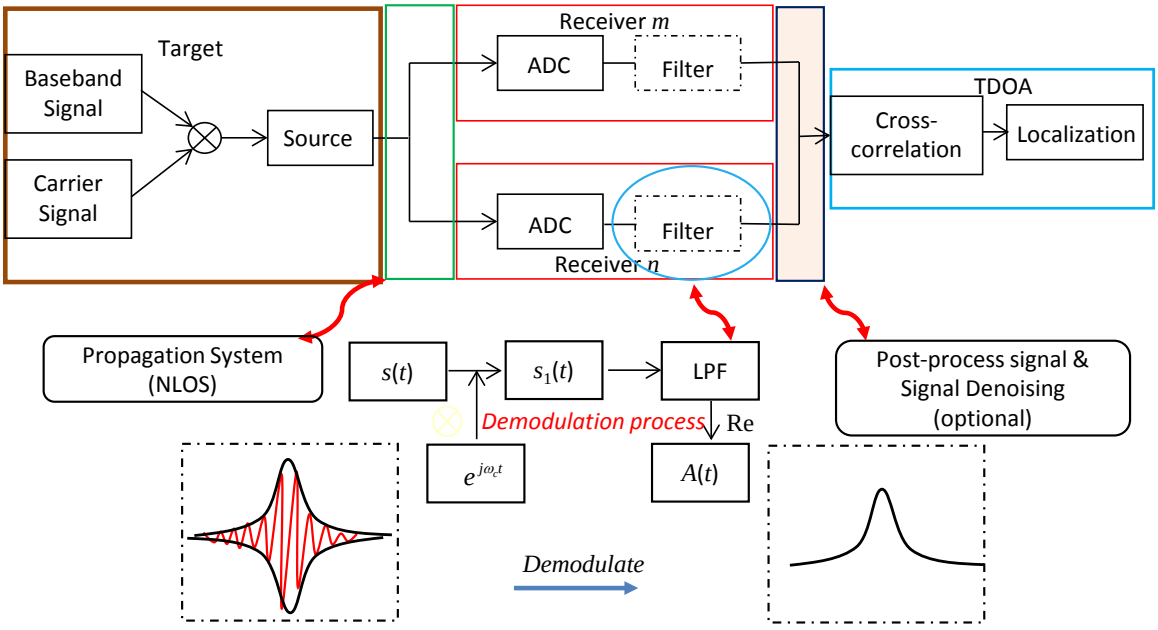

Figure 3.1. Algorithm for source localization using the processed signal.

3.1.1 Introduction of Transfer Function

The usual TDOA localization method, as mentioned in Chapter 2, is based on the assumption of free-space (line of sight) propagation. This is obviously not the case when a wall (or other obstacles, as shown in Fig.1.1) are present. The presence of an obstacle will therefore add error to the TDOA source localization, unless it is accounted for. The transfer function for the complete propagation system, including the obstacle, is already used to determine the signal at the receivers. In the direct TDOA method, this is the only way in which the transfer function is used. That is, the TDOA method proceeds just as it does without an obstacle, but uses modified signals at the receivers that account for the presence of an obstacle. This simulates source localization using the direct TDOA method (which neglects any obstacle) on measured receiver data that includes obstacle effects. The more an obstacle disturbs the signal at the receivers, the greater the source localization error will be.

However, the transfer function can also be used to remove the effects of an obstacle, so that the usual (LOS) TDOA method becomes exact (in the absence of noise), even though an obstacle (or other NLOS effect) is present. This is done by "de-embedding" the transfer function from the received signals. In essence, with this method we modify the received signals to emulate what the receivers would have received had there been no obstacle present. That is, we remove the obstacle effects, and calibrate the channel back to free-space propagation. Therefore, the usual direct (LOS) TDOA method becomes exact (in the absence of noise). In principle, the approach can account for any NLOS effects. This includes the effects of multiple walls (the entire building enclosure), a realistic ground, the presence of scattering objects in the environment, etc.

The transfer function in the TDOA problem relates the received and transmitted signals in the phasor domain as

$$T\left(\omega, \underline{r}, \underline{r}'\right) \equiv \frac{V_R\left(\omega\right)}{V_T\left(\omega\right)}, \tag{3.1}$$

where V_R is the received voltage and V_T is the transmitted voltage at frequency ω, with the transmitter located at $\underline{r}'$ and the receiver located at $\underline{r}$. The received signal is given in the transform domain by (a tilde denotes Fourier transform)

$$\tilde{v}_R\left(\omega\right) = \tilde{v}_T\left(\omega\right) T\left(\omega, \underline{r}, \underline{r}'\right), \tag{3.2}$$

and in the time domain by

$$v_R\left(t\right) = F^{-1}\left\{\tilde{v}_T\left(\omega\right) T\left(\omega, \underline{r}, \underline{r}'\right)\right\}, \tag{3.3}$$

where F^{-1} denotes inverse Fourier transform. To de-embed the transfer function, we define a "processed" transform of the received signal at one of the receivers as

$$\tilde{v}_R^p(\omega) \equiv \tilde{v}_R(\omega)\left(\frac{e^{-jk_0|\underline{r}-\underline{r}'|}}{T(\omega,\underline{r},\underline{r}')}\right), \tag{3.4}$$

so that

$$\tilde{v}_R^p(\omega) = \tilde{v}_T(\omega)e^{-jk_0|\underline{r}-\underline{r}'|}. \tag{3.5}$$

This means that

$$v_R^p(t) = v_T\left(t - c/|\underline{r}-\underline{r}'|\right). \tag{3.6}$$

There is thus no distortion of the processed received signal relative to the transmitted signal -- only a time delay based on the LOS distance between the transmitter and the receiver. Hence, the TDOA method should give perfect localization with no error (in the absence of noise). Hence, in the TDOA method, when doing the cross-correlation, the "processed" received signals should be used instead of the actual received signals. The processed received signal for any given receiver is defined by

$$v_R^p(t) \equiv F^{-1}\left\{\tilde{v}_R(\omega)\left(\frac{e^{-jk_0|\underline{r}-\underline{r}'|}}{T(\omega,\underline{r},\underline{r}')}\right)\right\}. \tag{3.7}$$

Note that if there is no wall or other NLOS effect, there would be only a time delay between transmitter and receiver; the transfer function would then be

$$T(\omega,\underline{r},\underline{r}') = Ae^{-jk_0|\underline{r}-\underline{r}'|} \tag{3.8}$$

for some constant *A* (which depends on the distance between the transmitter and receiver) so that

$$v_R^p(t) = v_R(t)/A. \tag{3.9}$$

In this case the processed received signal would be a scaled version of the actual received signal. Therefore,

$$v_R(t) = Av_R^p(t) = Av_T\left(t - c/\left|\underline{r} - \underline{r}'\right|\right). \tag{3.10}$$

Thus, if there is no wall or other NLOS effect, the de-embedded transfer function method reduces to the usual LOS direct TDOA method.

A limitation of the proposed approach, i.e., de-embedding the transfer function, is that the transfer function is a function of both transmitter and receiver locations. Therefore, in reality we do not know the transfer function unless we already know the target location; and of course if we already know the target location, then there is no point in doing the source localization. However, even if we have an approximate transfer function, it may help with the TDOA localization compared to using the original (unprocessed) received signals. This is the basis of the global search method and iterative method that are discussed in Section 3.1.2 and Section 3.1.3.

3.1.2 Global Search Method

Here we formulate the general improved TDOA method, allowing for an arbitrary transfer function, and an arbitrary orientation of the transmitting source. (In this dissertation the target dipole is a *z*-directed electric dipole, but the discussion below allows for an arbitrary dipole orientation.)

Note that the processed signal at each receiver is a function of the (unknown) coordinates (x, y) of the transmitting target and the unknown orientation (θ, ϕ) of the transmitting target source. The source is assumed to be modeled as a single equivalent electric dipole.

We initially assume a given (fixed) orientation (θ, ϕ) of the transmitting source (e.g., a vertical dipole). A cross-correlation is calculated between each pair of receivers (i, j), using the processed received signals:

$$C_{ij}\left(\tau;x,y\right)\equiv\int_{-\infty}^{\infty}v_{Ri}^{p}\left(t\right)v_{Rj}^{p}\left(t+\tau\right)dt\,. \tag{3.11}$$

We then denote

$$f\left(\tau\right)\equiv C_{ij}\left(-\tau;x,y\right)=\int_{-\infty}^{\infty}v_{Ri}^{p}\left(t\right)v_{Rj}^{p}\left(t-\tau\right)dt\,. \tag{3.12}$$

Usually, in the cross correlation definition, there is a conjugate on the first function in the above integral, but we ignore this here since we are working with real-valued signals. (For the processed signals, the time-domain processed signal is forced to be real-valued by enforcing the spectrum for negative frequencies to be the conjugate of the spectrum for positive frequencies. This is done in the inverse FFT routine used in MATLAB by virtue of the appropriate option selected in the FFT routine.)

Although the cross correlation is computed in the time domain (using MATLAB), it is possible to also cast the calculation in the frequency domain. This can be done by using the Fourier transform of the cross correlation, which is

$$\tilde{f}\left(\omega\right)=\left(\tilde{v}_{Ri}^{p}\left(\omega\right)\right)^{*}\tilde{v}_{Rj}^{p}\left(\omega\right); \tag{3.13}$$

hence, we have

$$\tilde{f}\left(\omega\right)=\left(\tilde{v}_{Ri}\left(\omega\right)\left(\frac{e^{-jk_0\left|\underline{r}_i-\underline{r}'\right|}}{T\left(\omega,\underline{r}_i,\underline{r}'\right)}\right)\right)^{*}\tilde{v}_{Rj}\left(\omega\right)\left(\frac{e^{-jk_0\left|\underline{r}_j-\underline{r}'\right|}}{T\left(\omega,\underline{r}_j,\underline{r}'\right)}\right). \tag{3.14}$$

The cross correlation is then

$$C_{ij}\left(-\tau;x,y\right)=F^{-1}\left\{\left(\tilde{v}_{Ri}\left(\omega\right)\left(\frac{e^{-jk_0\left|\underline{r}_i-\underline{r}'\right|}}{T\left(\omega,\underline{r}_i,\underline{r}'\right)}\right)\right)^{*}\tilde{v}_{Rj}\left(\omega\right)\left(\frac{e^{-jk_0\left|\underline{r}_j-\underline{r}'\right|}}{T\left(\omega,\underline{r}_j,\underline{r}'\right)}\right)\right\}. \tag{3.15}$$

The time delay TDOA_{ij} between receivers *i* and *j* (the time it takes for the signal to reach receiver *i* minus the time it takes for the signal to reach receiver *j*) is that if there

was no wall or other NLOS effect); this is found from the value of τ_{max} that maximizes the cross- correlation, using τ_{max} = -TDOA$_{ij}$. Each potential target position (x, y) has a corresponding objective function that is defined, as in the usual TDOA method, as

$$F\left(x,y;\theta,\phi\right)=\sum_{i=1}^{N}\sum_{j\neq i}\left[c\cdot TDOA_{ij}-\left(\begin{array}{l}\sqrt{\left(x_i-x\right)^2+\left(y_i-y\right)^2}\\-\sqrt{\left(x_j-x\right)^2+\left(y_j-y\right)^2}\end{array}\right)\right]^2. \qquad (3.16)$$

The objective function is zero at the true target location, since for this location the processed signals at the receivers will be equal to the signals that the receivers would have received had the target been transmitting in free space from that point. The target location (x, y) that minimizes the objection function in Eq. (3.16) is taken as the estimate of the true target location. In the absence of noise, this estimate will always yield the true target location. The minimization thus requires a global minimization search over the domain of interest (e.g., an enclosed region where the target is known to reside). Hence, by using the processed signals instead of the actual received signals, we propose an improved TDOA method, allowing for an arbitrary transfer function, called the global search method.

Ideally, if the search mesh is fine enough, this method will always give the exact target location in the absence of noise, though it will be much more time-consuming. In order to reduce the calculation time, a variation of the global-search method shown in Fig. 3.2 is actually used. Basically, the idea is to refine the search mesh locally in an iterative fashion, which saves time compared with searching over a finely meshed entire domain. This can work effectively when the transfer function is smooth over the entire domain of interest.

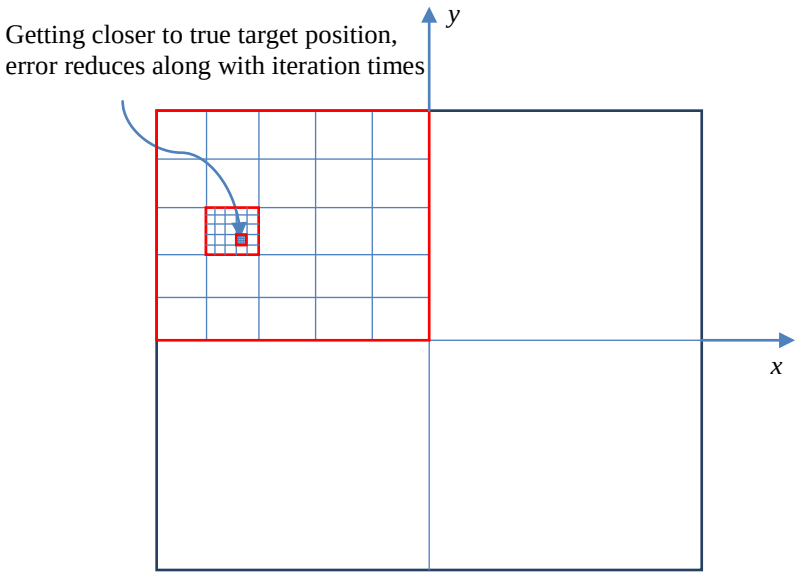

Figure 3.2. An illustration of the iterative mesh refinement that is used in the global search method.

The estimate of the target location (x, y) is based on the assumption of a given orientation (θ, ϕ) of the transmitting target. After the best estimate of the target location is obtained from the cross-correlation assuming a given source orientation, a new orientation of the transmitting target can be assumed and the process can be repeated. The orientation that gives the lowest overall value of the objective function would be the overall best estimate for the orientation of the transmitting source; the estimated target location (x, y) that corresponds to the optimum orientation would be the best overall estimate of the target location. This improved TDOA localization method can also be extended to 3D localization if four receivers are used.

3.1.3 Iterative Method

The method described above is accurate but time-consuming, as it requires a global search over the region of interest, and for each (x, y) point in the region the

transfer function $T(\omega, \underline{r}, \underline{r}')$ needs to be computed. Even though refining the search mesh locally in an iterative fashion (iterative mesh refinement) helps, the method can still be time consuming. An iterative method is proposed here to accelerate the search.

In the iterative method, an initial guess is made for the target location. The initial guess may be obtained using the usual TDOA method, neglecting the NLOS effects of the obstacle or enclosure. A transfer function is then computed for this target location at each of the receivers, and processed signals are calculated at the receivers. The cross-correlation (used to determine the TDOA between a pair of receivers) is calculated using the processed signals at each step (where the estimated target location is denoted as $\underline{r}' = \underline{r}_n$) as follows:

$$\begin{aligned} C_{ij}(-\tau; x_n, y_n) &\equiv \int_{-\infty}^{\infty} v_{Ri}^{p}(t)\, v_{Rj}^{p}(t-\tau)\, dt \\ &= F^{-1}\left\{ \tilde{v}_{Ri}(\omega)\left(\frac{e^{-jk_0|\underline{r}_i - \underline{r}_n|}}{T(\omega, \underline{r}_i, \underline{r}_n)} \right) \tilde{v}_{Rj}(\omega)\left(\frac{e^{-jk_0|\underline{r}_j - \underline{r}_n|}}{T(\omega, \underline{r}_j, \underline{r}_n)} \right) \right\}. \end{aligned} \tag{3.17}$$

Using the TDOA from the processed signals at the receivers, the usual TDOA method is applied again to search for an improved target location. Once the improved target location is found, a new transfer function is calculated at the receivers, and new processed signals are calculated, and the TDOA method is applied again. The process continues until the algorithm converges to a fixed point, which is then the estimated target location, or until it is clear that the process is not converging. This whole process is called the iterative method. A flow chart of the iterative algorithm is shown in Fig. 3.3. If the transfer function is accurate, the iterative method will converge to the true target position in the absence of noise, provided the initial guess is good enough.

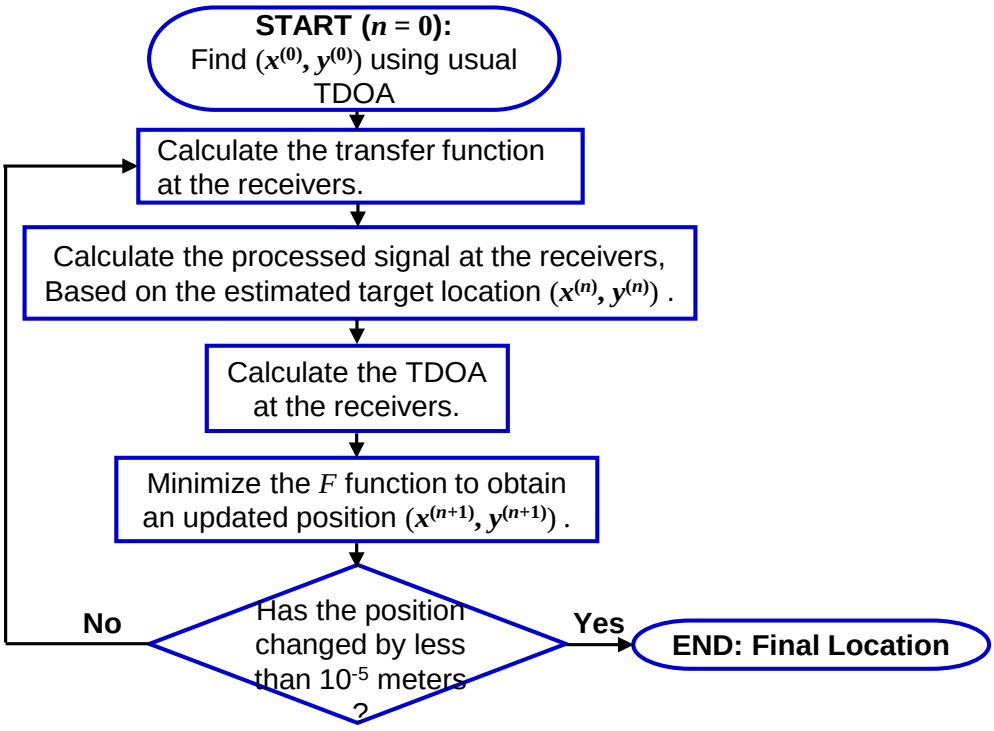

Figure 3.3. Flow chart showing the steps in the iterative method.

3.2 NLOS Effects Due to Refraction

3.2.1 The Single-Wall Model

Figure 3.4 shows a 3D view of the ray propagation route for the single-wall model, a typical refraction case from NLOS effects. As can be seen, the receiver and the target are assumed to be located on different sides of the wall. The target is inside a given region of interest. The wall's dimension and parameters are assumed. The reciprocity algorithm can be applied to obtain the transfer function that relates the field at the receiver to the field at the target when the receivers are put in the far field.

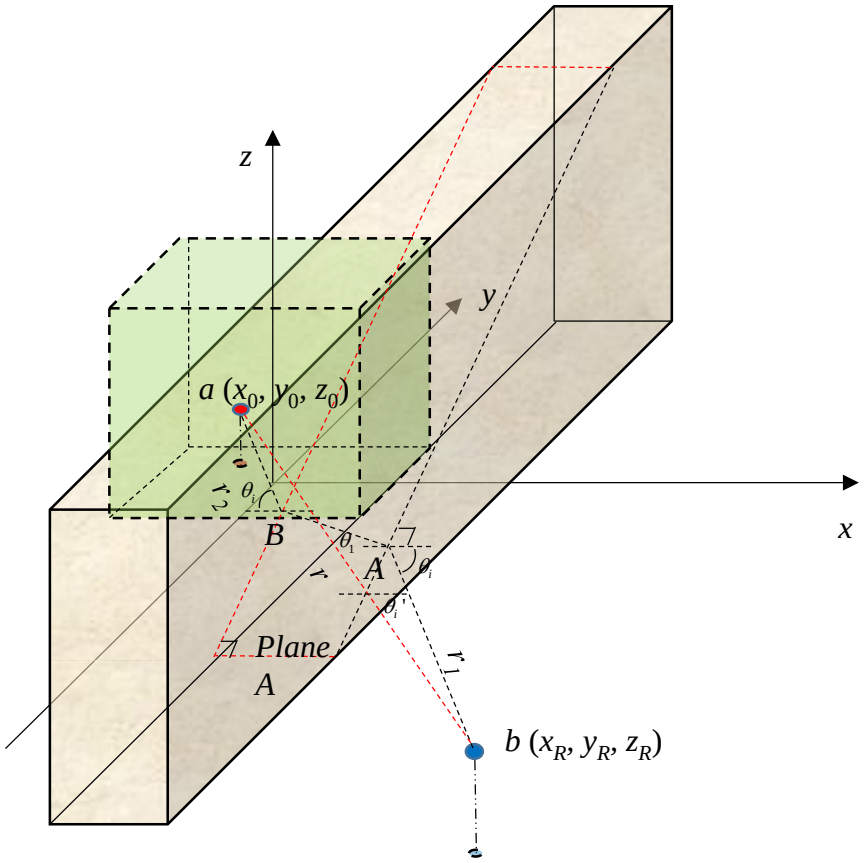

Figure 3.4. 3D view of signal propagation from target *a* (inside of a specified domain) to a receiver *b*, for the case of an infinite wall.

In the actual setup shown in Fig. 3.4, the target is the transmitting object and the signal is calculated at the position of one of the receivers in the TDOA method. However, in the reciprocity method we view the signal as being sent from the receiver and measured at the target. Reciprocity implies that these two situations are equivalent, but the receivers are typically further from the wall than the target is, and therefore it is more convenient to think of the signal as emanating from the receiver, so that the spherical wave that is being radiated will be closer to a plane wave as it impinges on the wall. This ensures that plane-wave theory, used to account for the presence of the wall, will be as accurate as possible.

Because of the PEC ground assumption, image theory can be applied to remove the ground, and create a wall that is infinite in the z direction. The transverse equivalent network (TEN) is then used to model the plane wave propagation through the wall to reach the target [45]. This allows us to calculate the transfer function $T(\omega, \underline{r}, \underline{r}')$ between a source at $\underline{r}'$ (a receiver) and an observer at $\underline{r}$ (the target). By reciprocity, we can then think of this as the transfer function between a source at $\underline{r}'$ (the target) and an observer at $\underline{r}$ (a receiver).

On the other hand, an accurate near field method, the spectral domain immittance method [46], was applied in this model to make a comparison with the above-mentioned plane wave method. In this method, by reciprocity, the receiver is also treated as a current source, and the finite current sheet is represented as a set of infinite phased current sheets, which can be decomposed into two parts that launch a pair of plane wave as TM_z and TE_z mode, respectively. The z-direction electrical field (transfer function with dipole moment) would therefore be calculated and combined from these two modes.

Figure 3.5 shows the basic geometry of the TDOA situation, with the wall present. Three receivers are used, as can be seen. The assumptions used in the simulation are as follows:

- The geometry consists of a square domain (simulating a square building footprint) that is 30 meters by 30 meters, centered at the origin.
- A single vertical electric dipole is used as the source.
- The dipole radiates a carrier wave (sinusoidal wave, 300 MHz) that is modulated by a lower frequency baseband Gaussian signal (1 MHz).
- The receivers are located at a distance of 1 km from the origin.
- The receivers and target are all on a PEC ground for simplicity.

- The TDOA for a pair of receivers is estimated using a cross-correlation between the signals (or processed signals) obtained from each pair of receivers.

Three different parameters for the wall are assumed, with the thickness in all cases being 20 cm, with infinite length and height along *y* and positive *z* directions.

- Case 1: $\sigma = 0\ S/m \quad \varepsilon_r = 6.3 - j0.69$.
- Case 2: $\sigma = 0\ S/m \quad \varepsilon_r = 3.9 - j0.19$.
- Case 3: $\sigma = 0.04\ S/m \quad \varepsilon_r = 9 - j0.45$.

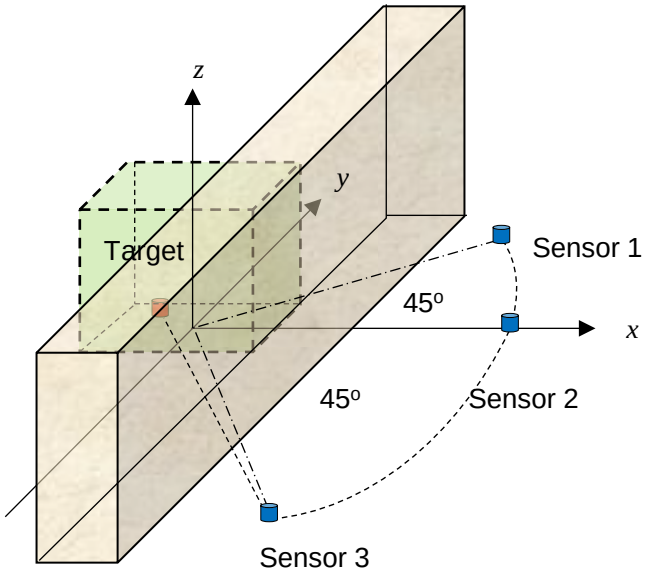

Figure 3.5. 3D view showing the positions of the target and receivers.

3.2.2 Derivation of Transfer Function

A) Reciprocity method

Figure 3.6 shows the geometry needed to obtain the transfer function after applying the reciprocity algorithm. The plane wave that impinges on the wall from the radiating receiver at (x_R, y_R) is polarized with the electric field in the *z* direction (vertical),

which is TE$_x$ polarization. The incident E_z field at point A from the radiating source (at the receiver location) in the far field is given by

$$E_A = \left(\frac{-j\omega\mu_0}{4\pi r_1} \right) e^{-jk_0 r_1}. \tag{3.18}$$

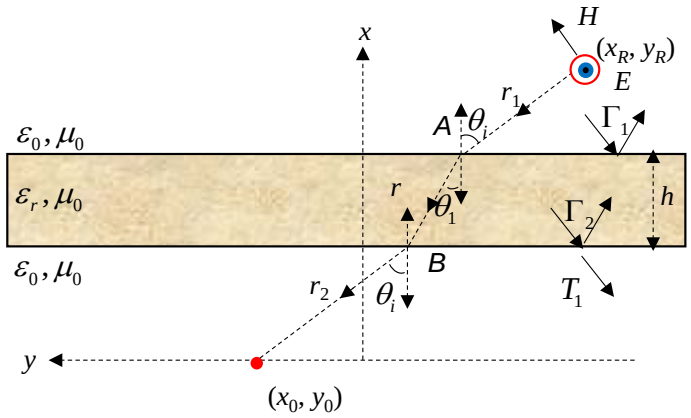

Figure 3.6. Top view of the single-wall model.

By using the transverse equivalent network (TEN) method [18], the various regions, including the wall, are modeled as transmission lines. The vertical electric field is modeled as voltage on the TEN, and a transmission-line calculation is used to obtain the voltage and hence the field at the target location. Omitting the calculation details, the transfer function is derived as

$$\begin{aligned} T(\omega, \underline{r}, \underline{r}') &= 2E_A T^{TE_x} e^{-jk_0 r_2} \\ &= -2\left(\frac{j\omega\mu_0 \cos(\theta_i)}{4\pi(x_R - h - \frac{L}{2})} \right) \cdot \left(\frac{1+\Gamma}{e^{+jk_{x1}h} + \Gamma_2 e^{-jk_{x1}h}} \right) \\ &\quad \cdot (1+\Gamma_2) e^{+jk_{x0}h} e^{-jk_0 r}. \end{aligned} \tag{3.19}$$

The factor 2 on the right-hand side is from image theory. The term T is the TE$_x$ transmission coefficient of the plane wave through the wall. The term Γ is the total TE$_x$

plane-wave reflection coefficient at point *A*, calculated from TEN. This includes the effects of the wall and the semi-infinite free-space region on the other side of the wall that the plane wave transmits into. The term Γ_2 is the interface TE_x reflection coefficient at point *B*, going from the wall region to the air region. The angle θ_i is the incident angle, and is taken as

$$\theta_i \approx \arctan\left(\frac{y_R - y_0}{x_R - x_0}\right). \tag{3.20}$$

The target is at (x_0, y_0), k_0 is the wavenumber in the air, and L length of the enclosure (30 meters here). Also, k_{x0} is the x component of the wavenumber in air, and k_{x1} is the x component of the wavenumber in the wall. Note that the angle θ_1 inside the wall will be complex for a lossy wall, but this causes no complication in the method. The detailed derivation is shown in Appendix A.1.

B) Spectral Domain Immittance Method

Assume that target *a* is located at (x_a, y_a, z_a), and sensor *b* is located at (x_b, y_b, z_b). After applying the reciprocity algorithm, the coordinate system is rotated and the origin's position is changed, as shown in Fig. 3.7. So we have $x_R = z_b$, $y_R = -y_b$, $z_R = x_b - L/2 - h$; $x_0 = z_a$, $y_0 = -y_a$, $z_0 = x_a - L/2 - h$. Here L is enclosed area's length.

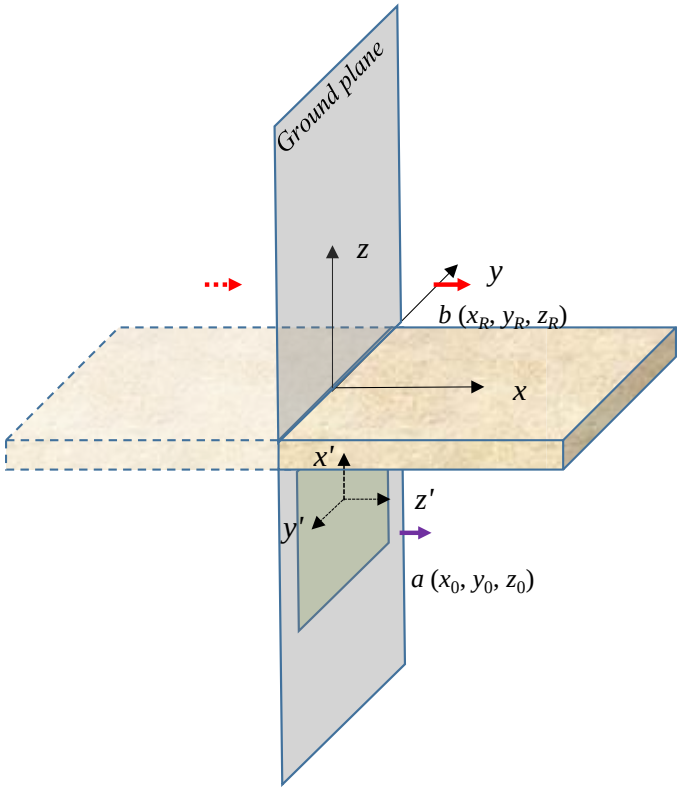

Figure 3.7. 3D view of the geometry after applying the reciprocity theorem.

Under the new coordinate system, the current source can be represented as follows, taking into consideration the ground effect:

$$\underline{J}_s\,|_{z=z_R} = \underline{\hat{x}}\begin{pmatrix} Il\delta\left(x-x_R\right)\delta\left(y-y_R\right) \\ +Il\delta\left(x+x_R\right)\delta\left(y-y_R\right) \end{pmatrix}. \tag{3.21}$$

The transverse equivalent network is shown in Fig. 3.8. A detailed derivation is provided in Appendix A.2.

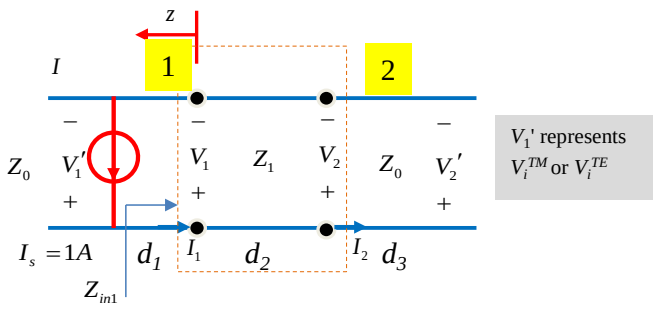

Figure 3.8. Transverse equivalent network for the SDI method.

Figure 3.8 shows the parameters needed to get a transfer function after applying the reciprocity algorithm and the SDI method. The final form of transfer function is expressed as

$$T(x_a, y_a, z_a) = -\int_{-\infty}^{\infty}\int_{-\infty}^{\infty} \frac{\cos(k_x z_b)}{2\pi^2 k_t^{\,2}} \left[k_x^2 V_i^{TM}\,|_{z=z_0} + k_y^2 V_i^{TE}\,|_{z=z_0} \right] \cdot e^{-j\left(k_x z_a + k_y(-y_a+y_b)\right)} dk_x dk_y, \tag{3.22}$$

where k_x is the x component of the wavenumber in air and k_y is the y component of the wavenumber in air. k_t is the transverse wavenumber in air. V_i^{TM} and V_i^{TE} denote the incident voltage at the target position in the TM_z and TE_z cases, respectively. We provide below comparisons of the transfer functions using the different methods.

1) Free space

In free space, the exact transfer function is simply found from the radiated field E_θ produced by an electric dipole:

$$E_\theta = \frac{Il}{4\pi}(j\omega\mu)e^{-jkr}\left(\frac{1}{r}\right)\left[1+\frac{1}{jkr}+\frac{1}{(jkr)^2}\right]\sin\theta. \tag{3.23}$$

Therefore, the transfer function is

$$T = -\frac{1}{4\pi}(j\omega\mu)e^{-jkr}\left(\frac{1}{r}\right)\left[1+\frac{1}{jkr}+\frac{1}{(jkr)^2}\right] \tag{3.24}$$

(the minus sign in the above equation is due to the fact that at the ground plane, $E_z = -E_\theta$.). Table 3.1 presents a comparison among the reciprocity method, the SDI method, and the exact transfer function. The target position is at (-1, -1, 0) meters.

Table 3.1 shows that the transfer function found by using the SDI method matches very well with the exact transfer function, but it is very time-consuming to compute, especially at higher frequencies (above tens of MHz). While the transfer function found from the reciprocity method is not quite as accurate as that from SDI, the reciprocity method is very efficient.

Table 3.1. Comparison between different transfer functions for free space.

Freq./Method	Exact	SDI	Reciprocity
300 KHz	-6.1027e-5-3.6728e-4j	-6.1026e-5-3.6733e-4j	-1.1069e-6-3.8582e-4j
3.3 MHz	-0.0001908-0.0041421j	-0.00019084-0.00414203j	-0.0001339-0.0042419j
33.3 MHz	-0.0131588-0.0397231j	-0.0131589-0.0397234j	-0.0134086-0.0406725j

2) Wall Case 3

Table 3.2 presents the comparison between the transfer functions from reciprocity and SDI, when a single-wall (Wall Case 3) is present in the propagation system. The transfer functions from SDI and reciprocity increasingly differ at higher frequencies. However, SDI is not practical at higher frequencies, as higher frequencies give higher

oscillation in spectral integration, making the integrals very time-consuming to converge. Hence, in the following sections (Section 3.2.3 ~3.2.8), all simulations are done using reciprocity when using the iterative method.

Table 3.2. Comparison among different transfer functions for Wall Case 3.

Freq./Method	SDI	Reciprocity
300 KHz	-6.6298e-5-3.645e-4*j*	-3.8301e-6-3.8482e-4*j*
1.6 MHz	-0.00056+ 0.00197*j*	-0.00060+0.00198*j*
3.3 MHz	-0.000415- 0.003920*j*	-0.000441-0.004094*j*
16.1MHz	0.0042+0.0157*j*	0.0025+0.0176*j*
33.3 MHz	-0.0162-0.0145*j*	-0.022-0.0187*j*

3.2.3 Sanity Check with Three Different Walls

Here comparisons are made between localization errors using the usual direct TDOA method (using the original received signals, with no transfer function accounted for) and using the iterative method (using the processed signals, with the transfer function accounted for). All of the simulations were implemented using an ADC sampling frequency of 100 GHz under noise-free conditions. The spatial sample points were on a 16×16 grid inside a 30 × 30 meter enclosure.

A) Wall Case 1

As shown in Fig. 3.9, the left side of the figure shows the error when using the usual direct TDOA method, while the right side of the figure shows the error when using the proposed iterative algorithm. The error range is reduced from 0.347 ~ 0.36 meters to 0.0001 ~ 0.0048 meters when we compare the usual direct TDOA method (which

neglects the wall) to our proposed iterative method (which accounts for the presence of the wall). This clearly shows the benefits of de-embedding the transfer function in the TDOA method.

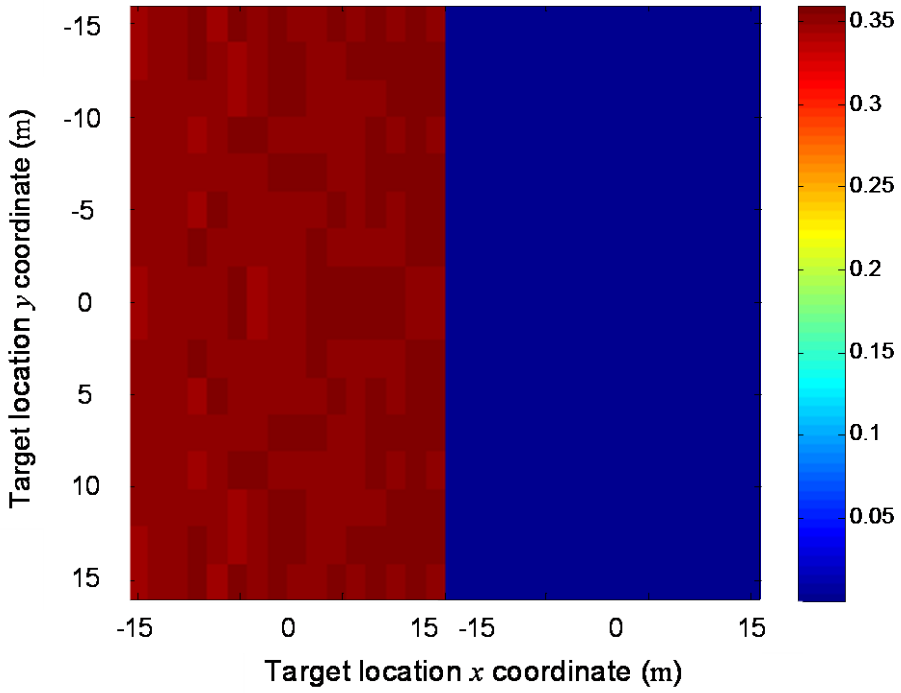

Figure 3.9. Localization error (in meters) comparison between different methods for Wall Case 1.

B) Wall Case 2

As shown in Fig. 3.10, the left side of the figure shows the error when using the usual direct TDOA method, while the right side of the figure shows the error when using the proposed iterative algorithm. Error range is reduced from 0.002 ~ 0.01 meters to 0.0001 ~ 0.0048 meters when comparing the usual direct TDOA method with the proposed iterative method. It is interesting to note that for Wall Case 2 the localization error when using the usual direct TDOA method is quite small (though, as with the other cases, it becomes even smaller when using the iterative method). It is thought that this is

a peculiar coincidence for Wall Case 2, partially related to the fact that wall permittivity is the lowest for Case 2, but perhaps also partially related to a “lucky” coincidence of wall parameters.

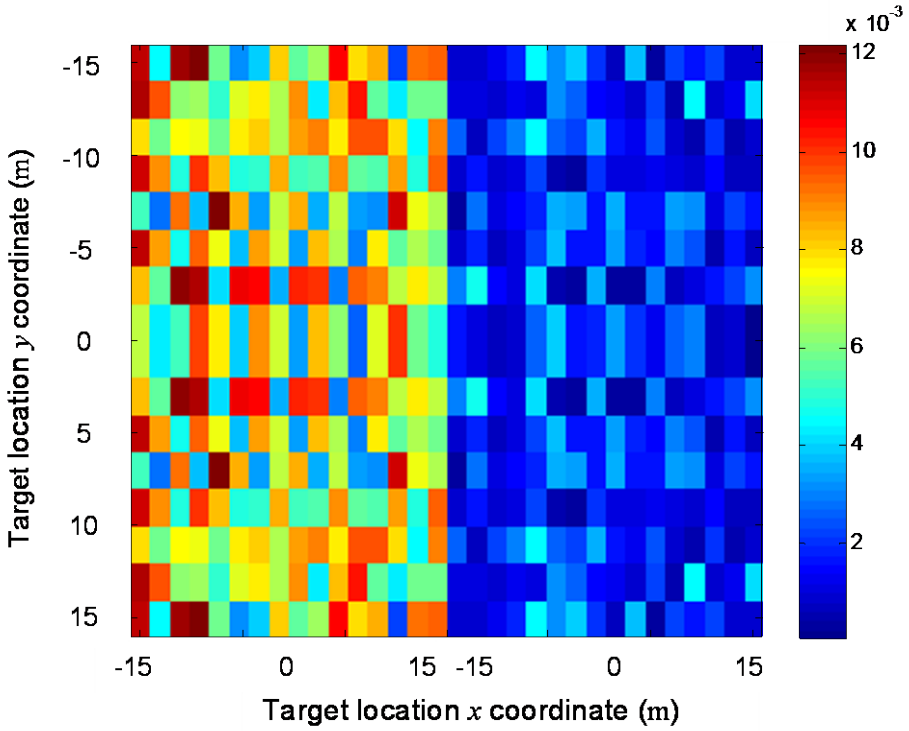

Figure 3.10. Localization error (in meters) comparison between different methods for wall Case 2.

C) Wall Case 3

As shown in Fig. 3.11, the left side of the figure shows the error when using the usual direct TDOA method, while the right side of the figure shows the error when using the proposed iterative algorithm. The error range is reduced from 0.176 ~ 0.185 meters to 0.0001 ~ 0.0048 meters when comparing the usual TDOA method with our proposed iterative method.

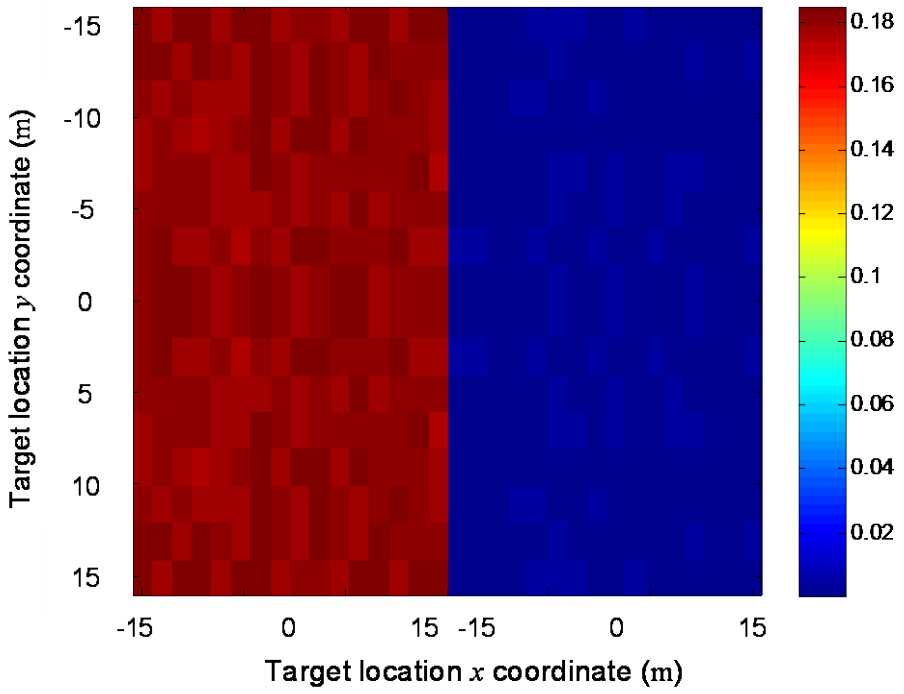

Figure 3.11. Localization error (in meters) comparison between different methods for wall case 3.

From Figs. 3.9 ~ 3.11, it can be seen that the localization error when using our proposed iterative method for the different walls is the same, which means that the wall parameters do not affect final accuracy when the iterative method is applied. This is because the wall is accounted for in the iterative method, so there is no error coming from the presence of the wall when using this method. The error in the iterative method results is only due to the finite (100 GHz) sampling frequency in the ADC.

In the next section, we discuss the sampling frequency effect when the iterative method is applied. The iterative method converges very fast (within 4 steps) if the transfer function is accurate enough.

3.2.4 Sampling Rate Effects

Table 3.3 shows the localization error using the proposed iterative method with different ADC sampling frequencies. The results are obtained for a target that is varied over the entire 30 × 30 meter region, allowing for all possible target positions.

Table 3.3. Localization error for different sampling rates.

f_{ADC} (GHz)	Ave. error (m)	Max. error (m)
100	0.0018	0.0048
50	0.0039	0.0095
10	0.0190	0.0482
5	0.0368	0.0855
2	0.0837	0.2179
1	0.2134	0.4965

Ave. denotes average; Max denotes maximum

Table 3.3 shows that localization accuracy using the proposed iterative method only depends on the ADC sampling frequency; the higher the sampling frequency, the lower the error; this is because a higher sampling frequency means a more accurate calculation of the TDOA in the cross-correlation between two signals obtained from a pair of receivers. A simple rule of thumb is error $\approx c / f_{ADC}$, where c is the speed of light.

3.2.5 Interpolation to Raise Low Sampling Rate

In order to improve the localization accuracy while lowering the numerical cost of the ADC, an interpolation method is used to increase the number of data points used in

the cross-correlation. The interpolation is applied together with a 1 GHz ADC sampling frequency in order to generate a much finer set of data points for the cross-correlation (corresponding to a 100 GHz density of points in the time sequence). The results are shown in Fig. 3.12.

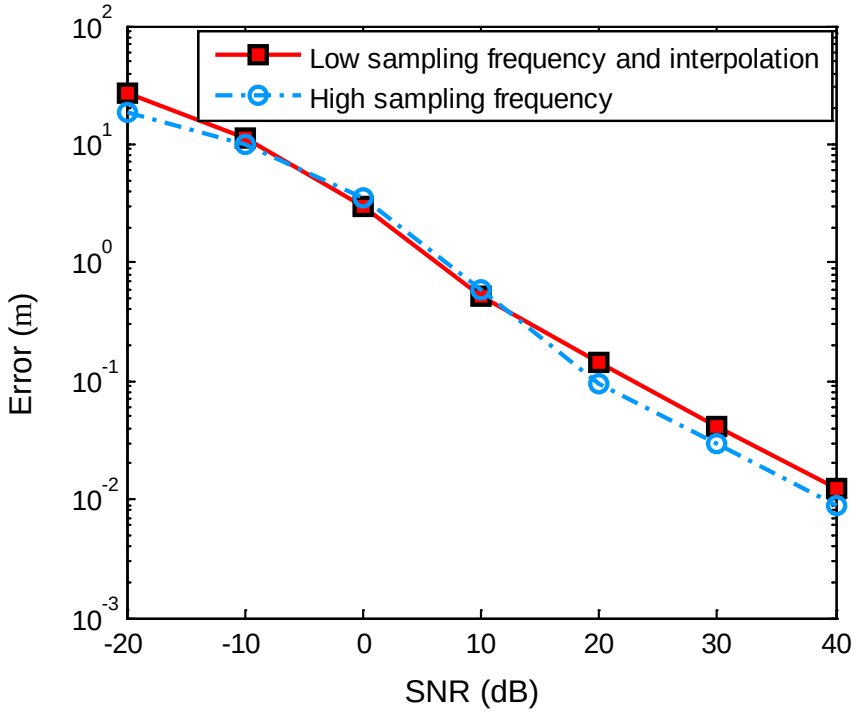

Figure 3.12. Error comparison between using a high ADC sampling frequency and a low ADC sampling frequency together with interpolation.

Figure 3.12 shows a simulation in free space that has Gaussian white noise added to the received signal. The average error (from a Monte Carlo simulation) is shown vs. the SNR, comparing results obtained with a very high ADC sampling frequency of 100 GHz vs. using a sampling frequency of only 1 GHz together with interpolation. The accuracy is approximately the same in both cases. Hence, interpolation is very effective in producing accurate cross-correlation results (and hence accurate TDOA results) from a fairly sparse set of samples in the original ADC sampling. The restriction is that the

initial sampling rate (before interpolation is applied) must still be high compared with the carrier frequency (at least twice the carrier frequency, from the Nyquist sampling theorem).

3.2.6 Influence from GDOP

According to Geometric Dilution of Precision (GDOP) [44], which was investigated in Section 2.4.3, the sensor layout geometry has an impact on localization accuracy. In particular, any errors get magnified during the localization process when the angular spread of the sensors is small. This is the GDOP effect. Even without added noise, the sampling frequency cannot be high enough to perfectly simulate the analog signal, and hence the cross-correlation calculation can always be seen as a numerical error source. Our iterative method effectively deals with the error brought about by NLOS effects, but error due to the cross-correlation still remains.

Simulations show that as long as the angular sensor array aperture is large enough (here the sensor aperture is 90°), the GDOP error is tolerable, and is on the order of millimeters.

3.2.7 Uncertainty of Parameters

Taking the wall parameters used in Section 3.2.3 (A) as a baseline example, the localization error due to uncertainties in the wall permittivity, conductivity, and thickness are examined here. Assuming that the parameters used in the localization have ±40%, ±20%, ±10%, ±5% deviation compared to the true values, the localization results after using the iterative method are shown in Table 3.4.

Table 3.4. Influence of uncertain parameters.

	+40%	+20%	+10%	+5%	-5%	-10%	-20%	-40%
ε_r'	0.116	0.059	0.027	0.013	0.010	0.017	0.015	0.040
ε_r''	0.006	0.003	0.002	0.002	0.002	0.002	0.003	0.006
σ	0.022	0.012	0.006	0.004	0.004	0.007	0.014	0.029
h	0.097	0.084	0.047	0.025	0.023	0.040	0.004	0.191

Ave. error after the iterative method (m) f_{ADC} = 100 GHz

+40% : 40% higher than the exact value, -40% :40% lower than the exact value

Using the usual TDOA method will give an average error of 0.2066 meters. After de-embedding the transfer function, if all parameters are accurate, the expected average error would be 0.0018 meters, as was shown in Table 3.4. Although the uncertainty lowers the accuracy, the results using the iterative method are still improved relative to the error in the usual TDOA method, which ignores completely the presence of the wall. The wall thickness and real part of the wall permittivity are the most sensitive parameters, as they affect the time delay of the signal the most.

Also of interest is the error in localization due to errors in the receiver location. If all receivers have the same error in radial distance r, then the localization error is minimal. However, if only one receiver position has uncertainty, or if the position error of the sensors is in a random direction, then the localization error is on the same order as the receiver position error.

3.2.8 Noisy Conditions

In the noise study, the target position is at (-5, 4) meters, and the sampling frequency is 100 GHz (to essentially eliminate TDOA errors in the cross-correlation). The Monte Carlo method is applied to study the effects of random noise (white additive Gaussian noise) when the wall is present. Error comparison between the usual TDOA method and the iterative method under noisy conditions with the wall present is shown in Fig. 3.13.

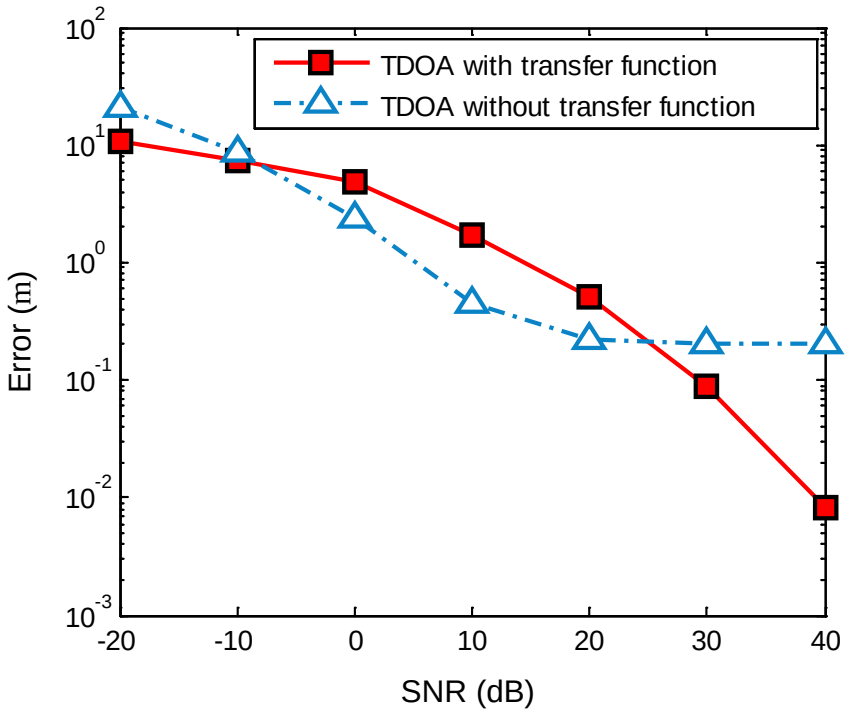

Figure 3.13. Error comparison between usual TDOA method and iterative method under noisy conditions with the wall present.

As shown in Fig. 3.13, as the SNR increases, the average error in the iterative method (averaged over the Monte Carlo trials) becomes very small, as expected. The usual TDOA method has an error that does not tend to zero as the SNR increases, since this method does not account for the wall effects. As the SNR becomes large, the error in

the direct TDOA method is seen to be about 0.2 m, consistent with the results in Fig. 3.12. However, the error in the iterative method results is larger than that for the direct TDOA method for smaller values of SNR (for SNR less than about 25 dB). A modified transfer function (discussed below) is introduced to overcome this problem, and results are shown in Fig. 3.14.

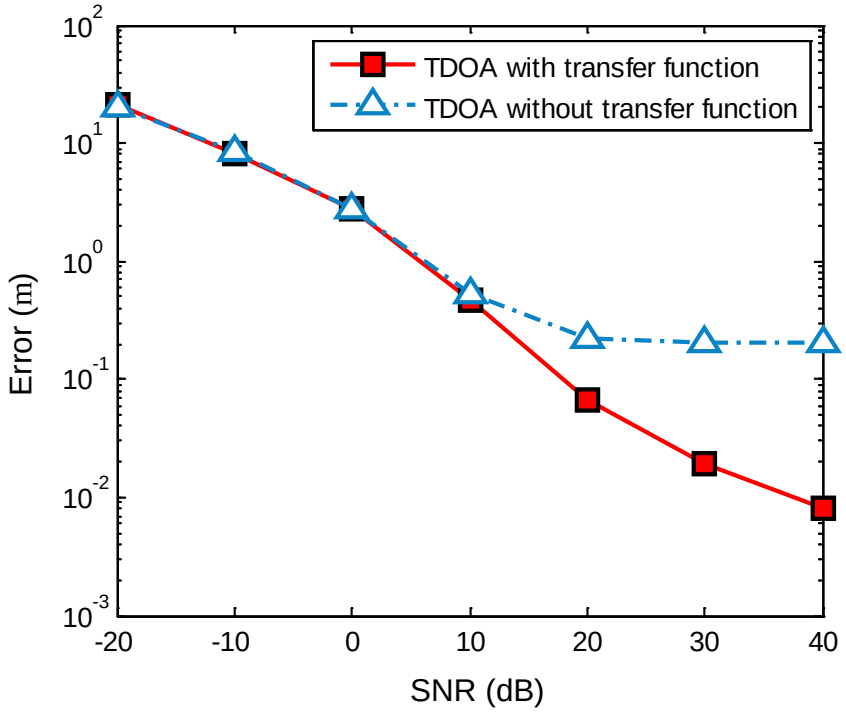

Figure 3.14. Error comparison between usual TDOA method and the iterative method with modified transfer function under noisy conditions with the wall present.

In free space, the exact transfer function is simply found from the radiated field E_θ produced by an electric dipole; therefore, the transfer function is

$$T = -\frac{1}{4\pi}(j\omega\mu)e^{-jkr}\left(\frac{1}{r}\right)\left[1+\frac{1}{jkr}+\frac{1}{(jkr)^2}\right]; \tag{3.25}$$

the minus sign in Eq. (3.25) is due to the fact that at the ground plane, $E_z = -E_\theta$. In Eq. (3.25), the free-space transfer function has a ω term in the far field, in addition to the

free-space propagation term e^{-jkr}; therefore, an ω term is introduced to obtain a modified processed signal as

$$\tilde{v}_R^p(\omega) \equiv \tilde{v}_R(\omega)\left(\frac{\omega e^{-jk_0|\underline{r}-\underline{r}'|}}{T(\omega,\underline{r},\underline{r}')}\right). \tag{3.26}$$

Figure 3.14 showed that after modification, the iterative method always yields results that are at least as good as the usual TDOA method; when the wall effects dominate the effects of the noises, the results from the iterative method are noticeably better than those of the usual TDOA method, which neglects the wall.

However, the additional ω term is not necessarily always beneficial. This probably depends on the source type and the received field.

3.3 Localization in the Near Field

3.3.1 The Near-Field Model

Figure 3.15 shows a 3D view of the near-field model; it gives a basic geometry of the TDOA situation, when the receivers are located in the near-field region of the target. As can be seen, three receivers are again used. The assumptions used in the simulation are as follows:

- The geometry consists of a square domain (simulating a square building footprint) that is 30 meters by 30 meters, centered at the origin.
- A single vertical electric dipole is used as the source.
- The dipole radiates a carrier wave (sinusoidal wave, 3 MHz) that is modulated by a lower frequency baseband Gaussian signal (1 MHz). So, the wavelength is about 100 m. The sampling frequency is still 100 GHz for the sanity check.
- The receivers are located at a distance of 50 m from the origin, and the angles to the *x* axis are 0°, 120°, -120°, respectively.

- The receivers and target are all on a PEC ground for simplicity.
- The TDOA for a pair of receivers is estimated using a cross-correlation between the signals (or processed signals) obtained from each pair of receivers.

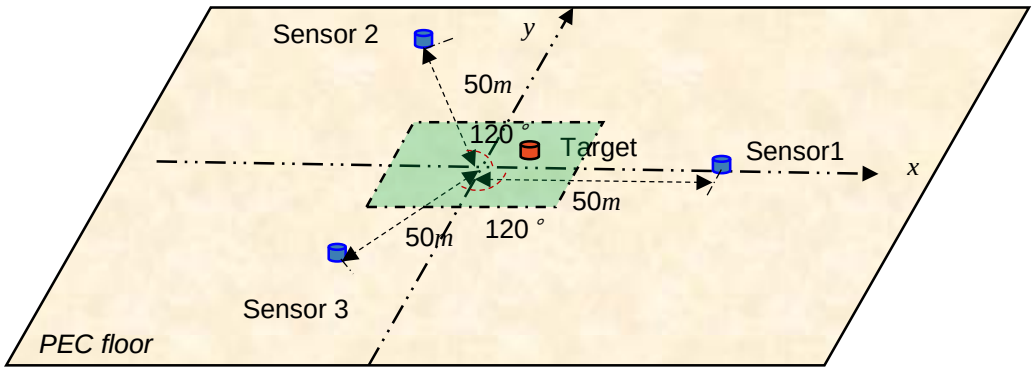

Figure 3.15. 3D view of the near-field model.

The transfer function is twice the transfer function, as shown in Eq. (3.25), since the PEC ground plane exists.

3.3.2 Sanity Check

In Fig. 3.16, the left side of the figure shows the error when using the usual direct TDOA method, while the right side of the figure shows the error when using the proposed iterative algorithm. The error range is reduced from 0.170 ~ 3.505 meters to 0.000026 ~ 0.0012 meters when comparing the usual direct TDOA method with the proposed iterative method.

The reason that the usual direct TDOA method's averaged error is much larger than that of the iterative method is that, in the near field, the signal is not propagating at the speed of light (the second and third term in the exact expression for the dipole field will distort the signal to some extent); this can be seen as a general NLOS effect. After applying the iterative method, the NLOS is removed, and thus distortions are eliminated.

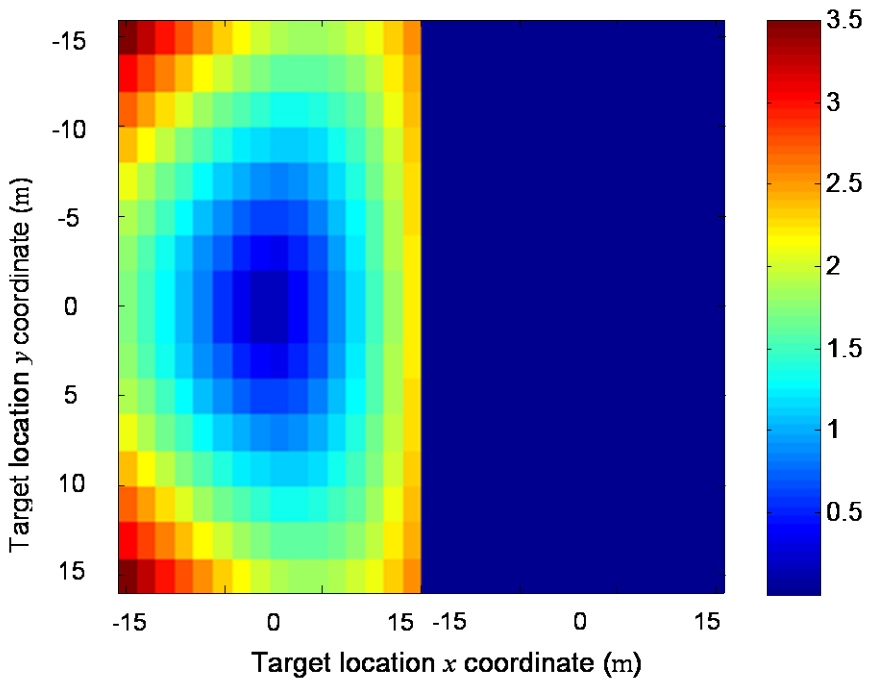

Figure 3.16. Localization error comparison (in meters) between different methods for the near-field model.

The sensor geometry is different here from the single-wall model; the GDOP influences localization accuracy even when using the iterative method (as mentioned in Section 3.2.6). Therefore, the error after using the iterative method in this near field condition differs slightly from that of the single-wall model.

3.4 NLOS Effects Due to Scattering

3.4.1 The Scattering Object Model

The geometry used in the simulation of NLOS effects due to a scattering object in the environment is shown in Fig. 3.17. The geometry parameters are as follows:

- The scattering object is a PEC box, with a size of 0.2 m×0.2 m×0.2 m, centered at (-0.1,0.2) m. The simulation area is a 2 m×2 m×1 m air box.

- The target position is (0, 0) m, and the receivers (sensors) are at (-0.4, -0.5) m, (-0.3, 0.5) m, (0.5,-0.1) m, respectively. Sensor 2 is located behind the scattering object.
- The target is a vertical electric dipole, located on the ground, with a length of one FDTD cell size (0.01 m). The receivers are simulated as point sensors.
- The source is an ideal current source (infinite internal impedance), and the signal form is a 300MHz sinusoidal wave, modulated with a Gaussian envelope having a time constant of 0.04 μs.

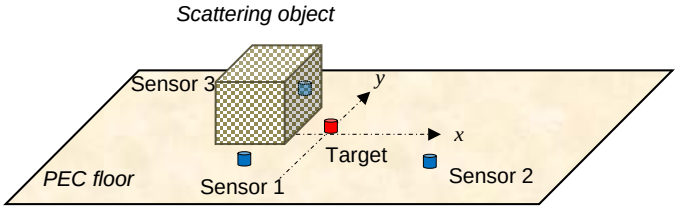

Figure 3.17. 3D view of the scattering object model.

3.4.2 XFDTD Simulation

Because the scattering problem does not have an analytic solution when the object's geometry is arbitrary, the transfer function is derived using XFDTD (see Fig. 3.18) using the finite-difference time-domain method.

The air box is surrounded with a PML boundary condition, except for the bottom PEC sheet. The basic cell size is 0.01 m, with a maximum ratio of 0.1. The cells are forced to pass the sensors and source as well as the object's edges. The resulting time step is 1.9253×10^{-11} *s*; thus the estimated localization error is around 0.0058 m.

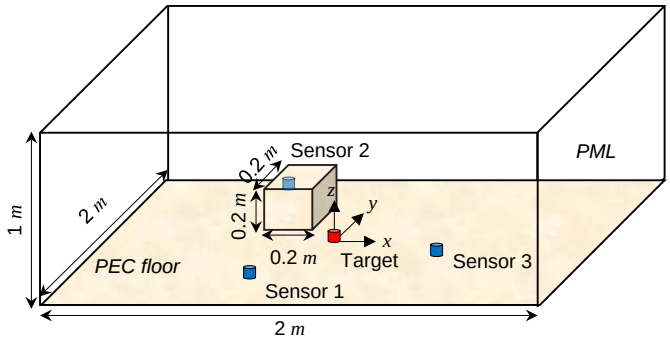

Figure 3.18. Localization simulation setup geometry inside XFDTD.

Since the signal bandwidth is mainly between 250 MHz and 350 MHz, the transfer function $T(\omega) = E_z(\omega)/I(\omega)$ need only be determined within this range. Table 3.5 shows the localization error when using the iterative method at each step in the iteration.

Table 3.5. Localization errors at different iterations.

Iteration NO.	x (m)	y (m)	Error (m)
0	0.0169	-0.2781	0.2786
1	0.0311	-0.1489	0.1521
2	0.0245	-0.0868	0.0902
3	0.0156	-0.0537	0.0560
4	0.0104	-0.0367	0.0382
5	0.0101	-0.0260	0.0279
6	0.0057	-0.0174	0.0183
7	0.0044	-0.0138	0.0145
8	0.0031	-0.0102	0.0106
9	0.0017	-0.0065	0.0068
10	0.0017	-0.0065	0.0068

The initial localization result is found by using the usual TDOA method, and the iterative method is applied until the iteration converges. Figure 3.19 shows the trajectory of estimated target positions as the iterations proceed. The red star shows the true target position.

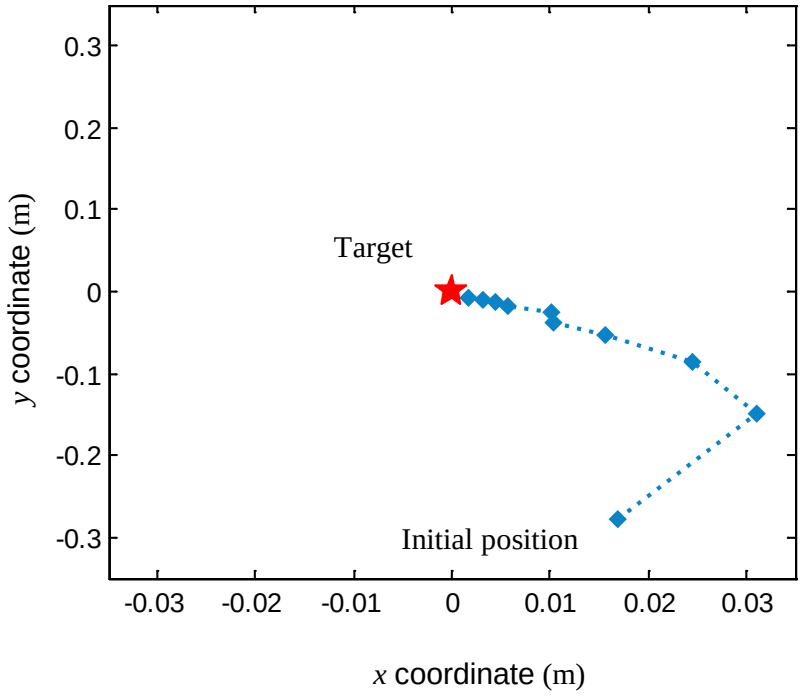

Figure 3.19. Iteration process for scattering object model simulation.

3.5 Conclusion

In this chapter, we have introduced an iterative method that accounts for the presence of a building enclosure (or any other NLOS effects) in the TDOA source localization algorithm. The method uses a derived transfer function for the propagation between the target and receivers, as a function of the target and receiver locations, to "de-embed" the NLOS effects and calibrate the channel back to LOS (free-space) propagation. This method employs an iterative algorithm, iteratively updating the transfer

function between successive minimizations of the objective function, as the estimated target location changes in the search process.

A global search method is also employed; however, due to computation time, the iterative method is the best choice unless the convergence process is not successful (such as in the case when multiple reflections exist and the signal is operated at a high frequency band). The global search method will be presented in detail in Chapter 4.

Our proposed iterative method is quite effective at accounting for NLOS effects, and this is verified by the results we presented assuming a single-wall model, a near-field model and a scattering object model.

In the absence of noise, the proposed iterative method converges to the true target location for the different single-wall models, with an error that is only limited by the sampling frequency that is used in the cross-correlation to find the TDOA values. To improve numerical efficiency, the frequency used in the cross-correlation can be much higher than that used in the original ADC sampling of the signals at the receivers, with interpolation on the ADC data used to increase the number of sample points used for the cross-correlation.

The localization results are not only dependent on the layout of the sensors (GDOP), but also depend significantly on the parameters of the wall, being strongly affected by the permittivity of the wall for an assumed wall thickness.

Our results have shown that neglecting the effects of the wall (i.e., using the usual direct TDOA method) typically results in a localization error on the order of 0.2 meters, for the wall considered here. This error is removed when using the proposed iterative algorithm, in the absence of noise. However, our results have also shown that the

proposed iterative method is more sensitive to noise than the usual direct TDOA method. To overcome this phenomenon, a modified transfer function is introduced, which includes an ω term in the transfer function. This makes the transfer function that is used in the iterative method consistent with the usual direct TDOA method. The iterative method with the modified transfer function performs better that that with the original transfer function for low-noise environments, in which SNR is greater than about 10 dB. Using the modified transfer function, the iterative method always outperforms the usual direct TDOA method that neglects the presence of the wall.

The near-field model also shows that, as long as the transfer function is accurately derived, the iterative method can improve localization accuracy to the order of several millimeters in the absence of noise, which is in consistent with the sampling frequency's prediction.

The scattering object model is simulated inside the XFDTD to verify the practicality of obtaining a transfer function from simulation software. Results show that the convergence process is smooth and successful.

Chapter 4

TDOA Localization with Multiple Reflections

Chapter 4 applies the proposed method involving a de-embedding of the transfer function to cases where multiple reflection effects exist. Three models are provided to represent different cases of multiple reflection scenarios. Section 4.1 investigates the parallel-wall model, where the target is located in between two parallel walls, and the sensors are located on the same side of the structure, far away from the target. The parameters of the walls are assumed to be known, so that the transfer function can be approximately derived using reciprocity algorithm and plane-wave theory. Section 4.1 considers the case when the reflections are basically coming from a single direction (the *x* direction). Sections 4.2 and 4.3 propose a 3D localization model and a 2D enclosed-wall model, which illustrate cases in which the reflections come from either *z* or both the *x* and *y* directions. A hybrid iterative method is proposed to solve the problem of convergence difficulties in the iterative method when the transmitted signal has a high carrier frequency so that the enclosure has a size that is significant compared with a wavelength, a problem that is worsened when the bandwidth of the transmitting signal is low.

4.1 The Parallel -Wall Model

4.1.1 Derivation of Transfer Function

Figure 4.1 presents the geometry of the parallel-wall model. In this model, the receivers (sensors) are once again assumed to be put far away from the dipole source so that plane wave theory can be utilized to obtain the transfer function analytically. Since the back wall behaves like a reflecting surface, the parallel-wall model is a canonical

situation where multiple reflections exist, so that the target is essentially inside of a cavity-like region.

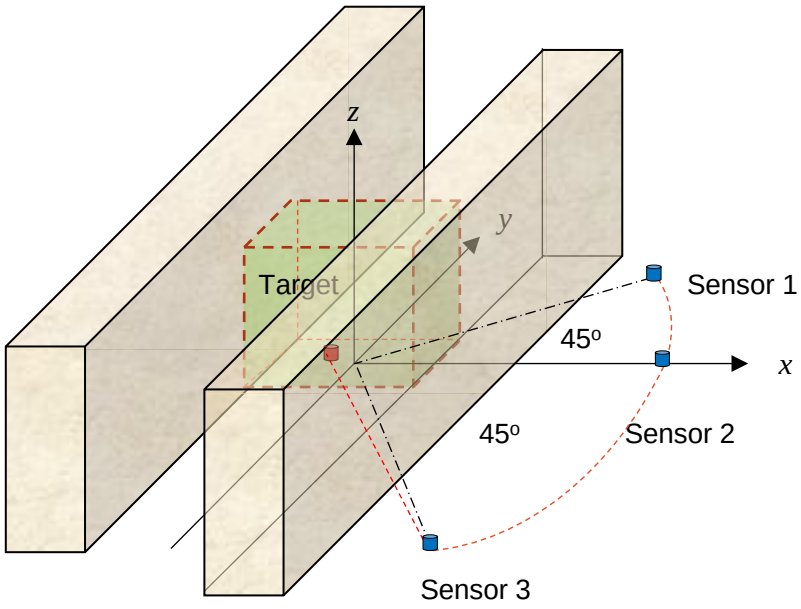

Figure 4.1. 3D view of the parallel wall model.

The assumptions used in the simulation are as follows:

- The geometry consists of a square domain (simulating a square building footprint) that is 30 by 30 meters, centered at the origin.
- A single vertical electric dipole is used as the source.
- The receivers are located at a distance of 1 km from the origin.
- The receivers and target are all on a PEC ground for simplicity.
- The wall is infinite along the *y* direction, and has a 20 cm thickness. Wall parameters: $\sigma = 0$ s/m, $\varepsilon_r = 6.3 - j0.69$. The wall has an infinite length and height along the *y* and positive *z* directions.
- The TDOA for a pair of receivers is estimated using a cross-correlation between the signals (or processed signals) obtained from each pair of receivers.

Three different signal forms for the transmitted signal are assumed; the basic signal form is a Gaussian envelope, modulated with a sinusoidal wave as follows:

- Case 1: carrier frequency 3 MHz, baseband frequency 1 MHz;
- Case 2: carrier frequency 300 MHz, baseband frequency 1 MHz;
- Case 3: carrier frequency 3 GHz, baseband frequency 1 GHz (an ultra-wide band signal);

Figure 4.2 shows the parameters needed to obtain the transfer function after applying the reciprocity algorithm. In the far field, from plane wave theory, the incident angles are approximately equal on either side of the front wall. Waves entering the target position contain the direct incident field and waves bouncing between the front and back walls. Figure 4.2 only shows the direct incident field. There only exists E_θ, and thus only TE_x wave needs to be taken into consideration.

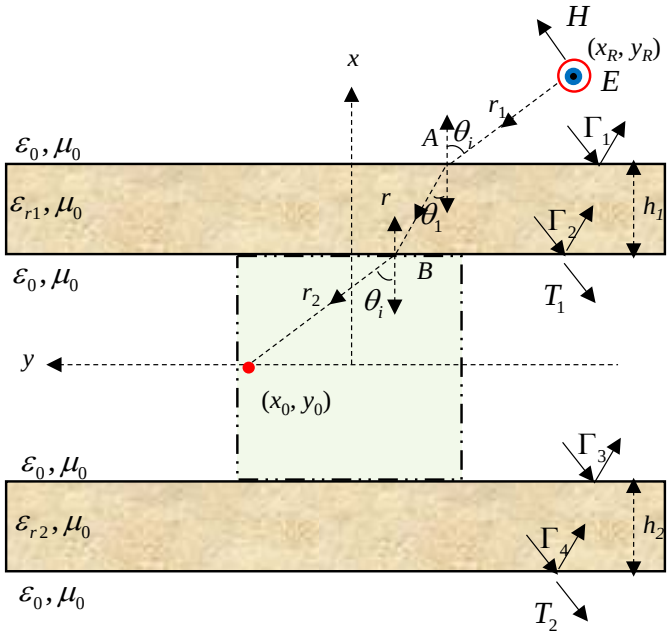

Figure 4.2. Top view of the parallel wall model.

By using the transverse equivalent network (TEN) method, the transfer function is derived as

$$\begin{aligned} T &= 2\left(1+\Gamma\right)V_2' E_A e^{-j\left(k_y\left(y_A-y_0\right)\right)} \\ &= 2\left(1+\Gamma\right)V_2' E_A e^{-j\left(k_0 \sin\left(\theta_i\right)\tan\left(\theta_i\right)\left(h_1+L/2-x_0\right)\right)}, \end{aligned} \tag{4.1}$$

where Γ is the reflection coefficient at incident point *A*, calculated from TEN. The angle θ_i is the incident angle, and is approximated as

$$\theta_i \approx \arctan\left(\frac{y_R - y_0}{x_R - x_0}\right). \tag{4.2}$$

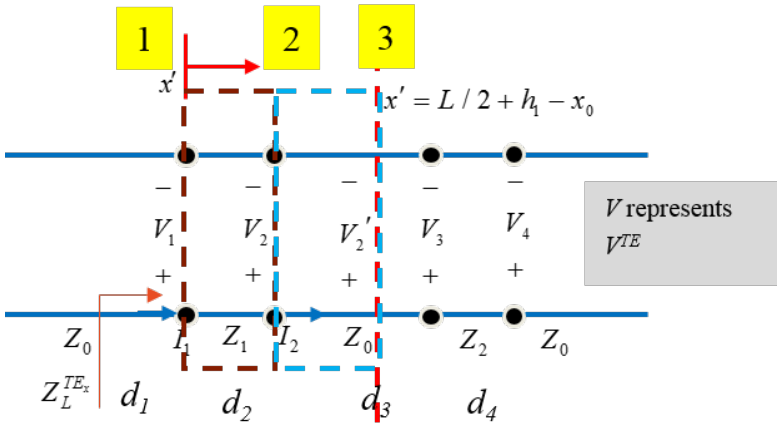

Figure 4.3. Transverse equivalent network for the parallel-wall model.

V_2' is the corresponding voltage at the target position when the incident voltage at position *A* is 1*V*, as shown in Fig. 4.3. Using the ABCD matrix, V_2' is derived as

$$\begin{bmatrix} V_2' \\ I_2' \end{bmatrix} = \begin{bmatrix} A_2 & B_2 \\ C_2 & D_2 \end{bmatrix}^{-1} \begin{bmatrix} A_1 & B_1 \\ C_1 & D_1 \end{bmatrix}^{-1} \begin{bmatrix} V_1 \\ I_1 \end{bmatrix}, \tag{4.3}$$

where

$$A_1 = \cosh\left(jk_{x1}h_1\right), B_1 = Z_1 \sinh\left(jk_{x1}h_1\right),$$
$$C_1 = \frac{\sinh\left(jk_{x1}h_1\right)}{Z_1}, D_1 = \cosh\left(jk_{x1}h_1\right) \quad , \tag{4.4}$$

and

$$A_2 = \cosh\left(jk_{x0}\left(L/2 - x_0\right)\right), B_2 = Z_0 \sinh\left(jk_{x0}\left(L/2 - x_0\right)\right),$$
$$C_2 = \frac{\sinh\left(jk_{x0}\left(L/2 - x_0\right)\right)}{Z_0}, D_2 = \cosh\left(jk_{x0}\left(L/2 - x_0\right)\right). \tag{4.5}$$

E_A is the incident electric field at position A from the receiver in the far field acting as a transmitter in reciprocity. The term k_0 is the wavenumber in air and L is the distance between the walls. The location (x_0, y_0) is the target position, and (x_R, y_R) is the receiver position.

4.1.2 Sanity Check under Three Different Signal Forms

Similar to the checks presented in Section 3.2, comparisons are made here between localization errors using the usual direct TDOA method (using the original received signals, with no transfer function accounted for) and using the iterative method (using the processed signals, with the transfer function accounted for). All of the simulations are implemented using an ADC sampling frequency of 100 GHz, under noise-free conditions. Of course, this high sampling frequency can be replaced by using a lower sampling frequency and an interpolation method, as was mentioned in Chapter 3. The spatial sample points are on a 16×16 grid inside the 30 × 30 meter enclosure.

A) Signal Case 1

Figure 4.4 shows the localization error comparison (in meters) between different methods for the parallel-wall model using signal case 1. The left side of the figure shows

the error when using the usual direct TDOA method, while the right side of the figure shows the error when using the proposed iterative algorithm. As shown in Fig. 4.4, when carrier frequency is 3 MHz and baseband frequency is 1 MHz, the error range is reduced from an averaged value of 1.23 m to 0.0019 m when compared with the usual direct TDOA method. This clearly shows that de-embedding the transfer function in the TDOA method can work well to improve localization accuracy under the condition that multiple reflections exist.

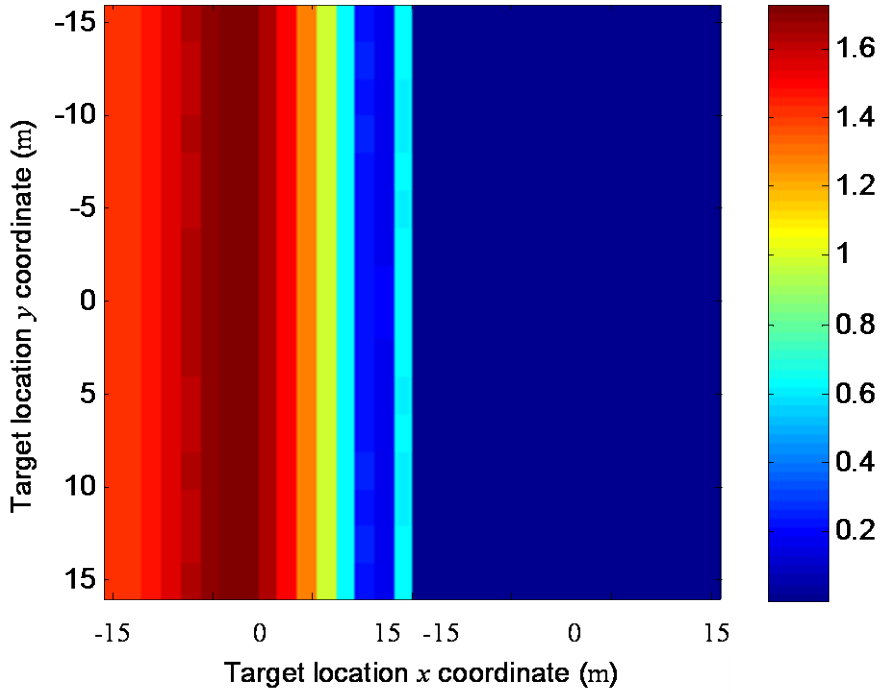

Figure 4.4. Localization error comparison (in meters) between different methods for the parallel-wall model using signal Case 1.

B) Signal Case 2

Figure 4.5 shows the localization error comparison (in meters) between different methods for the parallel-wall model using signal case 2. The left side of the figure shows the error when using the usual direct TDOA method, while the right side of the figure

shows the error when using the proposed iterative algorithm. As shown in Fig. 4.5, when the carrier frequency (300 MHz) is much larger than the baseband frequency (1 MHz), the iterative method has a convergence problem: the iteration process has not converged within the entire space domain. (The right half of Fig. 4.5 shows the last iteration results when the estimated target position is forced to be inside the 30 × 30 meter area; otherwise, the estimated error will become extremely large). Detailed explanations for this convergence problem are given in Section 4.1.3.

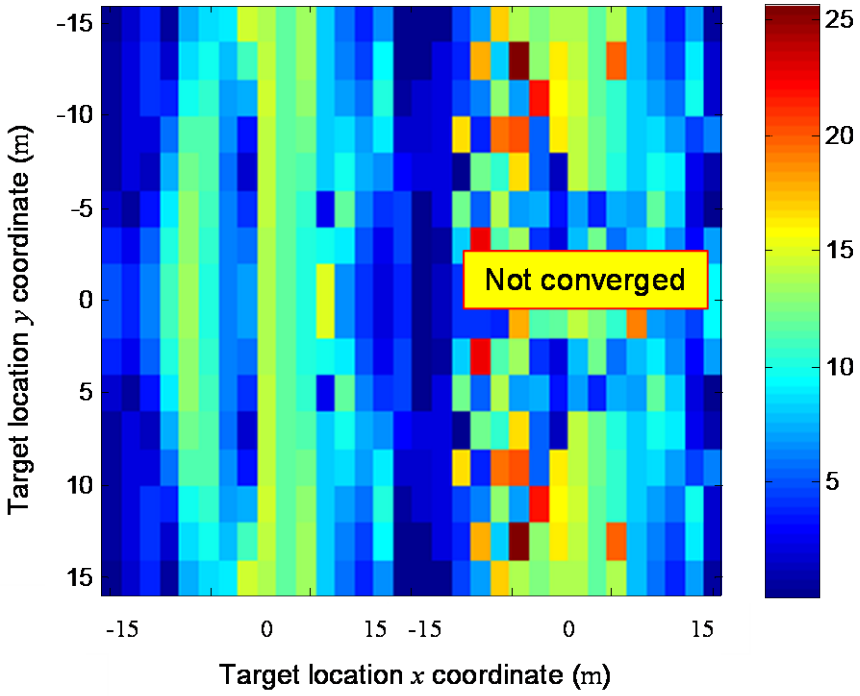

Figure 4.5. Localization error comparison (in meters) between different methods for the parallel-wall model using signal case 2.

C) Signal Case 3

Figure 4.6 shows the localization error comparison (in meters) between different methods for the parallel-wall model using signal case 3. The left side of the figure shows the error when using the usual direct TDOA method, while the right side of the figure

shows the error when using the proposed iterative algorithm. This result shows the localization results from an ultra-wideband signal. Although the averaged error is reduced from 0.1315 meters to 0.0022 meters, the iterative method still has a convergence problem in some particular positions, especially when the target is getting close to the back wall, as seen in the figure (the leftmost column of the right half of the figure). Unlike in signal case 2, the convergence problem here can be solved by rearranging the sensor geometry. However, to find a perfect geometry is complicated, so in Section 4.1.4, the time-gating concept is introduced to help overcome this convergence problem.

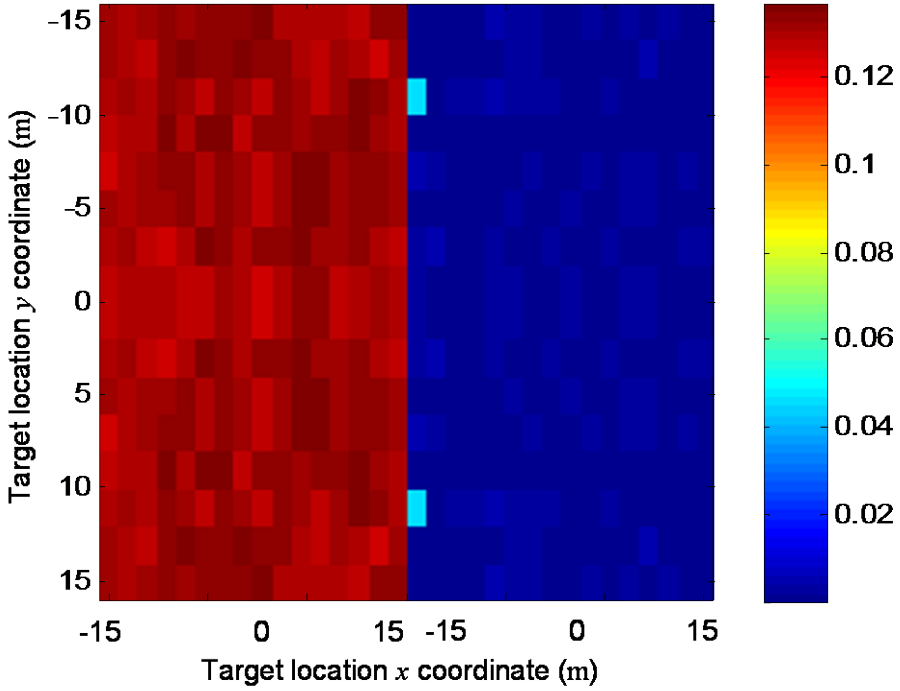

Figure 4.6. Localization error comparison (in meters) between different methods for the parallel-wall model using signal case 3.

4.1.3 Convergence Problem

When the back wall exists, the lower the carrier frequency is, the more likely it is for the iterations to converge (signal case 1), because the phase of the transfer function is

more regular and well-behaved (smoother) over the region between the walls. However, when the carrier frequency is relatively high, such as 300 MHz and 3 GHz, the transfer function exhibits more of a standing-wave effect due to the waves bouncing between the walls. This is the underlying cause of the convergence difficulty, since it creates an objective function that is not smoothly varying with a single well-defined global minimum. This problem is magnified when the baseband frequency is low; this is the reason that signal case 2 cannot converge, while signal case 3 converges as long as a suitable geometrical arrangement of the sensors is found, based on the transfer function.

It is illustrating to examine the behavior of the objective function. Plots of the objective function for the single-wall and parallel-wall cases are compared here. The target position is assumed to be located at (-1, -1) meters, and the enclosed area size is reduced to 10 ×10 meters for numerical efficiency considerations. There are 100 × 100 grid points inside. (This corresponds to a step size of 0.1 meters, starting from (-4.95, -4.95) meters, which means the sampled grid points do not include the exact target position). The permittivity and conductivity of the walls are the same as in the single-wall model (ε_r = 6.3 - j0.69). All of the sensors geometry and the sampling frequency are the same as those used in the single-wall model. The goal here is to explain the convergence problem, so signal case 2 is chosen. (The signal form is a Gaussian envelope with a 1 MHz baseband frequency, modulated by a sinusoidal wave with a 300 MHz carrier frequency.)

Figure 4.7 shows a plot of the objective function after de-embedding the corresponding transfer function at every position for the single-wall model. This objective function is what is minimized in the global search method to find the target

position. As expected, the objective function in the front-wall case is smooth and the estimated target position from the global search method is (-0.95, -0.95) meters.

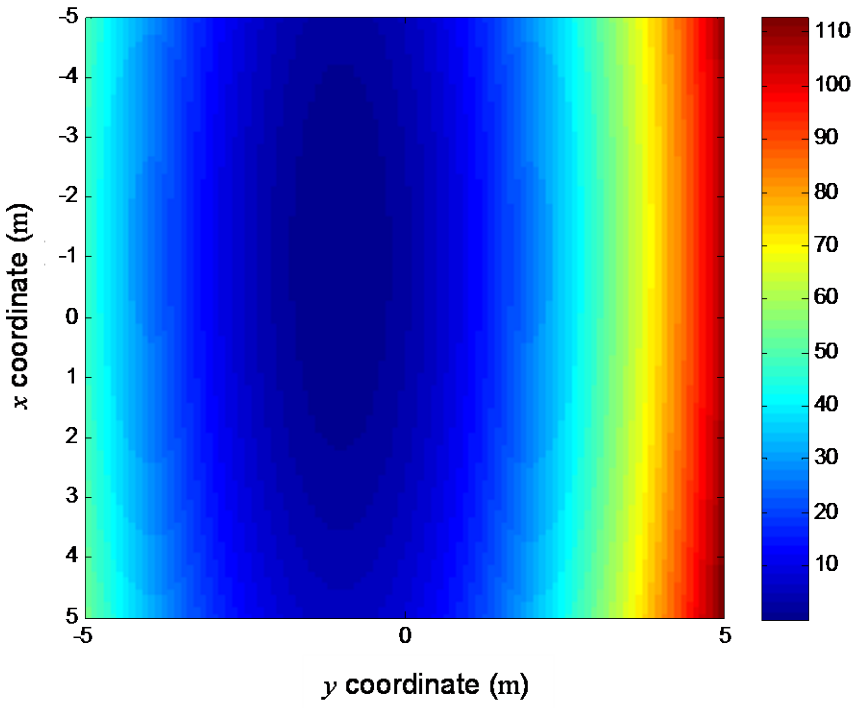

Figure 4.7. Objective function plot for the single-wall case.

Figure 4.8 shows the objective function plot after de-embedding the corresponding transfer function at every position for the parallel-wall case. Obviously, we can see there exists a strong standing wave along the *x* direction. In this case, the estimated target position from the global search method is at (0.85, -1.05) meters, and the error is about 1.85 meters. The reason for such a large error (larger than the step size of 0.1 meters) is that along the *x* coordinate the standing wave makes the objective function change so rapidly that a lot of local minima exist nearby the target position. Therefore, using the global search method with a finer step size is required to find the global minimum accurately.

For both the front-wall case and the parallel-wall case, as long as the sampling resolution is small enough, the estimated target position will be accurate and on the order of step size when using the global search method.

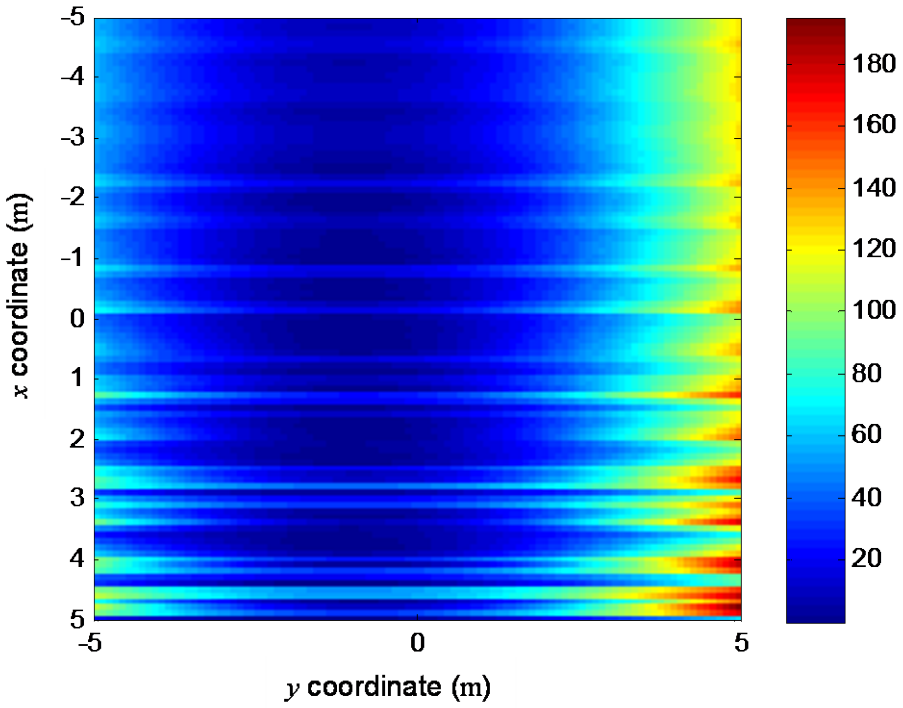

Figure 4.8. Objective function plot for the parallel-wall case.

Figure 4.9 shows the objective function plot along the *x* coordinate when the *y* coordinate is accurate (corresponding to the true target location) under different cases. Figures 4.9 (a), (b), and (c) illustrate the parallel-wall model, and Figs. 4.9 (d), (e), and (f) illustrate the single-wall model. Obviously, in the parallel-wall cases, when the carrier frequency of the received signal is small, as shown in Fig. 4.9 (a), the objective function is smooth, and it is easy to find the global minimum. However, when the carrier frequency band is relatively high, while the bandwidth is narrow, as shown in Fig. 4.9 (b), the iterative method will likely step into local minima. Figure 4.9 clearly explains the

reason for the convergence problem in signal cases 2 and 3. The smallest resolution needed for the global search method in this parallel-wall case is about 0.01 meters. The overall shape of the objective function in Fig 4.9 (b) indicates that a standing waves exists between the walls, though a rapidly-varying noise-like oscillation is also very pronounced.

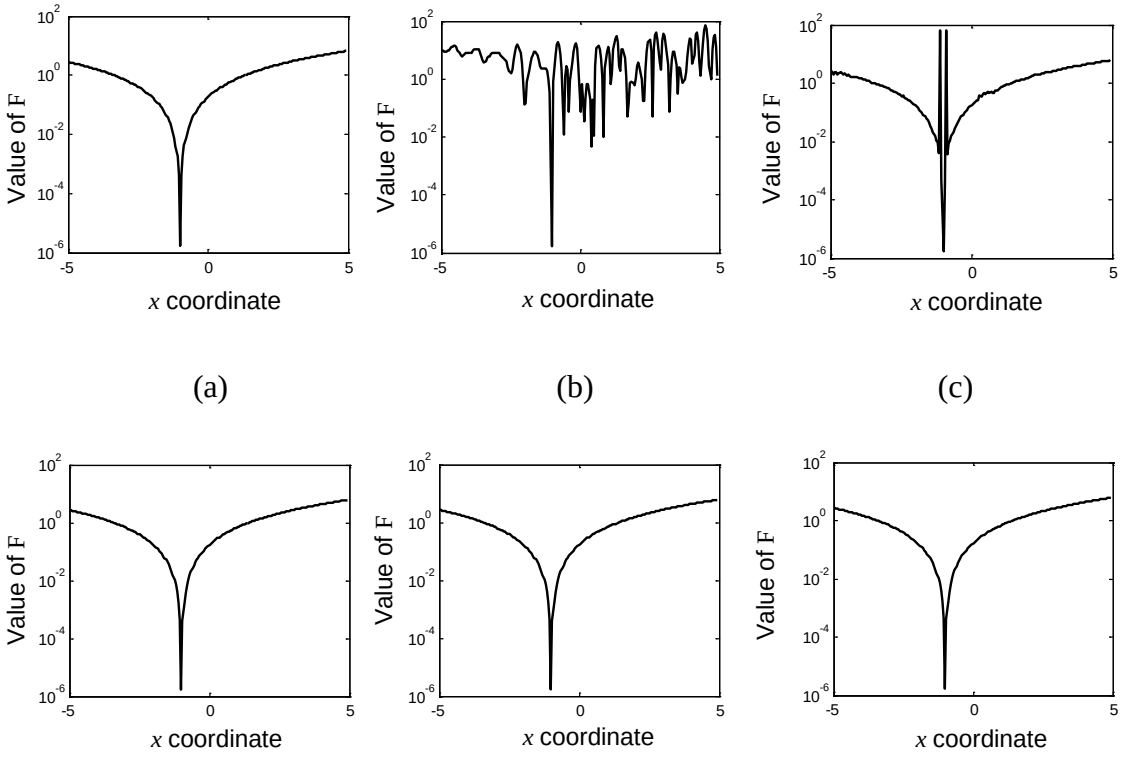

Figure 4.9. Objective function along the *x* coordinate when the *y* coordinate is accurate. (a) Parallel-wall, case 1; (b) Parallel-wall, case 2; (c) Parallel-wall, case 3; (d) Single-wall, case 1; (e) Single-wall, case 2; (f) Single-wall, case 3.

From transmission line theory, we know that a standing wave repeats in magnitude every half wavelength. However, when viewed as a standing wave, more fluctuations seem to exist than there are supposed to be there (the noise-like oscillation). This is because the processed signal will have distortions when the de-embedded transfer

function is not calculated at the true target location; thus, the cross-correlation would never be exact, and the TDOAs will have errors. To explain it even more simply, if we calculate the TDOA for two identically-shaped and time-shifted signals, the cross-correlation is straightforward and accurate; however, when calculating the TDOA from two distorted signals, the answer will sometimes be affected. The cross-correlation algorithm is not to blame; the accuracy of the TDOA depends upon how seriously the signals are distorted.

4.1.4 Hybrid Iterative Method

Although the global search method is accurate as long as the resolution of the search mesh is small enough to capture the behavior of the transfer function inside the area of interest, it is very time-consuming. So here we introduce a hybrid iterative method that partially retains the efficiency of the iterative method while also partially retaining the robustness of the global search method. Because standing waves mainly exist in the *x* direction in the parallel-wall case, the area of interest need only be meshed and searched globally along the *x* coordinate, while the iterative method is only used to determine the *y* coordinate. A flow chart depicting this scheme is shown in Fig. 4.10.

The key point for the hybrid iterative method is the updating of the Time Difference of Arrival (TDOA) between each pair of sensors at each iteration (as in the previous iterative method) until the estimated *y* coordinate in the search converges. For each specific *x* coordinate, there will always be a corresponding *y* coordinate that makes the objective function minimum, and this is found using the Levenberg-Marquardt algorithm, but with a one-dimensional search in the *y* coordinate. The rest of the hybrid iterative method is exactly the same as the originally proposed iterative method.

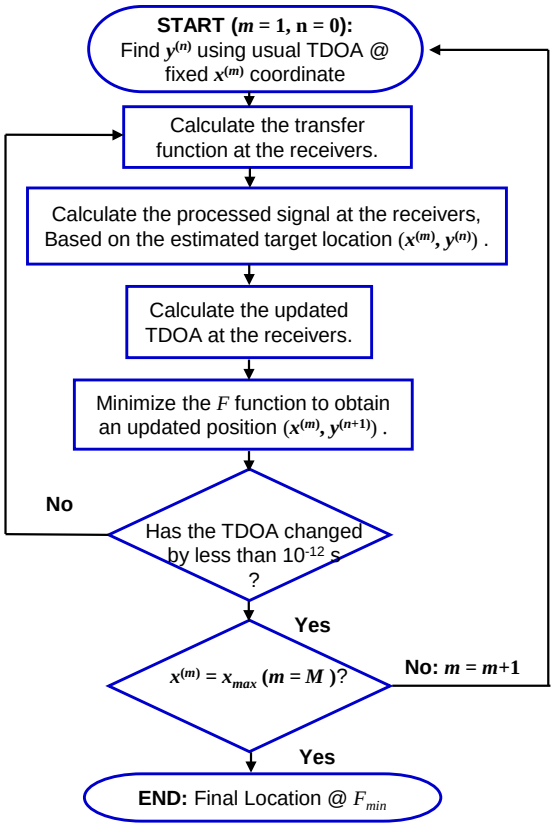

Figure 4.10. Flow chart for hybrid iterative method.

Figure 4.11 shows the objective function plot along the x coordinate in the parallel-wall case. The step size of the x coordinate is 0.1 meters, passing through the true target position. The final error is 0.05 meters, which is reasonable, because the mesh resolution is 0.1 meters. The hybrid iterative method is much more efficient than the global search method, because instead of meshing the search region in both the x and y directions, the y coordinate is found using the iterative method. The smallest step size needed for the hybrid iterative method to find a good approximation for the target position is much larger than that for the global search method (0.1 meters for the hybrid iterative method vs. 0.01 meters for the global search method); this is because the y

coordinate in the hybrid iterative method is found by the Levenberg-Marquardt algorithm; thus this parameter can be almost error-free.

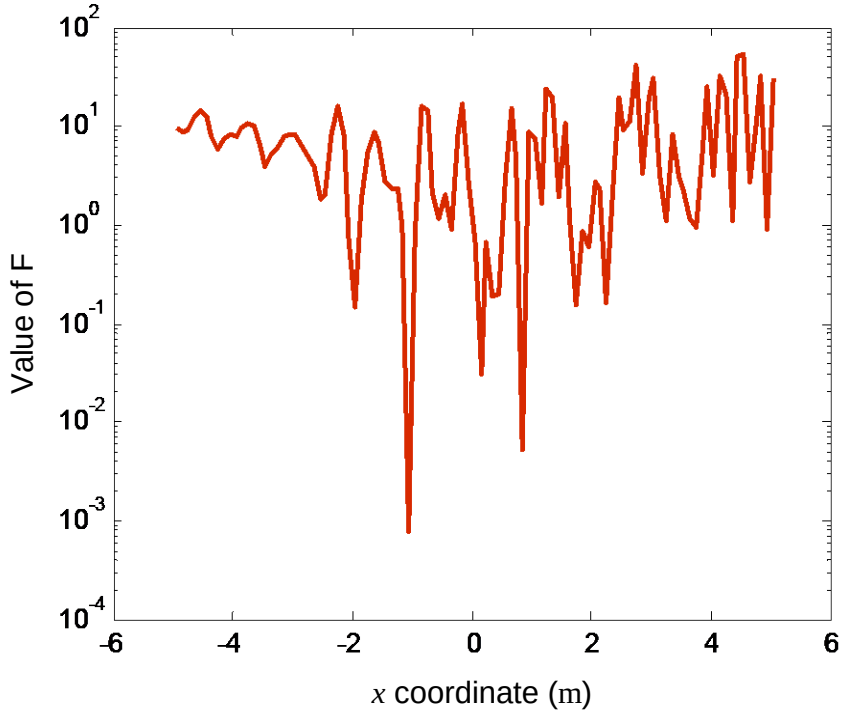

Figure 4.11. Plot of the objective function along *x* using the hybrid iterative method.

An ultra-wideband signal (signal case 3) is typically used for indoor localization. Because of its wideband property in the frequency domain, it occupies an extremely narrow band in the time domain, so that when reflections exist, the direct wave and reflected wave can sometimes be differentiated from each other using a time-gating method. As long as the effect from the back wall is removed (as in Fig 4.12), the transfer function for the iterative algorithm becomes the same as in the single-wall case. Details are discussed below in Section 4.1.5.

4.1.5 Time Gating Method

Figure 4.12 illustrate how time gating can be used to remove the reflected part of the signal from the total signal after the signal is reflected from the back wall. If the reflected part of the signal can be effectively removed by time gating, i.e., chopping off the reflected part of the signal, then the effect of the back wall is removed, and the iterative method can be based on the transfer function for the front wall only, which is advantageous since this removes the standing-wave problem that was responsible for the convergence difficulty in the parallel-wall case.

Figure 4.13 shows the localization results for signal case 3 after applying the time-gating method combined with the iterative method (using the single-wall transfer function). The average error is reduced from 0.1315 meters to 0.0018 meters. When the target is close to the back wall, the time-gating method becomes more accurate than the iterative method (which uses the parallel-wall transfer function).

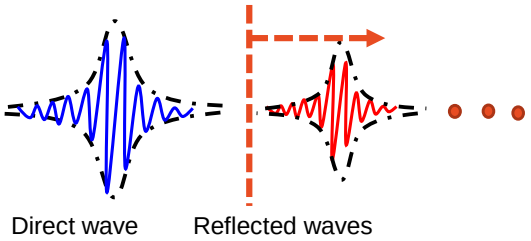

Figure 4.12. Illustration of chopping off the reflected wave in the time-gating method when the direct wave is separate from the reflected wave.

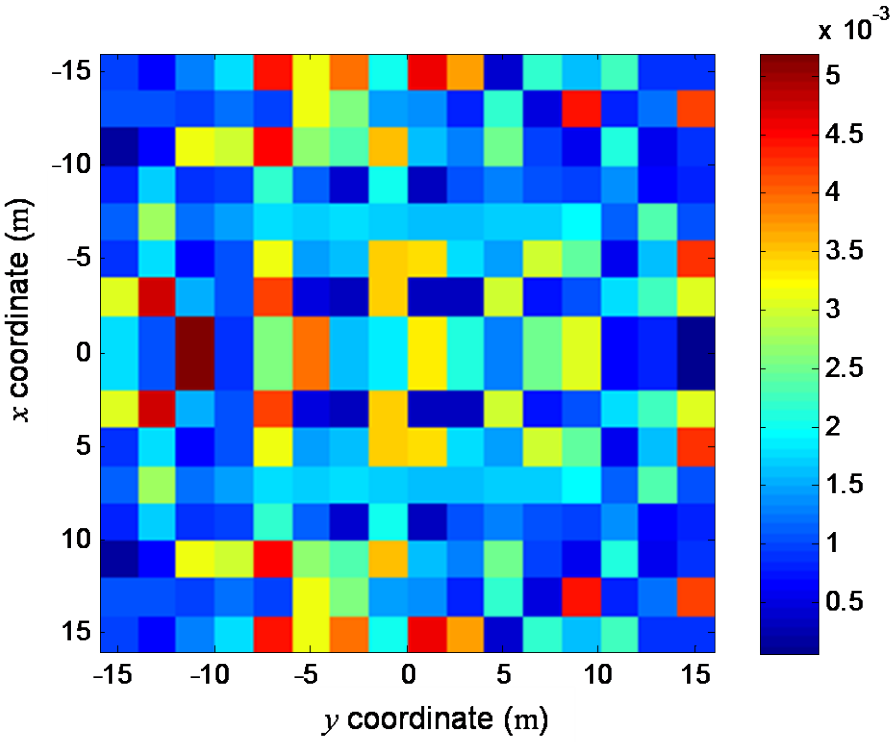

Figure 4.13. Localization error (in meters) after time gating for parallel wall model Case 3.

Nevertheless, the time-gating method does not always work. When the target is extremely close to the back wall, and the direct wave and reflected wave are merged together (see Fig. 4.14), there will be difficulty; whether or not this time-gating method still works depends on how much the signals have merged together.

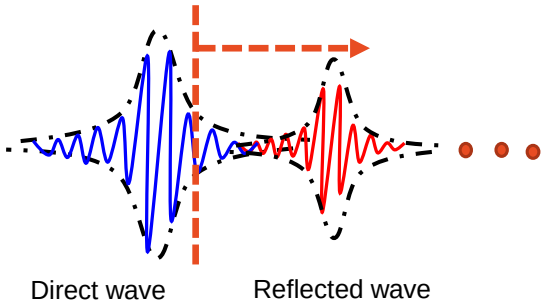

Figure 4.14. Illustration of chopping off the reflected wave in the time-gating method when the direct wave is partially merged with the reflected wave.

Figure 4.15 shows a comparison of results when the target is extremely close to the back wall (less or equal to 2 meters). The left side of the figure shows the error when using the original iterative method, while the right side of the figure shows the error when using the proposed time-gating iterative algorithm (using the single-wall transfer function combined with time gating). The positions inside the red curves are those for which the time-gating method using the front-wall transfer function gives a more accurate localization than the iterative method that uses the parallel-wall transfer function, for the same sensor geometry.

Assume the time delay between the direct and the reflected wave is Δt, and $\tau = 1/f_{base}$ is the time constant of the baseband signal (the modulating envelope). From the obtained simulation experience, it is concluded that when $\Delta t/\tau \geq 1.56$, the time-gating method will work. The chop-off position is placed at the -3 dB envelope position of the Gaussian waves if the waves are merged together. Figure 4.16 shows a simplified model used for the minimum distance calculation in the time-gating method.

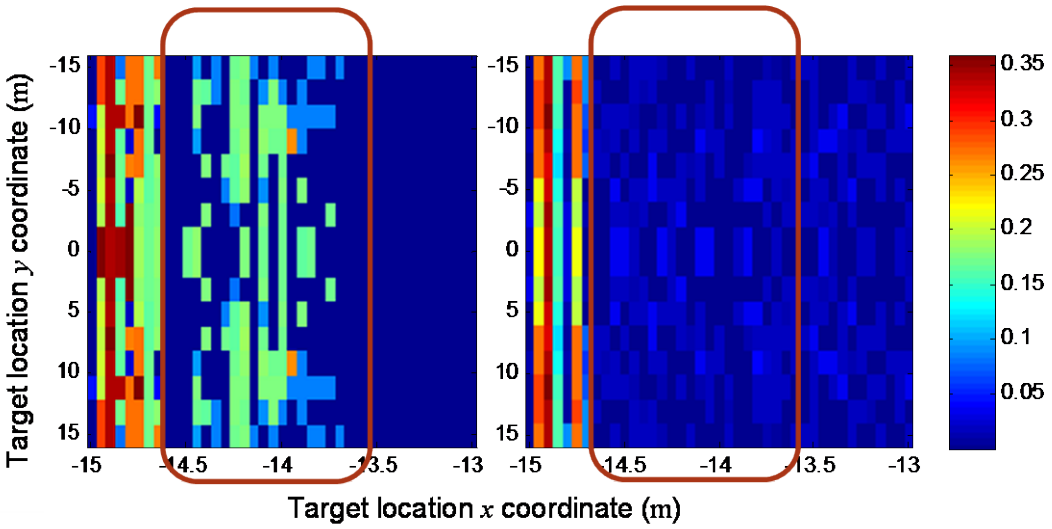

Figure 4.15. Localization error (in meters) comparison between different methods for the parallel-wall model using signal case 3. The results are shown for a region close to the back wall.

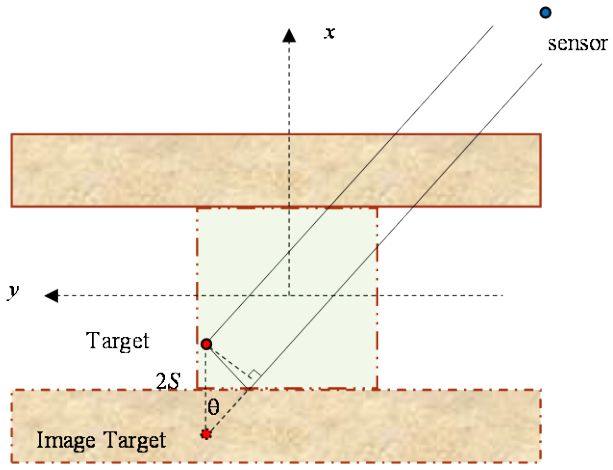

Figure 4.16. A simplified model used for the minimum distance calculation in the time-gating method.

Based on this model, the minimum distance from the back wall to the target necessary in order to successfully use the time-gating method is

$$S \geq \frac{0.78c}{\cos(\theta) f_{base}}, \tag{4.6}$$

where θ is the incident angle of the direct wave. Equation (4.6) holds only when the sensors are put in the far field, so that the angle of incidence on the back wall is essentially the same as on the front wall (i.e., plane-wave incidence).

When the target position does not meet this minimum equation, rearranging the sensor geometry may be the only way to achieve convergence. Equation (4.6) demonstrates that the distance from the back wall is related to the baseband frequency. When the carrier frequency is 3 GHz and the baseband frequency is 100 MHz, it is found from simulation results that the minimum distance is about 3.3 meters, which is consistent with Eq. (4.6). When the carrier frequency is 300 MHz and the baseband frequency is 100 MHz, the minimum distance is also about 3.3 meters.

4.2 The 3D Localization Model

The geometry of the 3D localization model is shown in Fig. 4.17. The simulation background is as follows:

- The four receivers are put 1 km away from the origin, and each one has a -90°, 0°, 90°, 180° angle with the *x* axis, respectively. Sensor 1 is on the ground, while the others are located off of the ground at various heights, as shown in Fig. 4.17.
- The sampling frequency is 100 GHz (again, the sampling frequency can be reduced using interpolation, as in Chapter 3).
- The target is a vertical electric dipole, located 20 meters above the ground.
- The basic signal form is a Gaussian envelope with a bandwidth frequency of 1 MHz, which modulates a 3 MHz sinusoidal carrier wave.

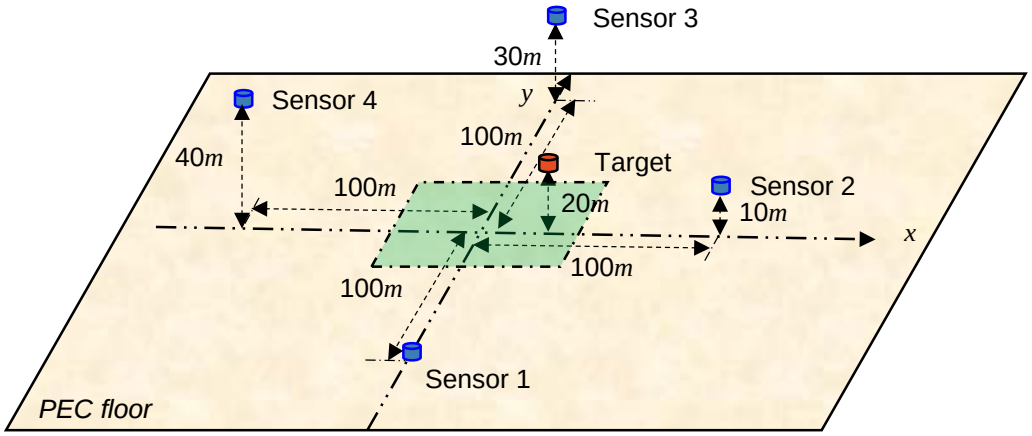

Figure 4.17. 3D localization model.

4.2.1 Derivation of Transfer Function

From TDOA localization theory, three receivers can only localize a 2D target. Thus, for three-dimensional localization, at least four receivers are required. The transfer function is derived from image theory, and Fig. 4.18 shows the parameters used for the geometry (taking sensor 3 as an example).

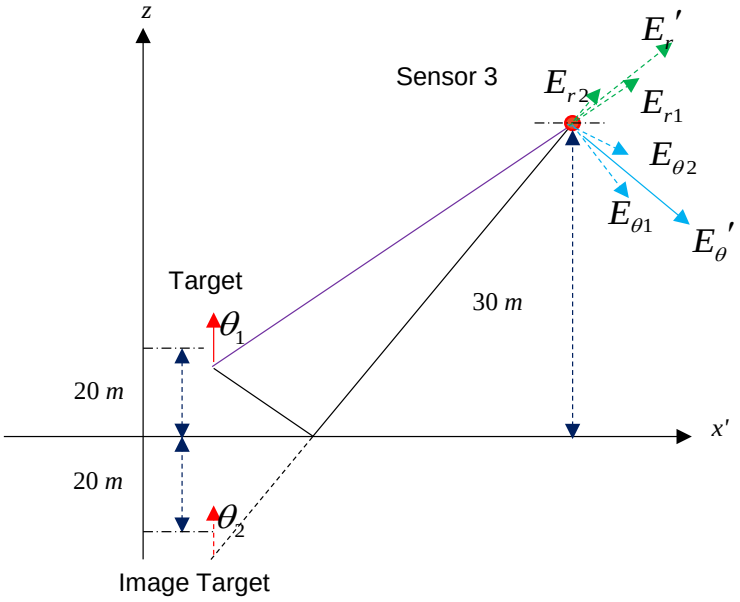

Figure 4.18. Side view of the 3D localization model for sensor 3.

For simplicity, the target is assumed to be a vertical electric dipole, and Fig. 4.18 shows image theory applied between sensor 3 and the target. The incidence angles from the target and the image target are θ_1 and θ_2, respectively, and are represented as:

$$\theta_1 = \arccos\left(\frac{z_R - z_0}{\sqrt{(x_0 - x_R)^2 + (y_0 - y_R)^2 + (z_0 - z_R)^2}}\right),$$
$$\theta_2 = \arccos\left(\frac{z_0 + z_R}{\sqrt{(x_0 - x_R)^2 + (y_0 - y_R)^2 + (z_0 + z_R)^2}}\right). \tag{4.7}$$

The target is at (x_0, y_0, z_0), and the receiver is at (x_R, y_R, z_R). Adding the field components E_θ' and E_r' in the rectangular coordinate system yields the total electric field at sensor 3. Suppressing the dipole moment, the final transfer function (E_z) is then:

$$\underline{T} = -\hat{z}(E_{\theta 1}\sin(\theta_1) + E_{\theta 2}\sin(\theta_2) - E_{r1}\cos(\theta_1) - E_{r2}\cos(\theta_2)), \tag{4.8}$$

and the general formula for E_θ and E_r is:

$$E_\theta = \frac{j\omega\mu Il}{4\pi} e^{-jkr}\frac{1}{r}\left[1 + \frac{1}{jkr} + \frac{1}{(jkr)^2}\right]\sin\theta,$$
$$E_r = \frac{\eta Il}{2\pi} e^{-jkr}\left(\frac{1}{r^2}\right)\left[1 + \frac{1}{jkr}\right]\cos\theta. \tag{4.9}$$

4.2.2 Simulation Results

The spatial sample points are on a 16×16 grid inside the 30 ×30 meter enclosure, centered at origin. In this model the z parameter (height of the target) is unknown and is to be determined.

As shown in Fig. 4.19, the left side of the figure shows the error when using the usual direct TDOA method, while the right side of the figure shows the error when using the proposed iterative algorithm. Error range is reduced from the range 5.35 ~ 17.76

meters to the range 0.0001 ~ 0.058 meters when comparing the usual direct TDOA method, in the lefthand side of the figure, to the proposed iterative method, in the righthand side of the figure.

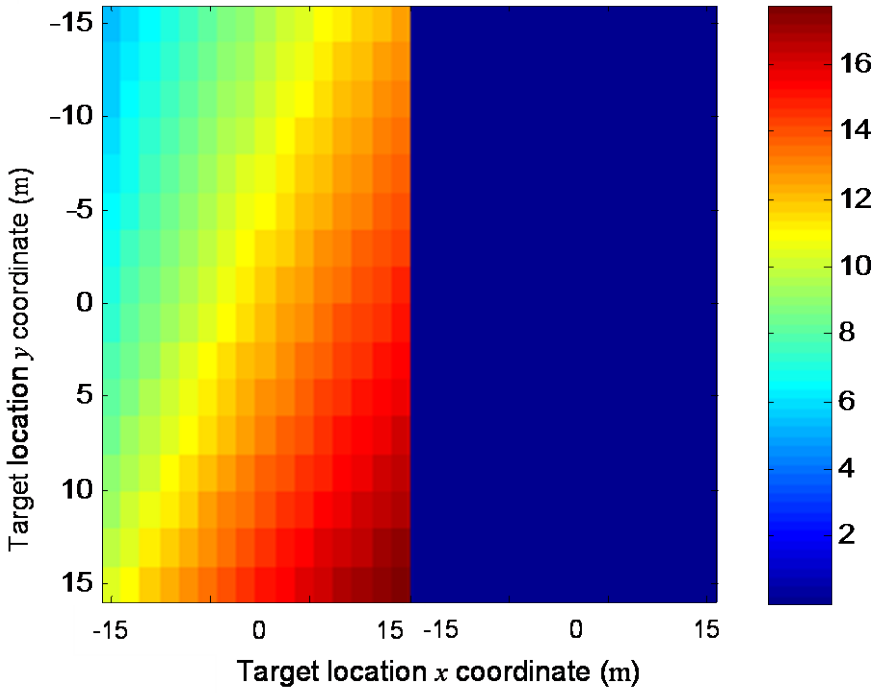

Figure 4.19. Localization error comparison (in meters) between different methods for the 3D localization model.

4.2.3 Convergence Problem

There is a rule of thumb based on the sampling frequency that indicates that the localization error should be proportional to c/f_s ; however, the maximum error, as shown in Fig. 4.19, is not in accordance. This is because the z direction geometry arrangement for the sensors is not optimized, according to the idea of Geometric Dilution of Precision (GDOP). The final localization error mainly comes from the z direction. Moreover, when the signal has a carrier frequency that is high, such as 300 MHz, the iterative method fails. This is because the ground plane behaves as a reflecting surface, so there are

significant reflections in the *z* direction, which makes the objective function behave fairly badly, as shown in Fig. 4.20. This is the same effect observed in the parallel wall model.

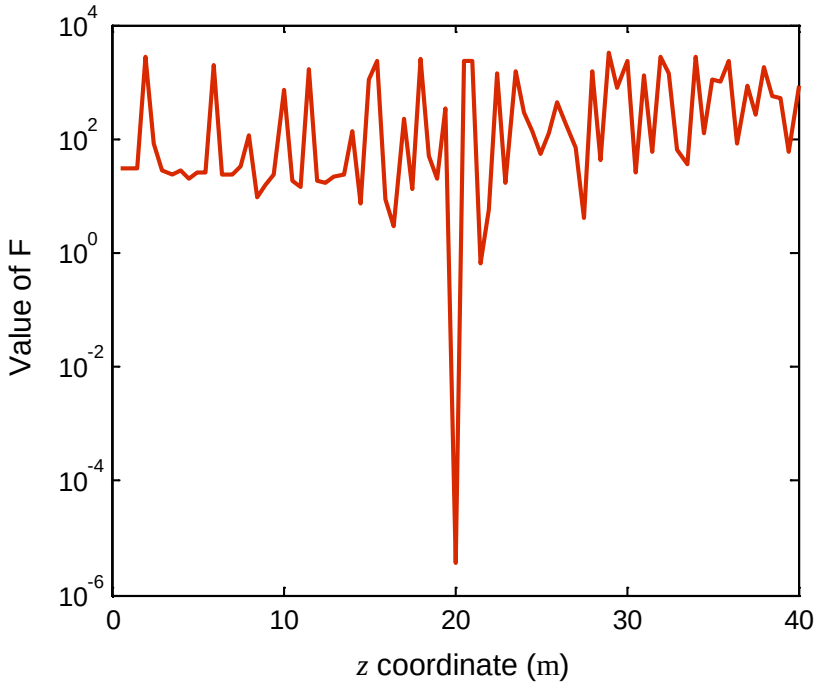

Figure 4.20. Plot of the objective function along the *z* coordinate when *x* and *y* are exact, for a carrier frequency of 300 MHz and a baseband frequency of 1 MHz.

Again, by applying the hybrid iterative method (finding appropriate *x* and *y* coordinates using the iterative method for each *z*, and using a global search for the *z* coordinate), the target location can be found effectively as long as the *z* coordinate is gridded fine enough in the global search. The error will then be on the order of the step size. However, this time, two coordinates are being determined by the iterative method, so the computation time is significantly increased. Due to limitations in computational resources, results are not shown here.

4.3 The 2D Enclosed Wall Model

The enclosed wall model as shown in Fig. 4.21 addresses the heaviest NLOS condition, when there are multiple walls present. In this case, reflections exist not only in the *x* direction, but also the *y* direction. The transfer function here is obtained from XFDTD, a commercial software based on the Finite Difference Time Domain (FDTD) method. To simplify the problem, the model is reduced to 2D (we set PEC as the boundary condition at the top and bottom of the structure, limit the height of the model, and make it extremely short in the vertical direction compared to the wavelength, and directly connect the side walls (modeling the walls of a building) to the top and bottom PEC surfaces. The surrounding boundary conditions are set to be those of a perfectly matched layer (PML)). A comparison between the simulation results and the analytic solution for the single-wall model is given in the next section. This shows that although the software is normally used for 3D simulations, under proper setup, the 2D simulation results are accurate enough for the use in our localization study.

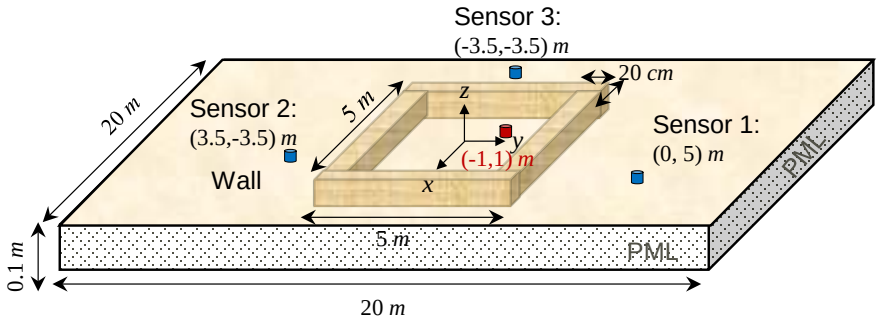

Figure 4.21. Enclosed wall model.

The simulation set up inside XFDTD is given as follows:

- The simulation area is 20 × 20 meters, and the enclosed area is 5 × 5 meters. To simulate a 2D structure, the height is set to 0.1 meters. The wall thickness is 20 cm,

and the wall permittivity is 6.3 - 0.69*j* (the same as wall case 2 in Chapter 3).

- The problem space is divided into 503 by 503 by 2 FDTD simulation cells.
- The radiating source is an ideal current feed connecting to the top and bottom PEC surfaces. Three point sensors are used to model the receivers. The target is located at (-1, 1) meters.
- The basic signal form is a Gaussian envelope with a 4 μs time constant, modulating a 3 MHz sinusoidal wave. The sampling time step used in the FDTD method is 8.9677×10^{-11} s.

4.3.1 Analytic Transfer Function for The 2D Single-Wall Model

Since the signal spectrum of the modulated Gaussian wave is focused in the frequency region between 2.5 MHz to 3.5 MHz, the transfer function, which is defined by $T(\omega) = E_z(\omega)/I(\omega)$, is considered to be trustworthy only inside this range.

For a 2D free-space simulation, the analytic transfer function for of the line source can be expressed as a Hankel function,

$$T_z = -\frac{\omega\mu}{4} H_0^{(2)}(k\rho). \tag{4.10}$$

For a 2D single-wall simulation (as shown in Fig. 4.22), the spectral domain immittance method can be employed to obtain the analytic transfer function.

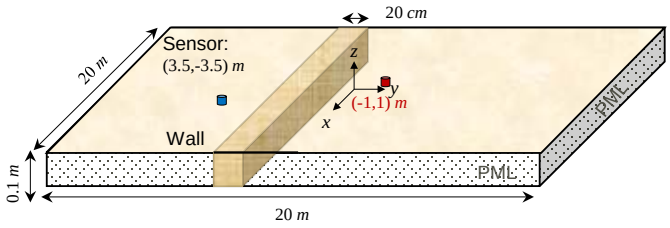

Figure 4.22. 2D single-wall model.

Assume that the target *a* is a vertical infinite current line source, located at (x_a, y_a), and that receiver *b* is located at (x_b, y_b). The reciprocity theorem is applied, followed by a rotation of the coordinates and a change the position of the origin, as shown in Fig. 4.23. In the spectral-domain method we represent a finite current sheet as a set of infinite phased current sheets. Then the phased current sheet launches a pair of plane waves. We decompose the current into two parts, which excite the TM_z and TE_z waves, respectively. The transfer function is obtained from the combined E_x field from these two modes by a double integral in the space domain. This process is exactly the same as that presented in Chapter 3, except that now the source is changed from the vertical electric dipole (used the Chapter 3) to the infinite current line, which is expressed as

$$\underline{J}_s\big|_{z=z_R} = \hat{\underline{x}} I \delta\left(y - y_R\right). \tag{4.11}$$

Then the final transfer function at the target position is

$$\begin{aligned} T\left(x_a, y_a, z_a\right) &= -\int_{-\infty}^{\infty} \frac{k_y{}^2 V_i^{TE}\,|_{x'=x_a}}{2\pi k_t{}^2} e^{-jk_y(-y_a+y_b)} dk_y \\ &= -\int_0^{\infty} \frac{V_i^{TE}\,|_{x'=x_a}}{2\pi} e^{-jk_t(-y_a+y_b)} dk_t - \int_0^{\infty} \frac{V_i^{TE}\,|_{x'=x_a}}{2\pi} e^{+jk_t(-y_a+y_b)} dk_t. \end{aligned} \tag{4.12}$$

The details of the derivation are available in Appendix A.3.

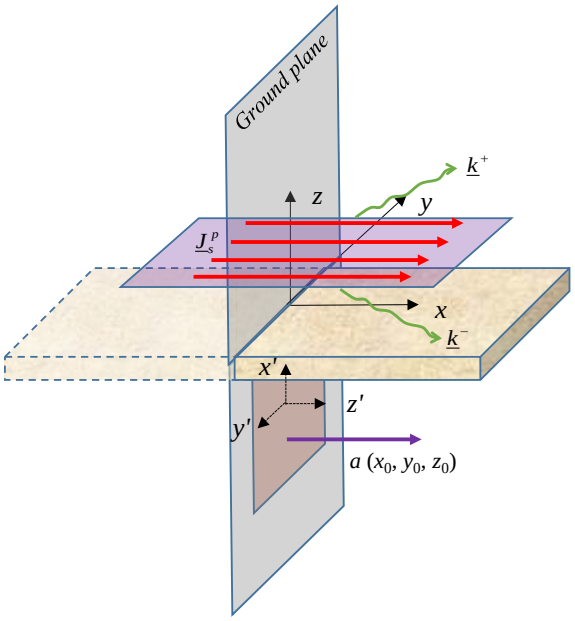

Figure 4.23. Spectral domain immittance method applied to the single-wall model.

The enclosed wall model has no analytic solution; thus in order to trust the 2D simulation results from a 3D simulation software, results from the first two models (free space and a single-wall) should be validated.

4.3.2 Comparison with the XFDTD Results

Figure 4.24 gives the transfer function comparison between the analytic results and the simulated numerical results for this single-wall model when the wall material becomes free space (2D free-space model). Figure 4.25 gives the comparison when the wall material is the same as that of the enclosed wall model (2D single-wall model).

Figure 4.24 shows very good agreement between the analytic solution and the numerical solution when the model becomes free space. Figure 4.25 shows a small phase error when the single-wall is present. However, this error is too small to affect the

localization accuracy. Hence, the simulation results from the FDTD method that yield the transfer function for the enclosed wall model are deemed to be trustworthy.

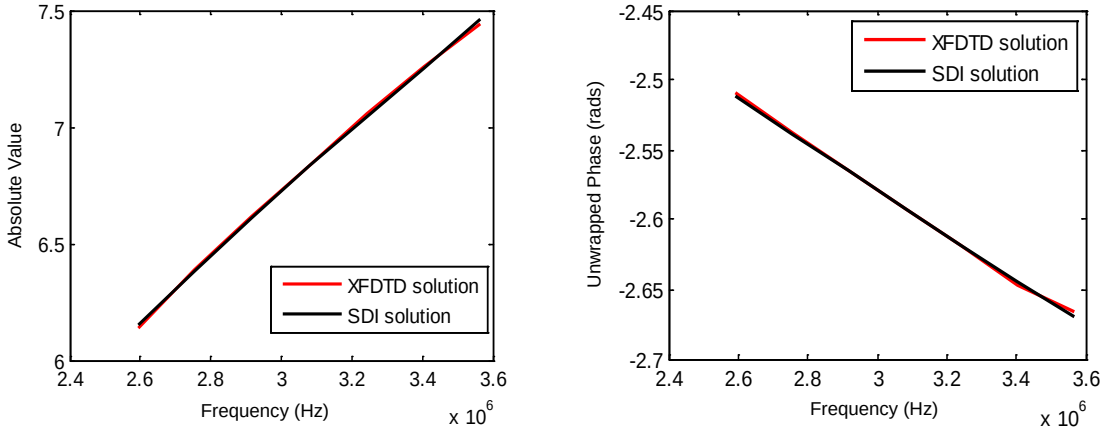

(a) (b)

Figure 4.24. Transfer function comparison between XFDTD and SDI solutions for free space. (a) Amplitude of the transfer function; (b) Phase of the transfer function.

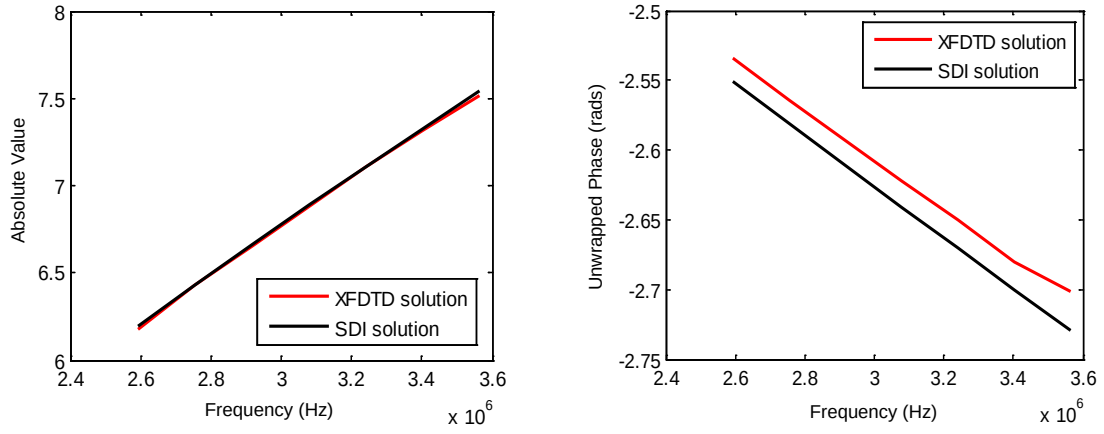

(a) (b)

Figure 4.25. Transfer function comparison between XFDTD and SDI solutions for the single-wall model. (a) Amplitude of the transfer function; (b) Phase of the transfer function.

4.3.3 XFDTD Simulation for 2D Enclosed Wall Model

Table 4.1 shows the localization results for different iterations in the enclosed wall model. Although there are multiple reflections inside the enclosed wall, the target can be accurately located, and the error is only 0.0067 meters. According to the rule of thumb resented earlier, the localization error should be around $c/f_s \approx 0.0269$ meters. The order of the localization error is as expected.

Table 4.1. Localization errors at different iterations.

ITERATION NO.	x (m)	y (m)	Error (m)
0	-1.3251	1.3172	0.4542
1	-0.9367	0.9005	0.1179
2	-1.0140	1.0283	0.0315
3	-0.9944	0.9962	0.0067
4	-0.9944	0.9962	0.0067

4.4 Conclusion

In this chapter, the iterative method using a de-embedding of the transfer function is applied to situations where multiple reflections exist. In order to investigate the behavior of the method when reflections are present, three models are developed and discussed: the parallel-wall model, the 3D localization model and the 2D enclosed wall model.

In the parallel-wall model, it's shown that in the absence of noise, the proposed iterative method converges to the true target location if the carrier frequency of the signal is in a relatively low frequency range (several MHz). However, the iterative method fails to converge when the carrier frequency is high, especially when the carrier frequency is extremely high (several hundred MHz), while the baseband frequency is low (several MHz). This is due to a standing-wave effect observed in the transfer function.

When the iterative method has convergence difficulties, the global search method can be used to perform the localization, but is quite time-consuming. Thus a hybrid iterative method is also proposed to effectively substitute for the original global search method to improve the efficiency. When the carrier frequency is high while the baseband frequency is also high, on the same order as the carrier frequency, a time-gating method can be used. However, this method has its own limitation – when the target is too close to the reflecting object, the method loses any advantage. A rule of thumb is given to calculate the threshold distance from the target to the back wall, beyond which the time-gating method offers improvement.

The 3D localization model shows that whenever the target is located above a ground, the ground always behaves like a reflector and causes the transfer function to exhibit a wilder behavior due to a standing-wave effect again for high carrier frequencies. Once again, a hybrid iterative method can be applied to effectively solve this problem; however, the iterative process is now used to search for two coordinates, x and y, for each global search coordinate z, making the entire process very numerically intensive compared to that of the parallel-wall case. Computer limitations prevent realizing results from this approach.

A 2D enclosed-wall model is simulated inside XFDTD. To verify the reliability of the numerically-obtained transfer function, an analytic transfer function for the 2D single-wall model is derived by using the SDI method, and compared with the numerical results obtained from the FDTD software. It is concluded that the software simulation results are trustworthy, and it is seen that the iterative method converges well when the carrier frequency of the signal is fairly low.

Chapter 5

Methods and Experimental Verification

This chapter describes an experiment using a 3D PEC ground plane model to verify the feasibility of proposed method, involving the de-embedding of the transfer function. As a comparison, the analytic transfer function is derived from image theory, and simulated in Matlab. The simulation results and the experimental results are consistent with each other and show good improvement for final localization accuracy and stability, respectively.

5.1 Introduction of 3D PEC Ground Plane Model

The experiment was set up at Sandia National Laboratories by Dr. Jeffery T. Williams. It was conducted within a chamber able to absorb signals over 700 MHz. Three broadband antennas were used as sensors to locate the target device. As shown in Fig. 5.1, Sensor 1 and Sensor 2 were identical, and Sensor 3 was different. Each antenna received approximately 1 ms of data at 2 GS/s and was connected to a short (6-foot) cable, then to a low noise amplifier (LNA) and finally to a 50-foot cable to the scope channel. The short cables and LNAs had nearly the same delay.

The geometry is shown in Fig. 5.1. The target was 30 inches above the PEC ground, Sensor 1 and Sensor 2 had a height of 1.3 meters, and Sensor 3 had a height of 1.25 meters. The target device was located at (1, 0) meters, measured at the device center. The target was a laptop, which had a physical size. Its radiating part(s) and signal form were unknown, and thus the precise target location was unknown. Therefore, in the following localization process, instead of comparing error, the x and y coordinates are

compared.

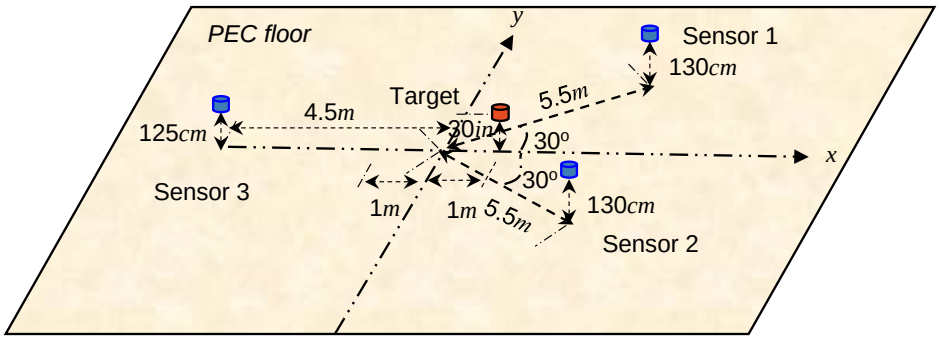

Figure 5.1. Localization experiment setup geometry.

After using a laptop, a desktop computer was also used to repeat the entire experiment. However, the signals received from the desktop are too weak to be used. Therefore, only the results from the laptop are discussed in this chapter. The laptop is either on the floor (on-floor case) or above the floor at a height of 30 inches (above-floor case). A time-frequency analysis is used to obtain the period of the signal waveform, as explained below. The time-frequency plots are clearer for the on-floor case, so the on-floor case is used in all of the time-frequency analysis to determine the period of the waveform. We do not apply the iterative method to this case, because the transfer function is equivalent to simply twice the transfer function in free space, and this does not help to improve accuracy; thus we only use the iterative method for the case when the laptop is above the floor.

5.2 Experimental Methods and Results

For this series of experiments, two scenarios are designed. In the first case, the receiver is receiving signals when the laptop is open and turned on. In the second case, the receiver is receiving signals when the laptop is off. In the latter case, the signals received at each sensor correspond to the background noise. Based on the assumption that

the environment is stable, the signal to background noise ratio can be approximately calculated as

$$SNR = \frac{\frac{1}{N}\sum_{n=0}^{N-1} x^2_{\text{on},n} - \frac{1}{N}\sum_{n=0}^{N-1} x^2_{off,n}}{\frac{1}{N}\sum_{n=0}^{N-1} x^2_{off,n}}. \quad (5.1)$$

From the experimental results, the SNR at Sensors 1, 2, 3 are 7.5 dB, 6.03 dB, and 8.15 dB, respectively, in the above-floor case.

The received signal has a long time series with 2×10^6 sample points. A frequency-domain analysis shows that the signal energy is mostly concentrated between 80 MHz and 300 MHz, as can be seen in Fig. 5.2, Fig 5.3, and Fig. 5.4 (in Figs. 5.2 and 5.3 the negative frequency region has been shifted by 2 GHz, so that the negative frequencies appear on the right side of the plot). The other frequency components are mostly contributed from noise.

Obviously, in Fig. 5.2(a), the signal repeats itself (at least approximately) around every 2000 sample points. A time-frequency analysis is used to determine the period more accurately. The period is used to divide the entire waveform into sections that are as identical as possible for application of the iterative method multiple times, i.e, for each different section. Figure 5.5 shows a generic picture to indicate how time-frequency analysis is applied. The entire time-domain waveform is first divided into sections. Within each section, the waveform is divided into segments, with each segment shifted from the others. A Fourier transform of the time series within each segment is then obtained. This figure is not drawn to scale in terms of the section or segment lengths; it simply illustrates the partitioning of the time series.

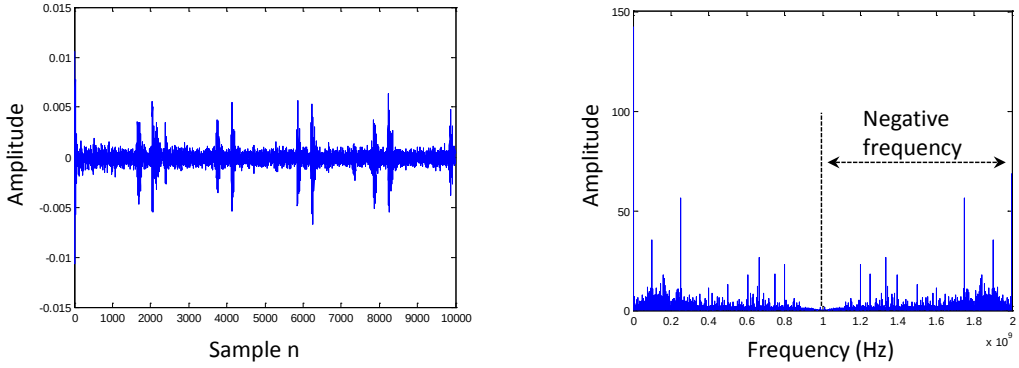

(a) (b)

Figure 5.2. Signal from receiver 3 when the laptop is on, in the above-floor case. (a) Time domain signal; (b) Frequency domain signal.

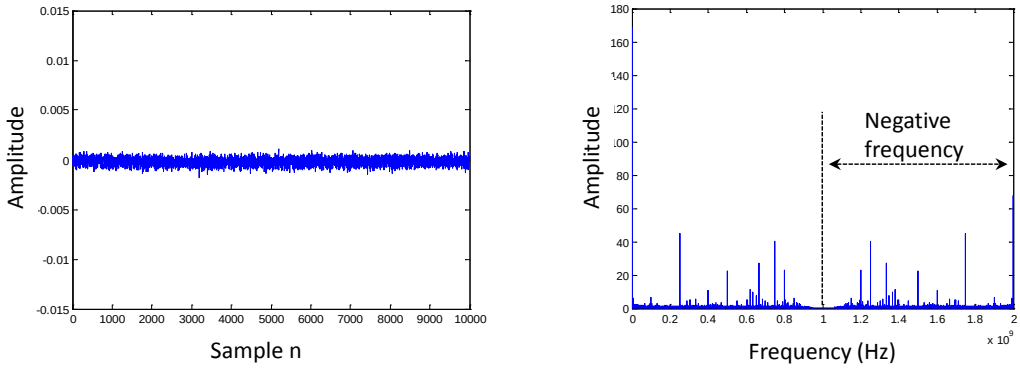

(a) (b)

Figure 5.3. Signal from receiver 3 when laptop is off, in the above-floor case. (a) Time domain signal; (b) Frequency domain signal.

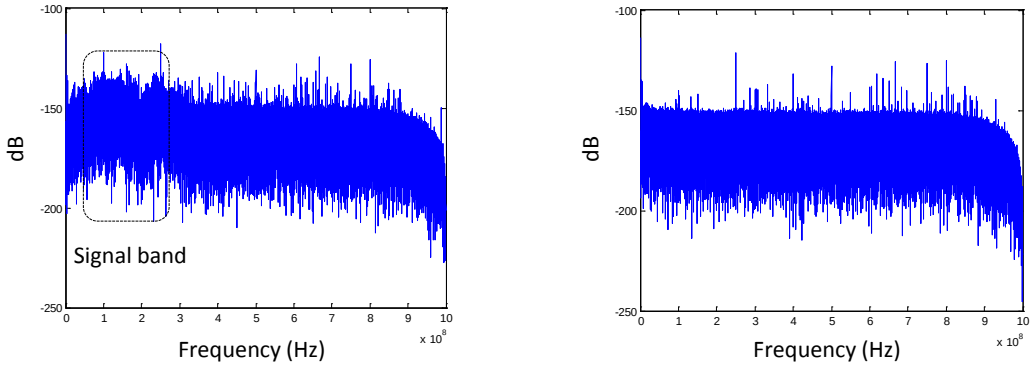

(a) (b)

Figure 5.4. Power spectral density at receiver 3, in the above-floor case. (a) Laptop is on; (b) Laptop is off.

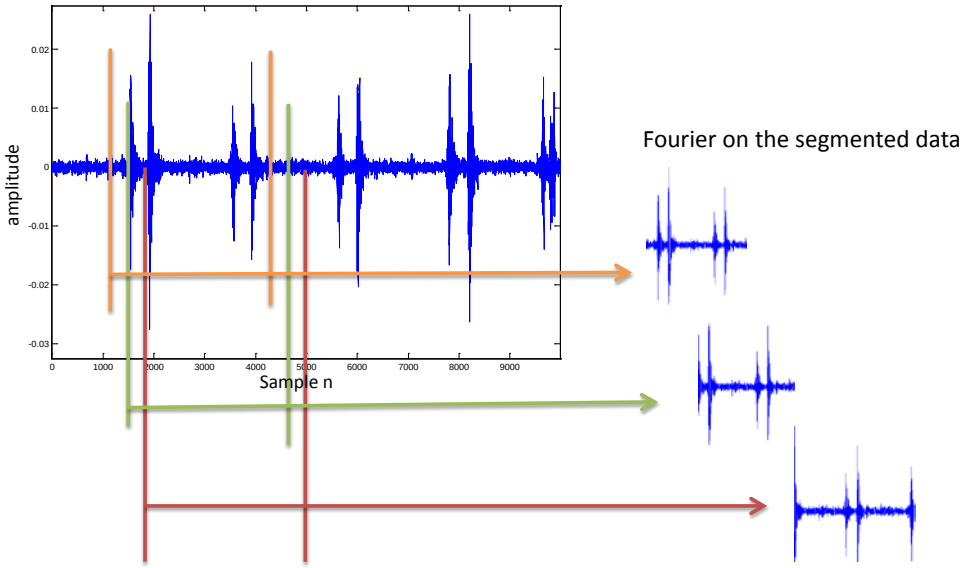

Figure 5.5. Time-frequency domain analysis on the experimental data (shown for the on-floor case). A section is subdivided into segments (three are shown here).

The entire time-domain waveform is first divided into 19 sections. The time-frequency plot for the on-floor case for a typical section is shown in Fig. 5.6. The section is divided into 1×10^5 segments, where each segment contains 500 samples. Each segment is offset from the previous one by one sample. Here *n* represents the segment number.

For each section, a visual inspection of the time-frequency plot is made. It is noticed that there is a periodic group of *n* values for which the single is strong. This particular section has 45 such groups. If we divide the difference in the values of *n* for the last and first groups by the number of these groups (45 in this case), we would obtain an average period of the waveform (the period in terms of the number of samples). In some sections some of the signal groups are less distinct, and they are ignored. So, for example, 42 groups are used in some sections instead of 45. Table 5.1 shows the period obtained for all 19 of the sections, and the number of signal groups that is used for the calculation of the period within that section. An average of the periods yields an average period of 2.0978×10^3 samples. Another type of average is also used, in which the entire time series (from all 19 sections) is used, and thus the total set of signal groups in the entire waveform is used, neglecting the ones that are less distinct. This result, shown at the bottom of Table 5.1, yields an identical result of 2.0978×10^3 samples for the average period. In time, this average period corresponds to a time period of $T = 1049\ \mu s$.

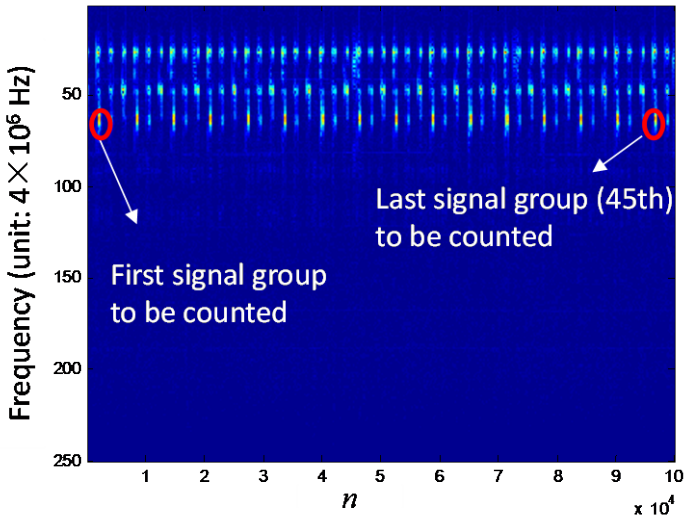

Figure 5.6. The first time window time-frequency plot.

Table 5.1. Period calculation for the experimental data.

Time window i	Start point n_{start}	End point n_{end}	Period N_i	Averaged period $P_i = \left(n_{end_i} - n_{start_i}\right) / N_i$
1	1911.5	96112	45	2.0933×10^3
2	2370.5	96807	45	2.0986×10^3
3	3007.5	97697	45	2.1043×10^3
4	3987.5	98354	45	2.0970×10^3
5	4653.5	99046	45	2.0976×10^3
6	5333.5	99710	45	2.0973×10^3
7	6004.5	94030	42	2.0958×10^3
8	327.5	94669	45	2.0965×10^3
9	933.5	95292	45	2.0969×10^3
10	1597.5	95946	45	2.0966×10^3
11	2227.5	96578	45	2.0967×10^3
12	2859.5	97166	45	2.0957×10^3
13	3475.5	97853	45	2.0973×10^3
14	4123.5	98437	45	2.0959×10^3
15	4729.5	99124	45	2.0977×10^3
16	6024.5	94047	42	2.0958×10^3
17	360.5	94692	45	2.0963×10^3
18	1002.5	95122	45	2.0915×10^3
19	1353.5	96624	45	2.1171×10^3
Averaged period for entire series	$P_{total} = \frac{\sum_1^{19}\left(n_{end_i} - n_{start_i}\right)}{\sum_1^{19} N_i} = 2.0978\times10^3;$		$T_{total} = \frac{P_{total}}{f_s}$	

Figure 5.7 presents a time-frequency plot for different sensors when using the estimated period as the section length, in which no overlap occurs between sections.

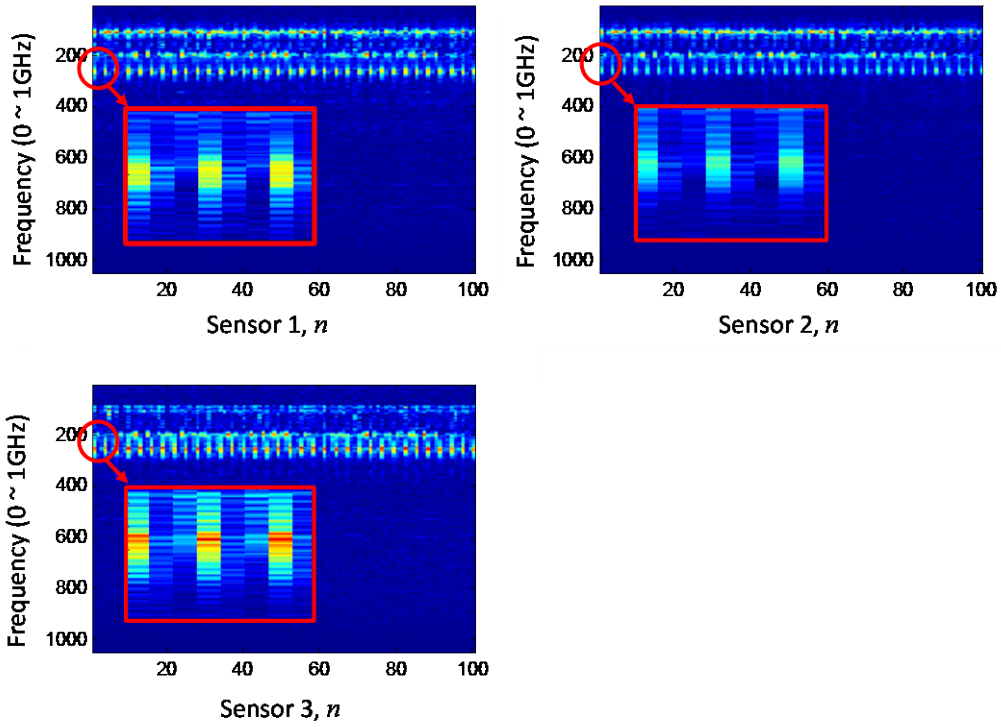

Figure 5.7. Time-frequency plot for the on-floor case, section length *T*.

To see whether or not de-embedding the transfer function (accounting for ground reflection) makes the time-frequency plot in the above-floor case more similar to that of the on-floor case (where the transfer function was not de-embedded), we de-embed the transfer function for the entire time series at the different receivers, and divide the processed signal at the last step in the iterative method into 100 sections.

The transfer function is derived from image theory according to the corresponding geometry, in which the target is seen as a simple *z*-directed electric dipole source. Since three sensors can only locate a 2D target, the *z* coordinate is assumed to be known.

Before applying the transfer function, the time-frequency plot is blurry and difficult to distinguish, as shown in Fig. 5.8. After the iterative process, the processed signal is much clearer, as shown in Fig. 5.9. Again, each section contains 2098 samples (T). Obviously, the NLOS effects are partially removed, so the signals are thus only slightly distorted, and only contaminated by environmental noise.

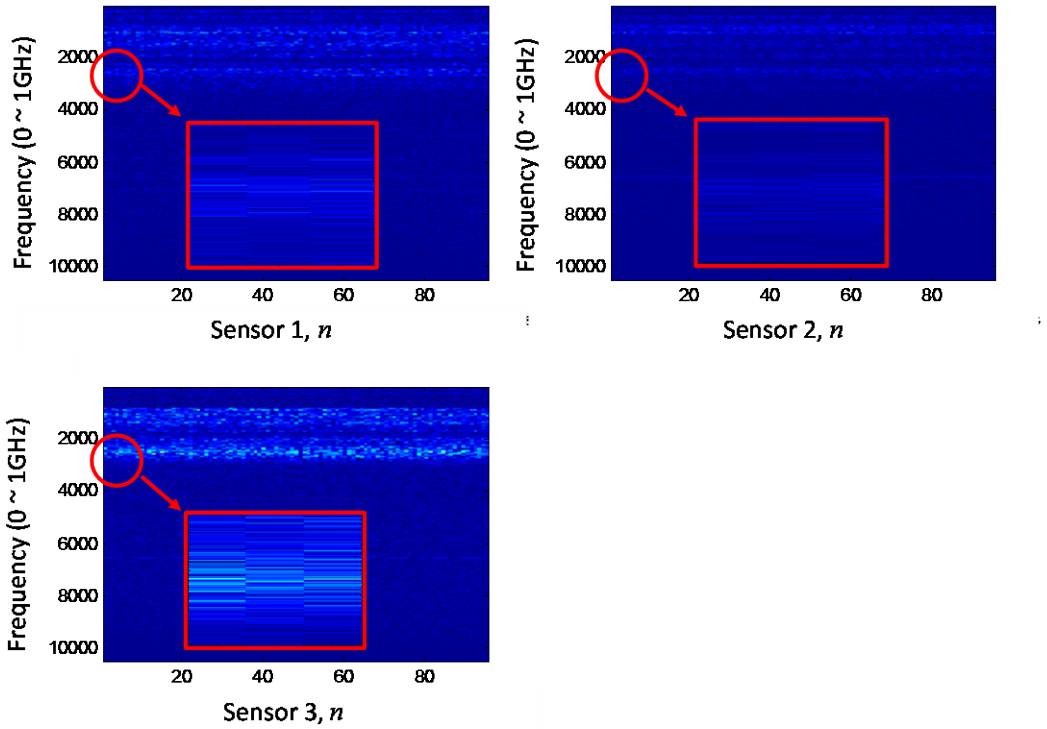

Figure 5.8. Time-frequency plot for the above-floor case before applying transfer function, section length T.

Because the transfer function is derived from the case assuming the source is simplified to be an electric dipole, it is not completely accurate, and so the results in Fig. 5.9 are not as clear as those in Fig. 5.7.

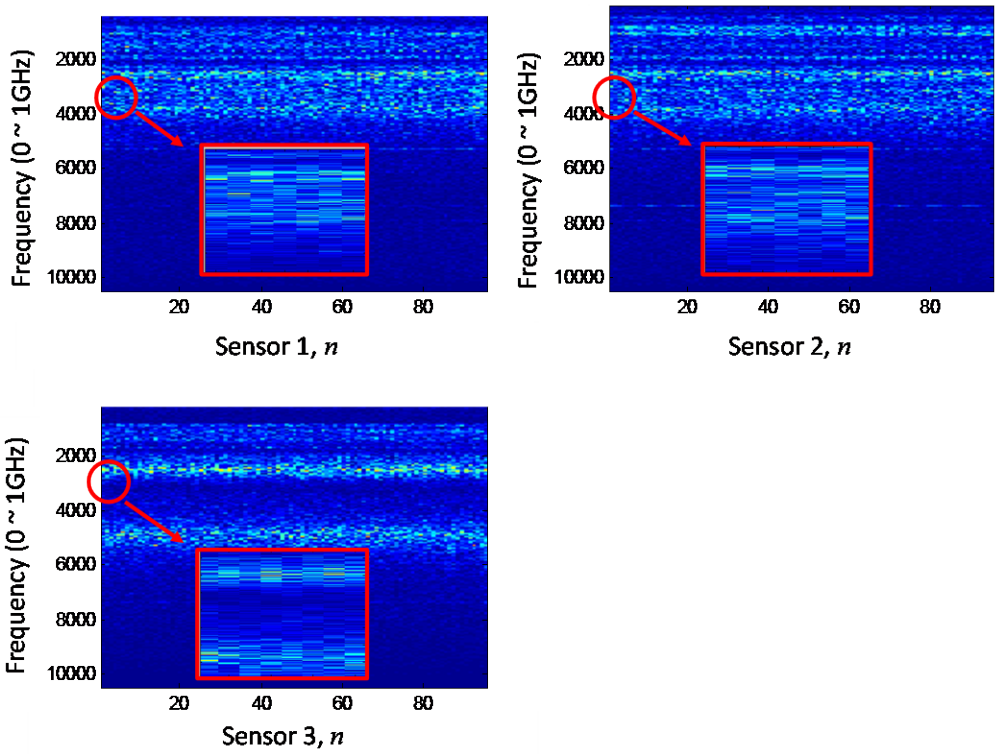

Figure 5.9. Time-frequency plot for the above-floor case after applying the transfer function, section length T.

Once the period of the radiated signal is found, it could be used to split the long time series, so that we are able to get different localization results from different sections to see if the iterative method is stable and accurate. The length of each new section is selected to be $10T$ (20980 samples, as shown in Fig. 5.10) so that the frequency domain signal form has a relatively high resolution.

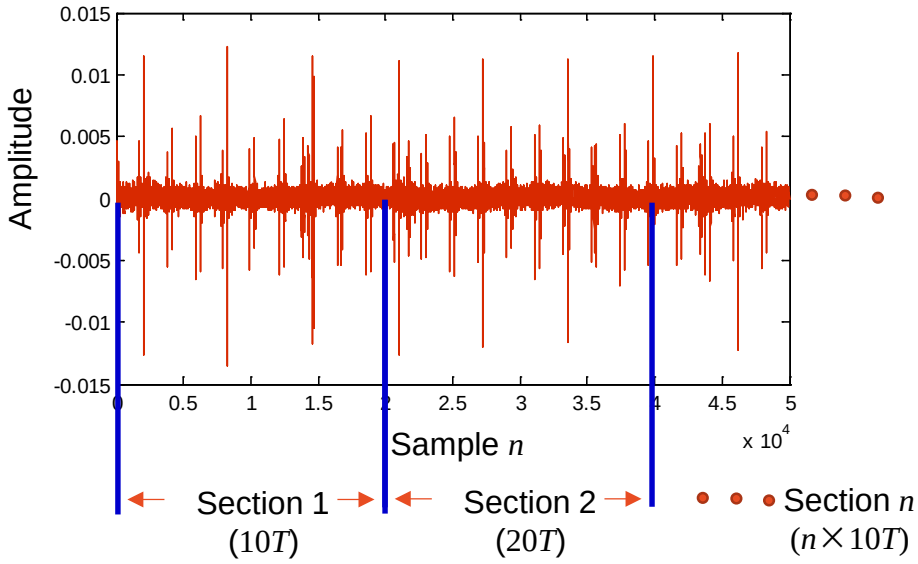

Figure 5.10. Sections of the time domain series at Sensor 3 in the above-floor case.

Figure 5.11 presents a comparison of localization results using the usual TDOA method and using the proposed iterative method; we estimate the x and y coordinates using the usual TDOA method (without using the transfer function) and the iterative method (using the transfer function). In order to improve localization accuracy, the interpolation method is applied to raise the sampling frequency from 2 GHz to 100 GHz. No denoising methods are applied. Both the x and y coordinates show a better stability after de-embedding the transfer function.

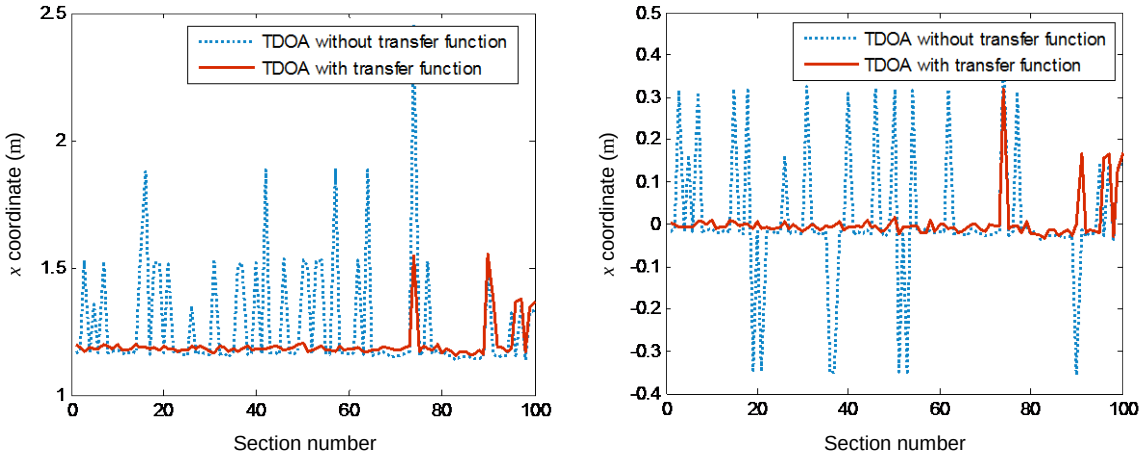

(a) (b)

Figure 5.11. Localization results for the experimental data after applying the TDOA method to the above-floor case with or without de-embedding the transfer function. (a) Results for the *x* coordinate; (b) Results for the *y* coordinate.

The next section (5.3) discusses our Matlab simulation and results. We have reason to believe that not only does localization becomes significantly more stable, but also that localization accuracy is greatly improved. Section 5.4 explains why the iterative process stabilizes the results.

5.3 Simulation Methods and Results

The 3D PEC ground plane model is validated inside Matlab. In order to see if localization accuracy is always improved by de-embedding the corresponding transfer function, the Monte Carlo method is employed, and different noise levels are introduced to the system. Both Gaussian white noise and the noise extracted from the experiment are applied and compared to see whether the iterative method could be affected by the type of noise. The above-floor case is used for all of the results in this section.

From the signal form analysis discussed above in Section 5.2, the received signal is seen to be concentrated in the 80 MHz to 300 MHz frequency band. Enlarging the time domain signal form shows that it looks like a Gaussian envelope modulating sinusoidal waves with multiple frequencies. The received signal has a period of about 2098 time samples. Therefore, a periodic signal with a Gaussian envelope modulating a sinusoidal wave is used to imitate the experimental signal. The baseband frequency is 100 MHz and the carrier frequency is set to be a single frequency of 250 MHz for simplicity. The signal contained 1×10^4 samples, which is consistent with the experimental results shown in Fig. 5.2. The Monte Carlo method is applied when noise was added to the system.

Figure 5.12 shows the time domain signal used for our Matlab simulation when the experimental noise is added to the system, and the SNR equals 5 dB.

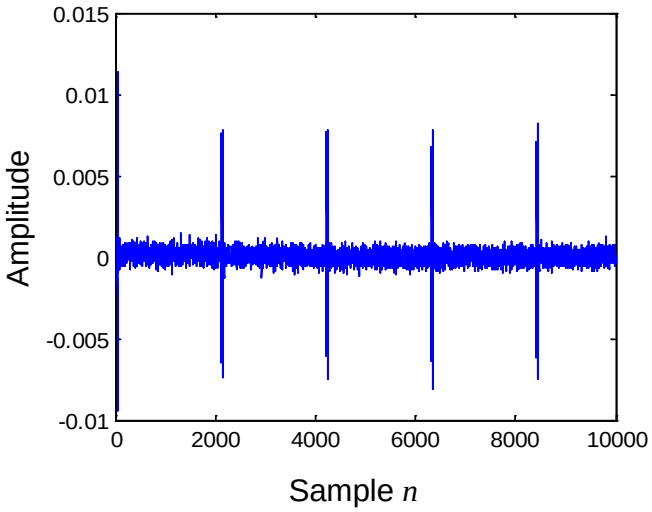

Figure 5.12. Simulated time domain signal form when the SNR is 5 dB, where the noise is extracted from the experiment.

Figure 5.13 presents the simulation results. Four different curves are presented in the plot. The square symbols represent the results when the experimental noise is

multiplied with a corresponding factor to realize a particular SNR and then add to the system. The circle symbols represent the results when Gaussian noise is added to the system. The region below 0 dB SNR is not trustworthy, because the noise power is greater than the signal power and most of the time the process does not converge. It can be seen that that the noise type does not influence the localization results. It is also clear that the iterative method provides better results compared to the usual TDOA method.

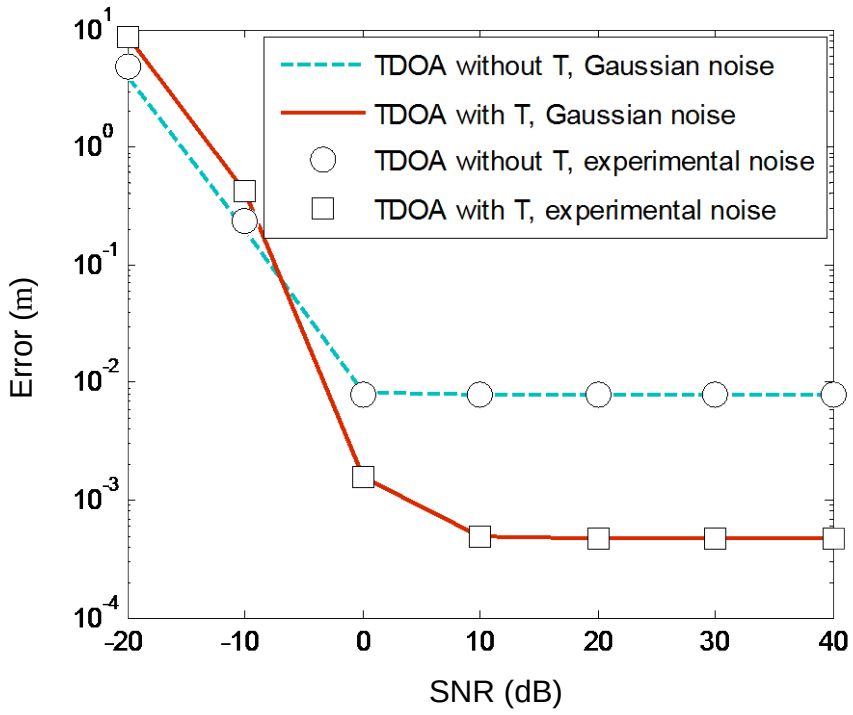

Figure 5.13. Matlab simulation results using the experiment geometry.

5.4 Explanation of Stability

Figure 5.11 shows that the results using the iterative method have better stability, except for several of the sections. From Fig. 5.11, we see that after de-embedding the transfer function Section 1 becomes well-behaved, while Section 100 is a bad section. Here we will discuss why most sections, like Section 1, have very stable localization

results after the iteration process, while a few sections, like Section 100, show a different behavior; we take these two sections as representative. In order to save time, in this section no interpolation method is implemented.

Looking at the time domain signal form at the different receivers, as shown in Fig. 5.14 ((a) Section 1, (b) Section 100), it is clear that at the third receiver in Section 100, between the 10000th samples to 15000th samples, the signal is partially distorted. This is probably because the third receiver has some problems occur occasionally, either from adjacent noise, or from the system; since the other receivers are well-behaved, the distortion is not because of NLOS effects.

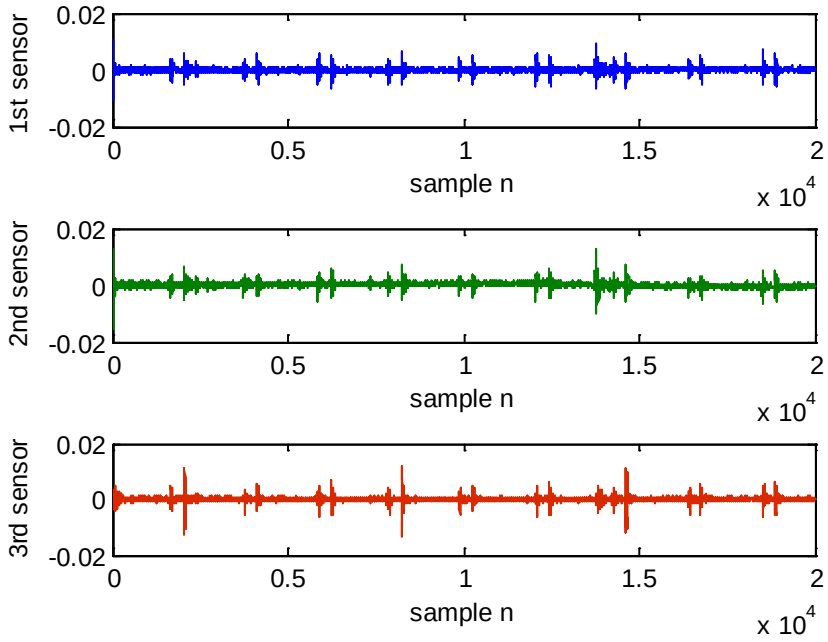

(a)

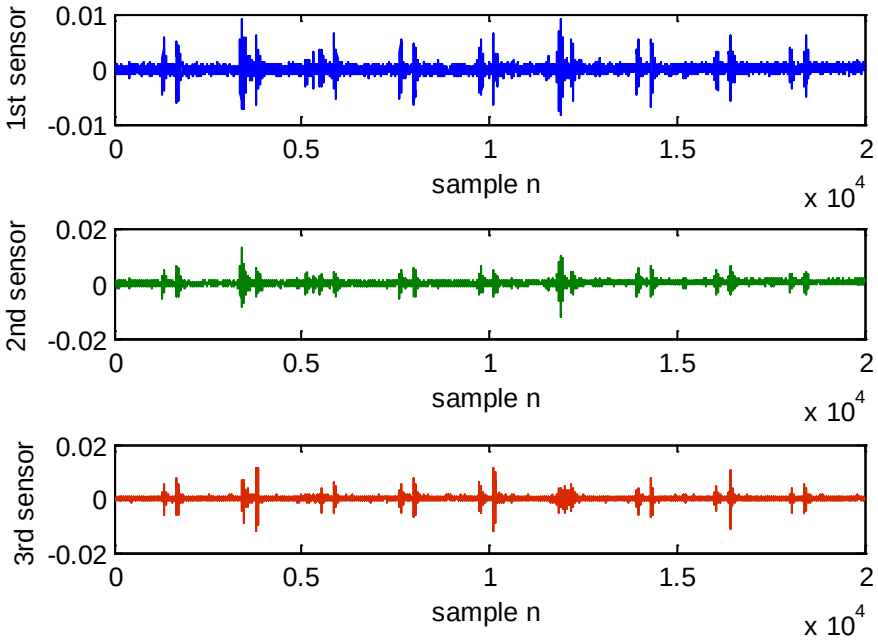

(b)

Figure 5.14. Time domain signal at different receivers before interpolation. (a) Section 1; (b) Section 100.

Section 1 also works well when only the usual TDOA method (without de-embedding the transfer function) is applied, so to make a comparison, we chose Sections 3 and 4. As seen in Fig. 5.11, when the usual TDOA method is applied, Section 4 is well-behaved, while Section 3 becomes victim to noise.

Figure 5.15 illustrates how noise directly affects the shape of the objective function – it shifts the entire plot. In Fig. 5.15(a), the minimum of the objective function is at (1.89 m, 0 m), while in Fig. 5.15(b) the minimum of the objective function is at (1.164 m, -0.041 m). Thus, the larger the noise, the further the minimum of the objective function is shifted from the true target position.

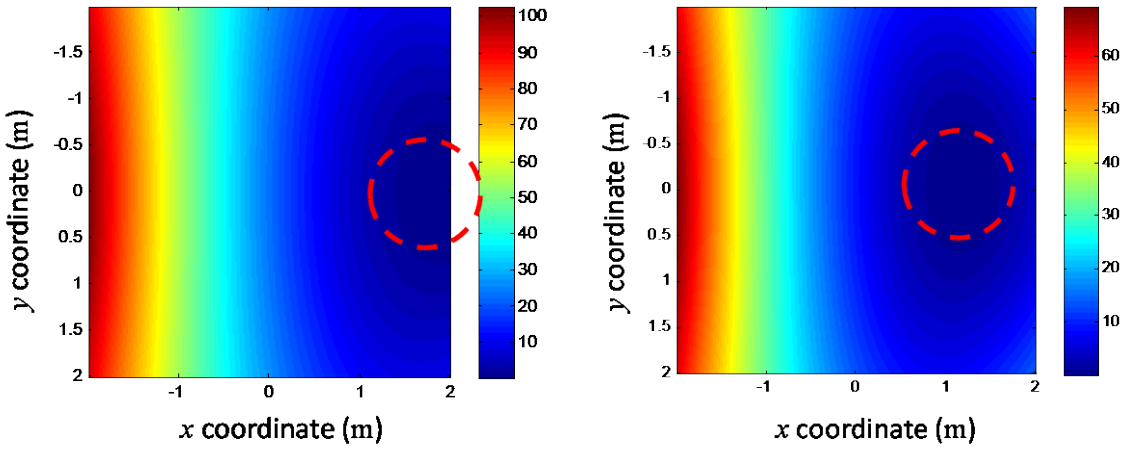

(a) (b)

Figure 5.15. Objective function plot for (a) Section 3 and (b) Section 4, without de-embedding the transfer function. The dashed circle shows the location of the minimum of the objective function (at the center of the circle).

From Fig. 5.11, we can see that accuracy of the results are enhanced for Sections 3 and 4 after de-embedding the transfer function; however, Section 100 remains badly behaved. Figure 5.16 explains the reason.

Figure 5.16 shows that after de-embedding the transfer function, noise will contaminate the objective function, but not shift the entire objective function. This means that as long as the noise does not contaminate the central minimum region, the true target position can be effectively determined (as happens with Sections 3 and 4).

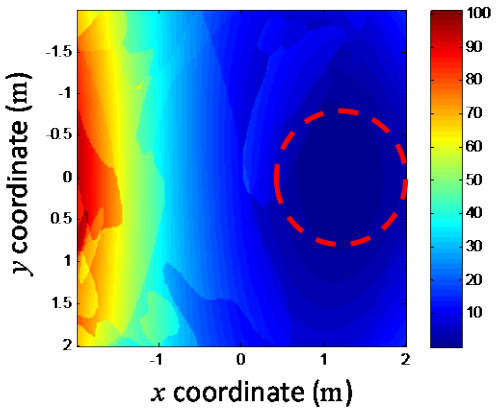

(a)

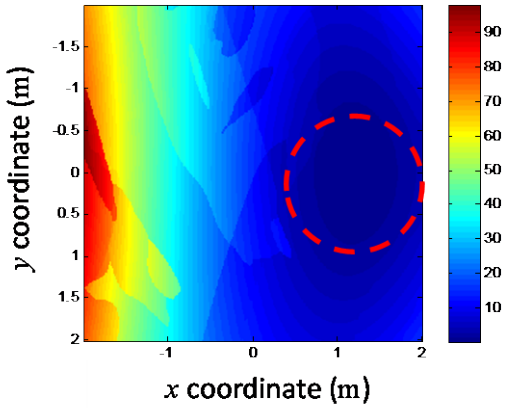

(b)

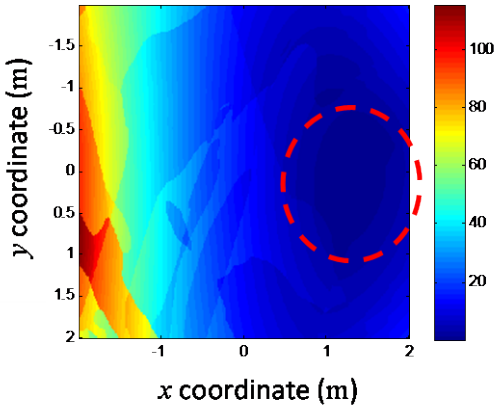

(c)

Figure 5.16. Objective function plot for Section 3 (a), Section 4 (b) and Section 100 (c) after applying transfer function.

In Fig. 5.16, the minimum of the objective function for Section 3 (part (a)) is at (1.21 m, 0 m), for Section 4 (part (b)) is at (1.21 m, 0 m), and for Section 100 (part (c)) is at (1.38 m, 0.16 m). Clearly, the objective function near the minimum for Section 100 is seriously contaminated (the minimum region is encircled by the red dashed circle).

5.5 Conclusion

This chapter describes an experiment to validate the proposed iterative method that de-embeds the transfer function. As a comparison, the same geometrical model is analyzed in a Matlab simulation. We conclude that the iterative method can improve localization accuracy for this configuration as long as the SNR is greater than 0 dB.

A time-frequency analysis is made to calculate the period of the radiated signal and then the section length is taken to be 10 times the obtained period. After applying the iterative method, the localization results become more accurate in the simulation and more stable in the experiment than those obtained when applying the usual TDOA method.

We have observed from the Matlab simulation that localization accuracy is enhanced after using the iterative method as expected, but it is not clear why the results became more stable in the experiment. Then in Section 5.4 we further explain this enhanced stability of the localization results after applying the iterative method in the experiment. In the usual TDOA localization, the noise shifts the entire objective function in the region of interest near the minimum. After de-embedding the transfer function, the effect from noise starts to contaminate the objective function, but does not shift it. This allows for the target position to be obtained more reliably.

Chapter 6

Conclusion

6.1 Conclusion

In this dissertation, a method was introduced for improving the usual time-difference-of-arrival (TDOA) localization method when non-line-of-sight (NLOS) effects are present. The method uses the known transfer function between the transmitting source ("target") and the receivers in the NLOS environment to improve the localization, accounting for the NLOS effects by means of the transfer function. The method is referred to as the iterative method, since it requires an iterative localization process. It is based on the usual TDOA, but uses the known transfer function for the propagation between the target and the receivers, as a function of the target and receiver locations, to de-embed the non-line-of-sight effects and calibrate the channel back to line-of-sight (free-space) propagation. The iterative method iteratively updates the transfer function between successive minimizations of the objective function, as the estimated target location changes in the search process. When it converges, the iterative method is very accurate, with the accuracy limited only by the sampling frequency at which the receiver data is recorded. However, the method may fail to converge, when the area of interest becomes large compared with a wavelength (i.e., at higher frequencies), especially when the radiated signal from the target has a small bandwidth.

A more robust method that is also more computationally intensive, referred to as the global search method, was also presented. This method does not require iteration, and therefore does not suffer from potential convergence problems, as it employs a global minimization search over the domain of interest, using an objective function that is based

on the de-embedded transfer function. This method is beneficial when the transfer function is not sufficiently smooth, and has multiple local minima within the region of interest, making the iterative method susceptible to either a lack of convergence or a failure to converge to the global minimum.

Chapter 2 first investigated TDOA localization accuracy when the signal was transmitting in line-of-sight (LOS) scenarios, and was only corrupted by the addition of Gaussian white noise. The errors in the localization were discussed and several denoising methods were proposed and compared.

Chapter 3 then proposed and examined several models under different NLOS scenarios, in order to test the proposed iterative method. The near-field dipole model represents a case where there are near-field effects; the single wall model is a canonical problem where there are refraction effects; the scattering-object model illustrates a scenario where there are scattering effects. In each case the transfer function was extracted from either analytic or numerical solutions, and simulations were conducted using either Matlab or XFDTD. Results showed that, in the absence of noise, the iterative method always converged to the true target position for the different cases, with an error that was only limited by the sampling frequency used in the cross-correlation to find the TDOA values.

Chapter 4 discussed the case in which the source was located inside an enclosure that results in multiple reflections. Three models were investigated: a parallel-wall model, a 3D localization model, and a 2D enclosed wall model. It was concluded that in the absence of noise, the proposed iterative method converges to the true target location if the received signal operates in a relatively low frequency range, but has difficulty converging

when operating at a high frequency range, so that the region of interest is fairly large compared with a wavelength. This is especially true when the carrier and baseband frequencies very different, meaning that the bandwidth of the signal is small. A global search method was successfully developed to solve this problem, but was found to be quite time-consuming. Then a hybrid iterative method and a time-gating method were proposed as a substitute for the global search method, resulting in a more efficient method that, while not as robust as the global search method, partially alleviates the convergence problems encountered with the iterative method.

Chapter 5 presents methods and results for an experiment and a corresponding simulation that was conducted to show the practicability of the proposed iterative method. The experiment was performed at Sandia National Laboratories. The conclusion was that the proposed iterative method greatly enhanced the stability of the localization that was achieved using the measured data from the experiment.

6.2 Future Work

In this research, the ground has been treated as an infinite perfect electric conductor (PEC), so an interesting future area of research would be to consider a practical ground instead of a PEC ground.

Throughout this research, only a vertical electric dipole was localized. So another hotspot of future research would be extend the method to include multiple targets and targets with different source types (electric or magnetic dipoles) and targets with unknown orientations.

Another attractive future application would be to apply the proposed method to realistic practical indoor public environments, so that NLOS effects include objects such

as tables, computers, and other obstacles inside the region. The transfer function could be obtained in this case from numerical simulations, e.g., based on the finite difference time domain method or the finite element method, or other methods such as the method of moments or high-frequency asymptotic techniques.

It was found that the computer simulation time was a key barrier when attempting to perform the localization in certain scenarios. Specifically, the iterative method fails to converge when the transmitting signal has a high carrier frequency, especially when the signal has a small bandwidth. The time-consuming global search method could be employed to get an accurate result if the domain is properly searched over a fine enough grid, but this will be numerically very time consuming. A useful future research area would be to apply parallel programming or other CPU or GPU acceleration approaches to this problem.

Another area of future work involves the study of other localization methods that can account for NLOS effects. The approach introduced here of de-embedding the transfer function is based upon the idea that the received signal can be enhanced by eliminating the NLOS effects in the TDOA localization algorithm. Other localization methods apart from the TDOA method, could be studied and compared. For example, one scheme could be to use the transfer function to reconstruct what the transmitted signal would be at the target, based on the signal received at a given receiver. Ideally this reconstructed transmitted signal would be identical regardless of which receiver was used. Hence, an objective function could be defined that measured the similarity in the reconstructed transmitted signal, and then searches over the region of interest to minimize

this function. This is another possible way in which the transfer function cold be used to de-embed the NLOS effects.

References

[1] A. H. Sayed, A. Tarighat, and N. Khajehnouri, "Network-Based Wireless Location: Challenges Faced in Developing Techniques for Accurate Wireless Location information," *IEEE Signal Processing Magazine*, vol. 22, no. 4, pp. 24–40, 2005.

[2] S. Gezici, "A Survey on Wireless Position Estimation," *Wireless Personal Communications.* vol. 44, no. 3, pp. 263–282, Feb. 2008.

[3] I. F. Akyildiz, W. Su, Y. Sankarasubramaniam, E. Cayirci, "Wireless Sensor Networks: a Survey," *Computer Networks*, vol. 39, no. 4, pp. 393-422, Mar. 15 2002.

[4] C.-Y. Chong, S. Kumar, "Sensor Networks: Evolution, Opportunities, and Challenges," *Proceedings of the IEEE*, vol. 91, no. 8, pp. 1247-1256, 2003.

[5] G. Mao, B. Fidan, (2009). *Localization Algorithms and Strategies for Wireless Sensor Networks* (1st Ed.)

[6] R. Peng, M. L. Sichitiu, "Angle of Arrival Localization for Wireless Sensor Networks," *Proceedings of Third IEEE Conference on Sensor and ad hoc Communications and Networks*, pp. 374-82, Reston, Sept. 28 2006.

[7] P. Kulakowski, J. Vales-Alonso, E. Egea-Lopez, W. Ludwin, J. Garcia-Haro, "Angle-of-arrival Localization Based on Antenna Arrays for Wireless Sensor Networks," *Computer & Electrical Engineering*, vol. 36, no.6, pp.1181-1186, Nov. 2010.

[8] Y.M. Chen, J.H. Lee and C.C. Yeh, "Two-Dimensional Angle-of-Arrival Estimation for Uniform Planar Arrays with Sensor Position Errors," *IET*, vol. 140, pp. 37-42, 1993.

[9] G. Carter, "Time Delay Estimation for Passive Sonar Signal Processing," *IEEE Transactions on Acoustic, Speech, and Signal Processing*, vol. 29, no. 3, pp. 463-470, 1981.

[10] G. Carter, (1993). *Coherence and Time Delay Estimation.* Piscataway, NL: IEEE Press.

[11] C. Knapp, & G. Carter, "The Generalized Correlation Method for Estimation of Time Delay," *IEEE Transactions on Acoustics, Speech, and Signal Processing*, vol. 24, no. 4, pp.320-327, 1976.

[12] D. Svecova and R.Z. Kocur, "Object Localization Using Round Trip Propagation Time Measurements," *18th International Conference RADIOELEKTRONIKA Prague*, 2008.

[13] B. Xu, G. Sun, R. Yu and Z. Yang, "High-accuracy TDOA-based Localization without Time Synchronization," *IEEE Transactions on Parallel and Distributed Systems*, vol. 24, no. 8, pp. 1567-1576, 2013.

[14] Y. Shang, W. Ruml, Y. Zhang and M.P.J. Fromherz, "Localization from Connectivity in Sensor Networks," *IEEE Transactions on Parallel and Distributed Systems*, vol. 15, no. 11, pp. 961-974, 2004.

[15] Y. Shang, W. Ruml, Y. Zhang and M.P.J. Fromherz, "Localization from Mere Connectivity," *Proceeding of the 4th ACM Int'l Symposium on Mobile Ad Hoc Networking & Computing*, pp. 201-212, 2003.

[16] P. Bergamo, G. Mazzini, “Localization in Sensor Networks with Fading and Mobility,” 13th IEEE International Symposium on Personal, Indoor and Mobile Radio Communications, pp. 750-754, 2002.

[17] E. Elnahrawy, X. Li, R. P. Martin, “The Limits of Localization Using Signal Strength: a Comparative Study,” *First Annual IEEE Conference on Sensor and Ad-hoc Communications and Networks*, pp. 406-414, 2004.

[18] K. Romer, “The Lighthouse Location System for Smart Dust,” *Proceedings of the 1st International Conference on Mobile Systems, Applications, and Services,* pp. 15-30, 2003.

[19] W. A. Gardner, C. K. Chen, “Signal-Selective Time-Difference-of-Arrival Estimation for Passive Location of Man-Made Signal Sources in Highly Corruptive Environments. I. Theory and method,” *IEEE Transactions on Signal Processing*, vol.40, no. 5, pp. 1185-1197, 1992.

[20] T. S. Rappaport, J. H. Reed, B. D. Woerner, “Position Location Using Wireless Communications on Highways of the Future,” *IEEE Communication Magazine*, vol. 34, no. 10, pp. 33-41, 1996.

[21] S. V. Schell, W. A. Gardner, “High-Resolution Direction Finding,” *Handbook of Statistics*, vol. 10, pp.755-817, 1993.

[22] C. Feng, W. Au, S. Valaee and Z. Tan, “Received-Signal-Strength-Based Indoor Positioning Using Compressive Sensing,” *IEEE Transactions on Mobile Computing*, vol. 11, no. 12, pp. 1983-1993, 2012.

[23] V. Seshadri, G.V. Zaruba and M. Huber, “A Bayesian Sampling Approach to Indoor Localization of Wireless Devices Using Received Signal Strength

Indication," *Proceedings of the Third IEEE International Conference on Pervasive Computing and Communications,* pp. 75-84, 2005.

[24] X. Li, "Collaborative Localization with Received-Signal-Strength in Wireless Sensor Networks," *IEEE Transactions on Vehicular Technology*, vol. 56, no. 6, pp. 3807-3817, 2007.

[25] C. Ma, R. Klukas, and G. Lachapelle, "A Non-Line-of-Sight Error-Mitigation for TOA Measurements," *IEEE Transactions on Vehicular Technology*, vol. 56, no. 2, pp. 641–651, Mar. 2007.

[26] M. P. Wylie, and J. Holtzman, (1996), "The Non-Line-of-Sight Problem in Mobile Location Estimation," *5th IEEE International Conference Universal Personal Communications*, Cambridge, MA, Sep. 29–Oct. 2, 1996.

[27] S.-S. Woo, H.-R. You, and J.-S. Koh, "The NLOS Mitigation Technique for Position Location Using IS-95 CDMA Networks," *Proceedings of IEEE VTC*, vol. 4, pp. 2556–2560, Sep. 2000.

[28] A. Seyed (Reza) Zekavat and R. Michael Buehrer. (2012). *Handbook of Position Location.* (1st Ed.).

[29] I. Guvenc, C. Chong, "A Survey on TOA Based Wireless Localization and NLOS Mitigation Techniques," IEEE Communications Surveys & Tutorials, vol. 11, no. 3, 2009.

[30] J. Khodjaev, Y. Park, and A. S. Malik, "Survey of NLOS Identification and Error Mitigation Problems in UWB-based Positioning Algorithms for Dense Environments," *Annals of Telecommunications*, Vol. 65, no. 5, pp 301–311, June. 2010.

[31] L. Cong, W. Zhuang, "Non-Line-of-Sight Error Mitigation in Mobile Location, " *IEEE Transactions on Wireless Communications*, vol. 4 , no. 2 , pp. 560–573 , 2005.

[32] S. Yarkan and H. Arslan, "Identification of LOS in Time-Varying, Frequency Selective Radio Channels," *EURASIP Journal on Wireless Communications and Networking*, vol. 2008, pp. 1-14, Feb. 2008.

[33] W. Xu, "Non-Line-of-Sight Identification in Wireless Localization via Phase Difference Statistics across Two Antenna Elements," *IET Communications*, vol. 5, no.13, pp. 1814–1822, Sep. 2011.

[34] W. Xu, "Multi-Antenna Non-Line-of-Sight Identification Techniques for Target Localization in Mobile ad-hoc Networks," PhD. Dissertation, Department of Electrical Engineering, Michigan Technological University, 2011.

[35] L. Konrad and W. Matt, "Motetrack: a Robust, Decentralized Approach to RF-Based Location Tracking," *International Workshop on Location and Context-Awareness*, 3479, pp. 63–82, 2005.

[36] C. Seow and S. Tan, "Non-Line-of-Sight Localization in Multipath Environments," *IEEE Transaction on Mobile Computing*, vol. 7, no. 5, pp. 647– 660, 2008.

[37] H. Song, H. Wang, K. Hong, and L. Wang, "A Novel Source Localization Scheme Based on Unitary Esprit and City Electronic Maps in Urban Environments," *Progress in Electromagnetics Research. PIER*, vol. 94, no. 94, pp. 243–262, 2009.

[38] Z. Wang and S. A. Zekavat, "Omni-Directional Mobile NLOS Identification and Localization via Multiple Cooperative Nodes," *IEEE Transactions on Mobile Computing*, vol. 11, no. 12, pp. 2047–2059, Oct. 2012.

[39] I. Gven, C.-C. Chong, F. Watanabe, and H. Inamura, “NLOS Identification and Weighted Least-Squares Localization for UWB Systems Using Multipath Channel Statistics,” *EURASIP Journal on Advances in Signal Processing*, vol. 2008, pp. 1–14, 2008.

[40] Y. T. Chan and K. C. Ho, “A Simple and Efficient Estimator for Hyperbolic Location,” *IEEE Transactions on Signal Processing*, vol. 42, no. 8, pp. 1905–1915, 1994.

[41] X. Wang, Z. Wang, and B. O’ Dea, “A TOA-Based Location Algorithm Reducing the Errors Due to Non-Line-of-Sight (NLOS) Propagation,” *IEEE Transactions on Vehicular Technology*, vol. 52, no. 1, pp. 112–116, 2003.

[42] A. Swami and B. M. Sadler, “On Some Detection and Estimation Problems in Heavy-Tailed Noise,” *Signal Processing*, vol. 82, pp. 1829–1846, 2002.

[43] S. Marano, W. M. Gifford, H. Wymeersch, M. Z. Win, “NLOS Iidentification and Mitigation for Localization Based on UWB Experimental Data,” *IEEE Journal on Selected Areas in Communications*, vol. 28, no. 7, Sept. 2010.

[44] B B. Yang and J. Scheuing, “A Theoretical Analysis of 2D Sensor Arrays for TDOA Based Localization,” *IEEE Int. Conf. Acoustics, Speech and Signal Processing, 2006. ICASSP 2006 Proceedings*. Toulouse, May 14-19, 2006.

[45] D. R. Jackson and J. T. Williams, “A Comparison of CAD Models for Radiation from Rectangular Microstrip Patches,” *International Journal of Microwave and Millimeter-Wave Computer Aided Design*, vol. 1, No. 2, pp. 236-248, April 1991.

[46] T. Itoh and W. Menzel, “A Full-wave Analysis Method for Open Microstrip Structures,” *IEEE Trans. Antennas and Propagation*, vol. 29, no. 1, Jan. 1981, pp. 63-68.

Appendices

A.1 Transfer Function for The Single-Wall Model: Reciprocity Method

As discussed in Chapter 3, the receivers are put in the far field, so that plane wave theory can be applied. The plane wave can thus be decomposed into TM_x mode and TE_x mode. While in the far field, only TE_x mode needs to be considered. Because the target and receivers have height, the reflections from the ground should also be taken into consideration.

Figure A.1 shows the propagation route of the transmitted signal from top view of the single-wall model.

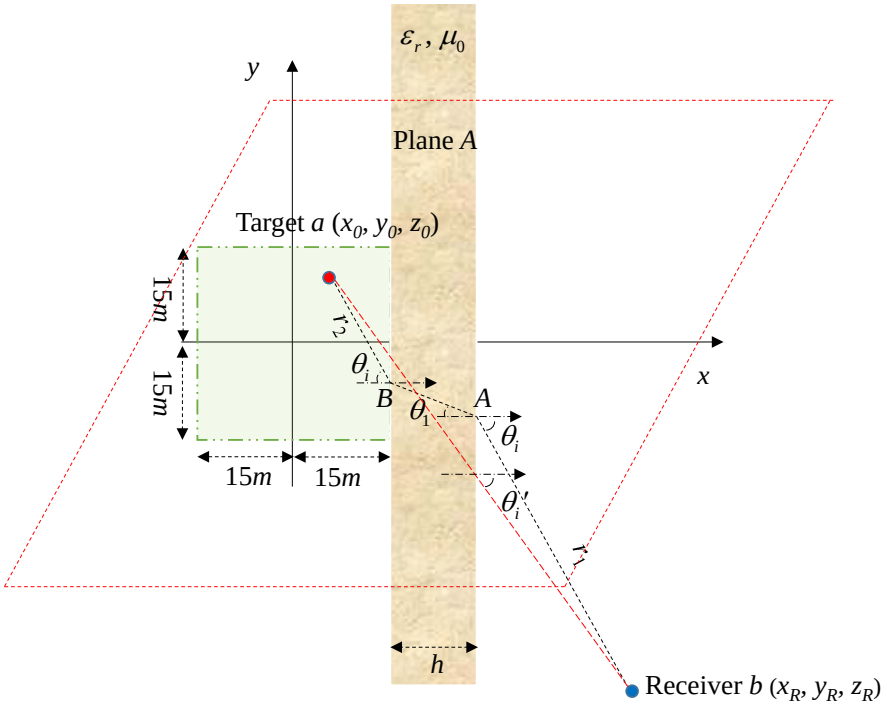

Figure A.1. Top and side view of the configuration for the single-wall model.

When the target is modeled as a *z*-directed electric dipole, from the reciprocity principle, in order to know the field at position *b*, we can put a testing dipole at *b*, and

$< a, b > = < b, a >$ (The field produced by source *a* at position *b*, equals the field produced by source *b* at position *a*).

As *b* is put in the far field, the incident field from source *b* to position *a* is also treated as a plane-wave field. Figure A.2 shows the local system for dipole *b* after applying the reciprocity algorithm.

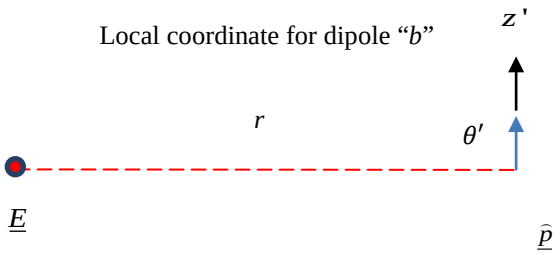

Figure A.2. Local coordinate for dipole *b*.

In order to determine the incident field *E*, let $\underline{E} \sim \underline{\hat{\theta}}' \left(\frac{j\omega\mu_0}{4\pi r} \right) e^{-jkr} \sin(\theta')$, where $\theta' = \frac{\pi}{2}$, so that

$$\underline{E} \sim \underline{\hat{\theta}}' \left(\frac{j\omega\mu_0}{4\pi r} \right) e^{-jkr} = -\underline{\hat{p}} \left(\frac{j\omega\mu_0}{4\pi r} \right) e^{-jkr}, \qquad \text{(A.1)}$$

when $r \to \infty$, Hence $\underline{E} \sim \underline{\hat{p}} E_0$ where $E_0 = \left(\frac{-j\omega\mu_0}{4\pi r} \right) e^{-jkr}$. The propagation process inside the wall after applying the reciprocity algorithm is shown in Fig. A.3.

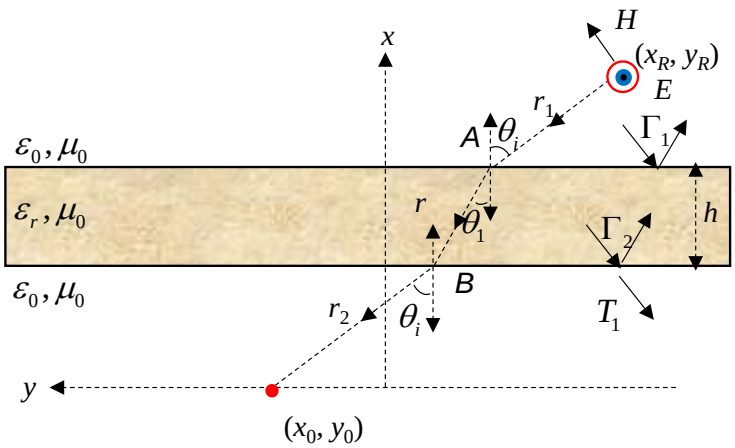

Figure A.3. Refraction process inside the wall.

The target is modeled as a vertical electric dipole, in the far field, and only E_θ exists. The height differences of the target and the receivers can be ignored because of the long distance, thus all of them can be treated as on the floor. Thus, θ approximately equals 90° at each receiver and only the TE_x mode needs to be taken into consideration. From the image theory shown in Fig. A.4 (for simplification, we ignore the wall in the picture), E'_θ can be calculated by vector addition of E_θ from the target a and the corresponding image target.

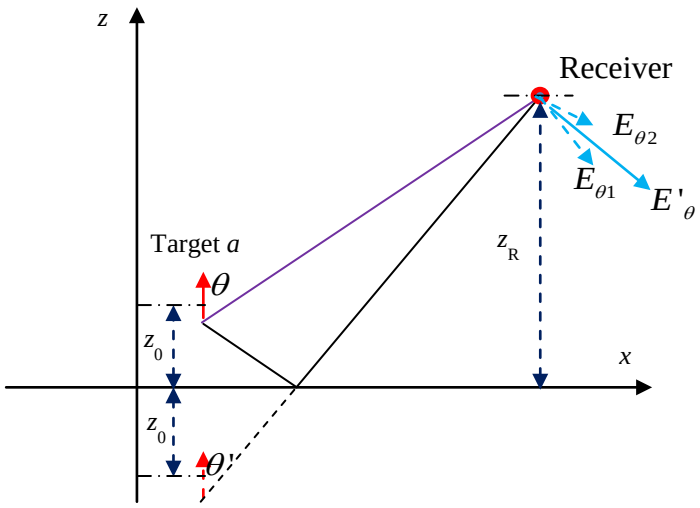

Figure A.4. Image theory applied for the target.

A) TE_x mode from the target

We assume that the transmission coefficient is T, the reflection coefficient of the first interface is Γ_1 , and the reflection coefficient of the second interface is $\Gamma_2 = -\Gamma_1$. The transverse equivalent network for TE_x is shown in Fig. A.5.

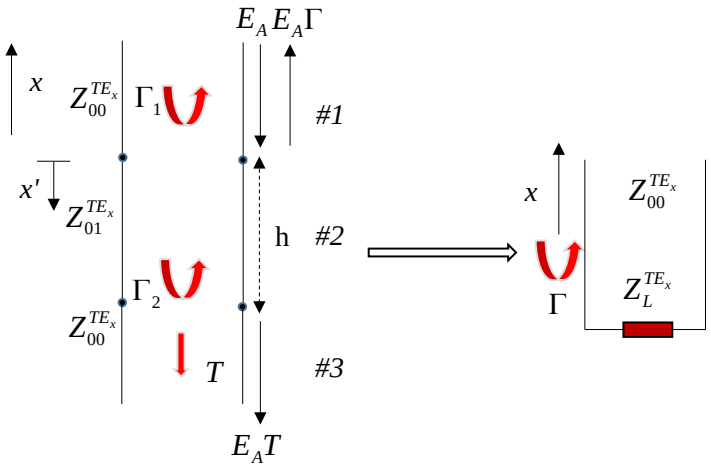

Figure A.5. Transverse equivalent network for the plane-wave field.

Using the *TEN* method, we define $n_1 = \sqrt{\varepsilon_r \mu_r}$, so that $\sin\theta_i = n_1 \sin\theta_1$. Here θ_i is the incident angle and θ_1 is the refraction angle. Approximately,

$$\theta_i \approx \theta_i' = \arccos\left(\frac{x_0 - x_R}{\sqrt{(x_0 - x_R)^2 + (y_0 - y_R)^2 + (z_0 - z_R)^2}} \right), \tag{A.2}$$

so that the characteristic impedances for region 2 and region 3 are

$$Z_{01}^{TE_x} = \frac{\omega\mu}{k_{x1}}, Z_{00}^{TE_x} = \frac{\omega\mu_0}{k_{x0}}, \tag{A.3}$$

where $k_{x1} = k_1 \cos(\theta_1) = \mathrm{k}_1 \sqrt{1 - \left(\frac{\sin(\theta_i)}{n_1} \right)^2}$ and $k_{x0} = k_0 \cos(\theta_i)$. The reflection coefficients at $z' = 0$ and $z' = h$ are

$$\Gamma_1 = \frac{Z_{01}^{TE_x} - Z_{00}^{TE_x}}{Z_{01}^{TE_x} + Z_{00}^{TE_x}}, \quad \Gamma_2 = -\Gamma_1. \tag{A.4}$$

Simplifying the TEN as in Fig A.5, the reflection coefficient is

$$\Gamma = \frac{Z_L^{TE_x} - Z_{00}^{TE_x}}{Z_L^{TE_x} + Z_{00}^{TE_x}}, \tag{A.5}$$

where $Z_L^{TE_x} = Z_{01}^{TE_x} \dfrac{Z_{00}^{TE_x} + jZ_{01}^{TE_x} \tan\left(k_{x1}h\right)}{Z_{01}^{TE_x} + jZ_{00}^{TE_x} \tan\left(k_{x1}h\right)}$.

In Region 2, we use x' as the propagation coordinate, so the voltage is expressed as

$$\begin{aligned} V_2(x') &= \left(Ae^{-jk_{x1}(x'-h)} + A\Gamma_2 e^{+jk_{x1}(x'-h)} \right) \\ &= A\left(e^{-jk_{x1}(x'-h)} + \Gamma_2 e^{+jk_{x1}(x'-h)} \right). \end{aligned} \tag{A.6}$$

At $x' = 0$: $V_2(0) = V_1(0) \Rightarrow A\left(e^{+jk_{x1}h} + \Gamma_2 e^{-jk_{x1}h} \right) = E_A(1+\Gamma) \Rightarrow A = E_A \left(\dfrac{1+\Gamma}{e^{+jk_{x1}h} + \Gamma_2 e^{-jk_{x1}h}} \right)$.

At $x' = h$: $V(h) = V_2(h) = A(1+\Gamma_2)$.

In Region 3, the voltage is expressed as

$$V_3(x') = V(h)e^{-jk_{x0}(x'-h)}, \tag{A.7}$$

and hence $V(h)e^{-jk_{x0}(x'-h)} = E_A T e^{-jk_{x0}x'}$.

The transmission coefficient is then

$$T = \frac{1}{E_A}[(\mathrm{A}(1+\Gamma_2))]\mathrm{e}^{+jk_{x0}h} = \left(\frac{1+\Gamma}{\mathrm{e}^{+jk_{x1}h}+\Gamma_2\,\mathrm{e}^{-jk_{x1}h}}\right)\left(1+\Gamma_2\right)\mathrm{e}^{+jk_{x0}h}, \tag{A.8}$$

and at the incident point *A*, the electric field is

$$E_A = \left(\frac{-j\omega\mu_0}{4\pi r_1}\right)e^{-jkr_1}, \tag{A.9}$$

where $r_1\cos(\theta_i)+h+\frac{L}{2} = x_R \Rightarrow r_1 = \frac{x_R - h - \frac{L}{2}}{\cos(\theta_i)}$, $r_2\cos(\theta_i)+x_R = \frac{L}{2} \Rightarrow r_2 = \frac{\frac{L}{2}-x_0}{\cos(\theta_i)}$. Here r_1 is the propagation length between point *A* and position, r_2 is the propagation length between point *B* and the target *a*, and *L* is the length of the enclosed area.

The TE_x wave represents the E_θ field. Since the position *b* is above the floor, $\theta = \arctan\left(\frac{\sqrt{(x_0-x_R)^2+(y_0-y_R)^2}}{|\,z_0-z_R\,|}\right)$ (we assume a new coordinate system where the origin is at the target position). We have

$$\begin{aligned} &E_{\theta 1} = E_A(-\sin(\theta))T^{TE_x}e^{-jk_0r_2}, \\ &\sin(\theta) = \left(\frac{\sqrt{(x_0-x_R)^2+(y_0-y_R)^2}}{\sqrt{(x_0-x_R)^2+(y_0-y_R)^2+(z_0-z_R)^2}}\right). \end{aligned} \tag{A.10}$$

For the right-hand side, we insert the incident coefficients (A.9), (A.8) to obtain (where *r* is the distance between target and receiver):

$$
\begin{aligned}
E_z &= -E_{\theta 1} \\
&= -\sin(\theta)\left(\frac{j\omega\mu_0\cos(\theta_i)}{4\pi(x_R - h - \frac{L}{2})}\right)\left(\frac{1+\Gamma}{e^{+jk_{x1}h} + \Gamma_2 e^{-jk_{x1}h}}\right) \\
&\quad (1+\Gamma_2)e^{+jk_{z0}h}e^{-jk_0 r}.
\end{aligned} \tag{A.11}
$$

Meanwhile, the moment of the dipole is *Il*=1, so that the transfer function is the same as E_z, and thus is represented as

$$
\begin{aligned}
T_1 &= -\sin(\theta)\left(\frac{j\omega\mu_0\cos(\theta_i)}{4\pi(x_R - h - \frac{L}{2})}\right)\left(\frac{1+\Gamma}{e^{+jk_{x1}h} + \Gamma_2 e^{-jk_{x1}h}}\right) \\
&\quad (1+\Gamma_2)e^{+jk_{z0}h}e^{-jk_0 r}.
\end{aligned} \tag{A.12}
$$

B) TE_x mode from the image target

The image target position is (x_0, y_0, -z_0). The algorithms used are the same as above, and the incident angle at the wall is

$$
\theta_i^{image} \simeq \arccos\left(\frac{x_0 - x_R}{\sqrt{(x_0 - x_R)^2 + (y_0 - y_R)^2 + (z_0 + z_R)^2}}\right). \tag{A.13}
$$

Another difference is the angle θ' instead of θ. (This was shown in Fig. A.4. We assume another coordinate system where the origin is at the image target position). The angle is expressed as

$$
\theta' = \arctan\left(\frac{\sqrt{(x_0 - x_R)^2 + (y_0 - y_R)^2}}{|z_0 + z_R|}\right), \tag{A.14}
$$

so the transfer function received from the image target is

$$
\begin{aligned}
T_2 &= E_{z2} = -E_{\theta 2} \\
&= -\sin(\theta')\left(\frac{j\omega\mu_0 \cos\left(\theta_i^{image}\right)}{4\pi(x_R - h - \frac{L}{2})}\right)\left(\frac{1+\Gamma}{e^{+jk_{x1}h} + \Gamma_2 e^{-jk_{x1}h}}\right) \\
&\quad \left(1+\Gamma_2\right) e^{+jk_{z0}h} e^{-jk_0 r'},
\end{aligned}
\tag{A.15}
$$

where r' is the direct distance from image target to receiver *b*.

C) Combining the two electric fields

We transfer the two electric fields back into one coordinate system:

$$
\begin{aligned}
E'_{\theta} = {} & \hat{x}(E_{\theta 1}\cos(\phi)\cos(\theta) + E_{\theta 2}\cos(\phi)\cos(\theta')) + \\
& \hat{y}(E_{\theta 1}\sin(\phi)\cos(\theta) + E_{\theta 2}\sin(\phi)\cos(\theta')) - \\
& \hat{z}(E_{\theta 1}\sin(\theta) + E_{\theta 2}\sin(\theta')),
\end{aligned}
\tag{A.16}
$$

where $\phi = \arctan\left(\frac{y_0 - y_R}{x_0 - x_R}\right)$. Hence, the final transfer function is:

$$
T = E'_z = -(E_{\theta 1}\sin(\theta) + E_{\theta 2}\sin(\theta')). \tag{A.17}
$$

For simplicity, since the receivers are put far away from the wall, the height of the receivers and target can be ignored; thus the transfer function is simplified into:

$$
\begin{aligned}
T(\omega, \underline{r}, \underline{r}') = -2 & \left(\frac{j\omega\mu_0 \cos(\theta_i)}{4\pi(x_R - h - \frac{L}{2})}\right)\left(\frac{1+\Gamma}{\mathrm{e}^{+jk_{x1}h} + \Gamma_2 \mathrm{e}^{-jk_{x1}h}}\right) \\
& \left(1+\Gamma_2\right)\mathrm{e}^{+jk_{x0}h}\mathrm{e}^{-jk_0 r}.
\end{aligned}
\tag{A.18}
$$

A.2 Transfer Function for The Single-Wall Model: SDI Method

For convenience, we change the location expression to be: target *a* (x_a , y_a, z_a), receiver *b* (x_b , y_b, z_b). We use reciprocity first, then rotate the coordinates and change the origin position as shown in Fig. A.6. Hence, $x_R = z_b$, $y_R = -y_b$, $z_R = x_b - L/2 - h$; $x_0 = z_A$, $y_0 = -y_a$, $z_0 = x_a - L/2 - h$. Here *L* is enclosed area's length.

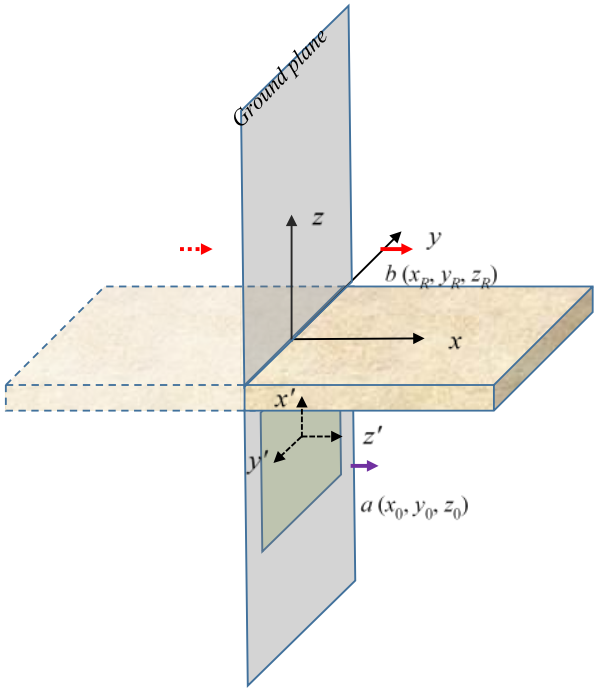

Figure A.6. 3D view of the geometry after applying the reciprocity theorem under the new coordinate system.

In the new coordinate system, the current source can be represented as

$$\underline{J}_s\,|_{z=z_R} = \underline{\hat{x}} Il\delta\left(x-x_R\right)\left(y-y_R\right). \tag{A.19}$$

After taking into consideration the ground effect, the current source is

$$\underline{J}_s\,|_{z=z_R} = \underline{\hat{x}}\left(Il\delta\left(x-x_R\right)\delta\left(y-y_R\right)+Il\delta\left(x+x_R\right)\delta\left(y-y_R\right)\right). \tag{A.20}$$

The finite current sheet can then be represented as a set of infinite phased current sheets as

$$\underline{J}_s\left(x,y\right)=\frac{1}{\left(2\pi\right)^2}\int_{-\infty}^{+\infty}\int_{-\infty}^{+\infty}\underline{\tilde{J}}_s\left(k_x,k_y\right)e^{-j\left(k_x x+k_y y\right)}dk_x dk_y. \tag{A.21}$$

Assume that

$$\underline{J}_s^p\left(x,y\right)=\underline{J}_{s0}^p\,e^{-j\left(k_x x+k_y y\right)}, \tag{A.22}$$

where

$$\underline{J}_{s0}^{p} = \frac{1}{(2\pi)^2}\underline{\tilde{J}}_s\left(k_x, k_y\right)dk_x dk_y. \tag{A.23}$$

Then the phased current sheet launches a pair of plane wave as shown in Fig. A.7.

In the space domain,

$$\begin{aligned}\underline{\tilde{J}}_s\left(k_x, k_y\right)|_{z=z_R} &= \int_{-\infty}^{+\infty}\int_{-\infty}^{+\infty}\underline{J}_s e^{j\left(k_x x + k_y y\right)}dxdy \\ &= \int_{-\infty}^{+\infty}\int_{-\infty}^{+\infty}\underline{\hat{x}}\begin{pmatrix} Il\delta\left(x - x_R\right)\delta\left(y - y_R\right) \\ +Il\delta\left(x + x_R\right)\delta\left(y - y_R\right)\end{pmatrix}e^{j\left(k_x x + k_y y\right)}dxdy \\ &= \underline{\hat{x}}2\cos\left(k_x x_R\right)e^{jk_y y_R}.\end{aligned} \tag{A.24}$$

We insert (A.24) into $\underline{J}_{s0}^{p}$, and obtain $\underline{J}_{s0}^{p}|_{z=z_R} = \underline{\hat{x}}\frac{1}{2\pi^2}\cos\left(k_x x_R\right)e^{jk_y y_R}dk_x dk_y$; thus the phased current sheet can be represented as

$$\begin{aligned}\underline{J}_s^{p}\left(x, y\right)|_{z=z_R} &= \underline{J}_{s0}^{p}|_{z=z_R}\ e^{-j\left(k_x x + k_y y\right)} \\ &= \underline{\hat{x}}\frac{1}{2\pi^2}\cos\left(k_x x_R\right)e^{-j\left(k_x x + k_y\left(y - y_R\right)\right)}dk_x dk_y.\end{aligned} \tag{A.25}$$

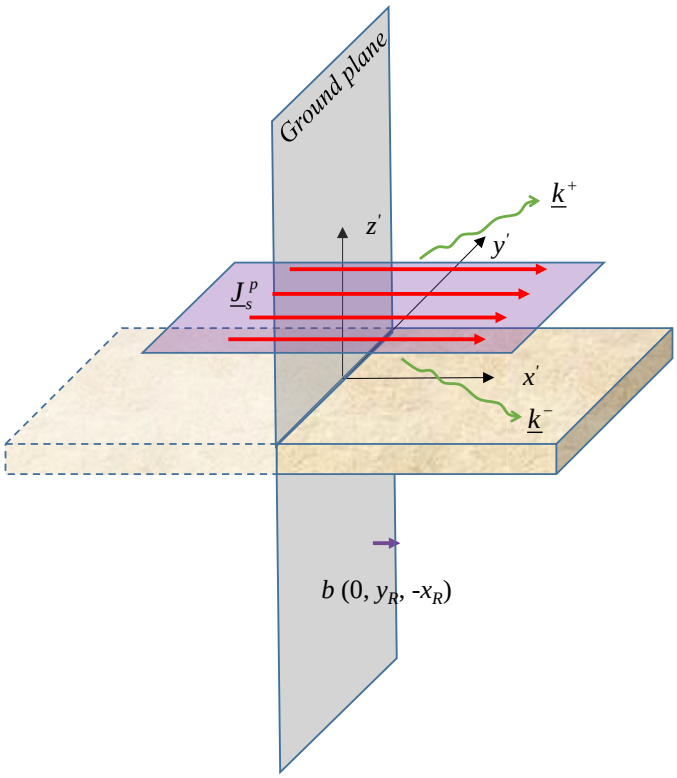

Figure A.7. Equivalent finite current sheet configuration.

The next step is to decompose the current into two parts, which excite the TM_z and TE_z waves, respectively:

$$\underline{J}_s^p(x,y) = \underline{\hat{u}} J_{su}^p(x,y) + \underline{\hat{v}} J_{su}^p(x,y), \tag{A.26}$$

where J_{su}^p launches a TM_z wave, and J_{sv}^p launches a TE_z wave. The definition of $\underline{\hat{u}}$ and $\underline{\hat{v}}$ is shown in Fig. A.8, and $\overline{\phi} = \arccos\left(\frac{k_x}{k_t}\right)$.

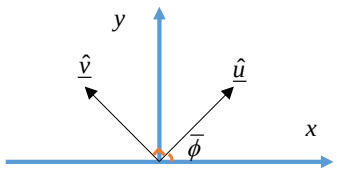

Figure A.8. Definition of unit vectors.

A) Transverse fields under TM_z excitation

Figure A.9 shows the transverse equivalent network of the entire system under TM_z excitation.

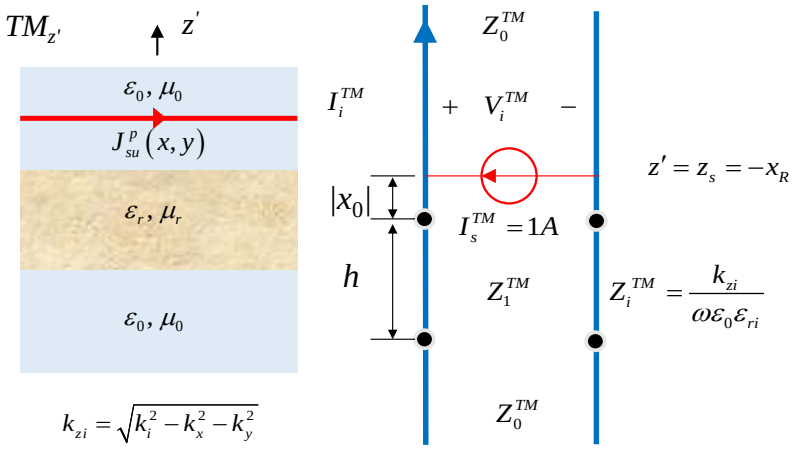

Figure A.9. Transverse equivalent network for TM_z excitation.

The transverse fields can be expressed as

$$\begin{aligned}
\underline{E}_t &= \underline{\hat{u}} E_u(x,y,z) = \underline{\hat{u}} E_{u0}(z) e^{-j(k_x x + k_y y)} \\
&= \underline{\hat{u}} V^{TM}(z) e^{-j(k_x x + k_y y)} \\
\underline{H}_t &= \underline{\hat{v}} H_v(x,y,z) = \underline{\hat{v}} H_{v0}(z) e^{-j(k_x x + k_y y)} \\
&= \underline{\hat{v}} I^{TM}(z) e^{-j(k_x x + k_y y)},
\end{aligned} \tag{A.27}$$

where $E_u = V_i^{TM}(z)\left(-\underline{J}_{s0}^p \cdot \underline{\hat{u}}\right) e^{-j(k_x x + k_y y)}$ and $E_u = H_v = I_i^{TM}(z)\left(-\underline{J}_{s0}^p \cdot \underline{\hat{u}}\right) e^{-j(k_x x + k_y y)}$. The characteristic impedances of the network (shown in Fig. A.9) are

$$\begin{aligned}
Z_0^{TM} &= \frac{k_{z0}}{\omega\varepsilon_0} \quad Z_1^{TM} = \frac{k_{z1}}{\omega\varepsilon_0\varepsilon_{rc}} \\
Z_{in1} &= Z_1^{TM} \frac{Z_0^{TM} + jZ_1^{TM} \tan k_{z1} h}{Z_1^{TM} + jZ_0^{TM} \tan k_{z1} h} \\
Z_{in} &= Z_0^{TM} \frac{Z_{in1}^{TM} + jZ_0^{TM} \tan k_{z0} z_R}{Z_0^{TM} + jZ_{in1}^{TM} \tan k_{z0} z_R}.
\end{aligned} \tag{A.28}$$

The input voltage at position $z = z_R$ is then $V_i^{TM}\big|_{z=z_R} = Z_{in} \,\|\, Z_0^{TM}$.

The same process can be applied for the TE_z excitation.

B) Transverse fields under TE_z excitation

Figure A.10 shows the TEN under TE_z excitation. The transverse fields are:

$$\begin{aligned}
\underline{E}_t &= \underline{\hat{v}} E_v(x,y,z) \\
&= \underline{\hat{v}} E_{v0}(z) e^{-j(k_x x + k_y y)} \\
&= -\underline{\hat{v}} V^{TE}(z) e^{-j(k_x x + k_y y)} \\
\underline{H}_t &= \underline{\hat{u}} H_u(x,y,z) \\
&= \underline{\hat{u}} H_{u0}(z) e^{-j(k_x x + k_y y)} \\
&= \underline{\hat{u}} I^{TE}(z) e^{-j(k_x x + k_y y)},
\end{aligned} \tag{A.29}$$

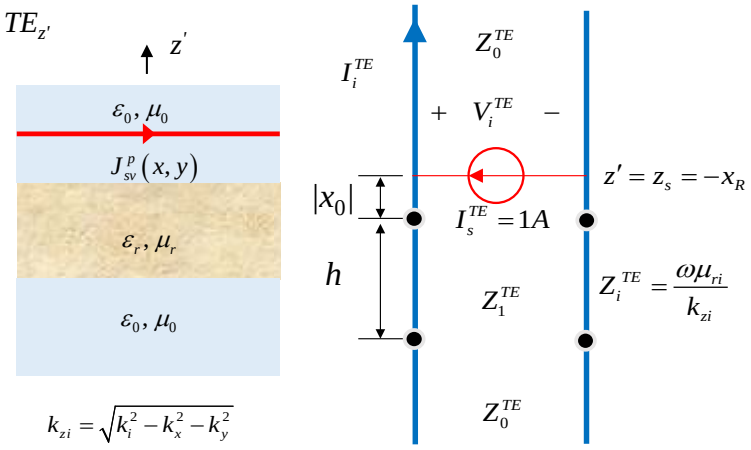

Figure A.10. Transverse equivalent network for TE_z mode.

where $E_v = -V_i^{TE}(z)\left(\underline{J}_{s0}^p \cdot \underline{\hat{v}}\right) e^{-j(k_x x + k_y y)}$ and $H_u = I_i^{TE}(z)\left(\underline{J}_{s0}^p \cdot \underline{\hat{v}}\right) e^{-j(k_x x + k_y y)}$. The characteristic impedances of the network are:

$$
\begin{aligned}
Z_0^{TE} &= \frac{\omega\mu_0}{k_{z0}} \quad Z_1^{TE} = \frac{\omega\mu_0}{k_{z1}} \\
Z_{in1} &= Z_1^{TE}\frac{Z_0^{TE} + jZ_1^{TE}\tan k_{z1}h}{Z_1^{TE} + jZ_0^{TE}\tan k_{z1}h} \\
Z_{in} &= Z_0^{TE}\frac{Z_{in1}^{TE} + jZ_0^{TE}\tan k_{z0}z_R}{Z_0^{TE} + jZ_{in1}^{TE}\tan k_{z0}z_R}.
\end{aligned}
\tag{A.30}
$$

The input voltage at position $z = z_R$ is then $V_i^{TE}\left(z_R\right) = Z_{in} \,||\, Z_0^{TE}$.

C) Transfer function

To get the transfer function, the $E_{z'}$ component should be determined; in the new coordinate system, $E_{z'} = E_x$. Combining both the *TE* mode and *TM* fields, we have

$$
\begin{aligned}
E_x &= E_u \cdot \left(\hat{\underline{u}} \cdot \hat{\underline{x}}\right) + E_v \cdot \left(\hat{\underline{v}} \cdot \hat{\underline{x}}\right) \\
&= E_u \cdot \frac{k_x}{k_t} - E_v \cdot \frac{k_y}{k_t} \\
&= \frac{1}{k_t}\left[k_x V_i^{TM}\left(z\right) I_s{}^{TM} + k_y V_i^{TE}\left(z\right) I_s{}^{TE}\right] e^{-j\left(k_x x + k_y y\right)} \\
&= -\frac{1}{k_t{}^2}\left[k_x{}^2 V_i^{TM}\left(z\right) + k_y{}^2 V_i^{TE}\left(z\right)\right] J_{sx0}^{p}\, e^{-j\left(k_x x + k_y y\right)}.
\end{aligned}
\tag{A.31}
$$

Using (A.23) (using the *x* component of the currents),

$$
\begin{aligned}
E_x &= \frac{1}{\left(2\pi\right)^2}\int_{-\infty}^{\infty}\int_{-\infty}^{\infty} -\frac{1}{k_t{}^2}\tilde{J}_{sx}\left[k_x{}^2 V_i^{TM}\left(z\right) + k_y{}^2 V_i^{TE}\left(z\right)\right] e^{-j\left(k_x x + k_y y\right)} dk_x dk_y \\
&= \frac{1}{2\left(\pi\right)^2}\int_{-\infty}^{\infty}\int_{-\infty}^{\infty} -\frac{1}{k_t{}^2}\cos\left(k_x x_R\right)\left[k_x{}^2 V_i^{TM}\left(z\right) + k_y{}^2 V_i^{TE}\left(z\right)\right] \\
&\qquad\qquad \cdot e^{-j\left(k_x x + k_y\left(y - y_R\right)\right)} dk_x dk_y.
\end{aligned}
\tag{A.32}
$$

The transfer function equals E_x when the equivalent source is an electric dipole; thus, transferring back to the original coordinate system yields

$$T=-\int_{-\infty}^{\infty}\int_{-\infty}^{\infty}\frac{\cos\left(k_x x_R\right)}{2\pi^2 k_t^{\,2}}\left[k_x^2 V_i^{TM}\left(z\right)+k_y^2 V_i^{TE}\left(z\right)\right]\cdot e^{-j\left(k_x x+k_y\left(y-y_R\right)\right)}\,dk_x dk_y$$
$$=-\int_{-\infty}^{\infty}\int_{-\infty}^{\infty}\frac{\cos\left(k_x z_b\right)}{2\pi^2 k_t^{\,2}}\begin{bmatrix}k_x^2 V_i^{TM}\left(x'-L/2-h\right)\\+k_y^2 V_i^{TE}\left(x'-L/2-h\right)\end{bmatrix}\cdot e^{-j\left(k_x z'+k_y\left(-y'+y_b\right)\right)}dk_x dk_y. \tag{A.33}$$

At the target's position, the transfer function should be in form

$$T\left(x_a,y_a,z_a\right)=-\int_{-\infty}^{\infty}\int_{-\infty}^{\infty}\frac{\cos\left(k_x z_b\right)}{2\pi^2 k_t^{\,2}}\left[k_x^2 V_i^{TM}\,|_{z=z_0}+k_y^2 V_i^{TE}\,|_{z=z_0}\right]\cdot e^{-j\left(k_x z_a+k_y\left(-y_a+y_b\right)\right)}dk_x dk_y. \tag{A.34}$$

Inside this transfer function, $V_i^{TM/TE}\,|_{z=z_0}$ can be calculated by using ABCD matrix, as shown in Fig. A.11.

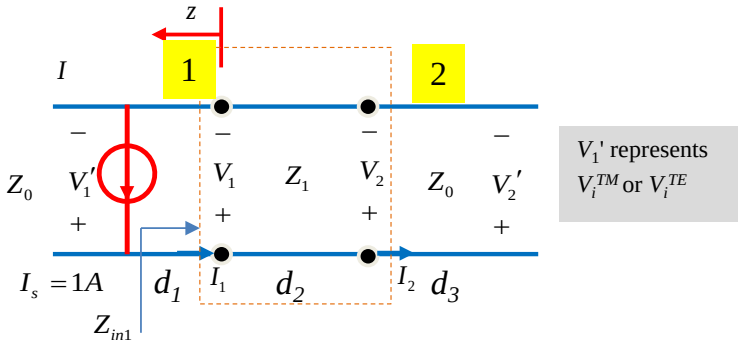

Figure A.11. ABCD matrix calculation.

In this transmission line, input and output voltage can be related by the ABCD matrix as

$$\begin{bmatrix}V_1\\I_1\end{bmatrix}=\begin{bmatrix}A & B\\C & D\end{bmatrix}\begin{bmatrix}V_2\\I_2\end{bmatrix}, \tag{A.35}$$

where

$$A=\left.\frac{V_1}{V_2}\right|_{I_2=0}=\cosh\left(jk_{z1}h\right)\quad B=\left.\frac{V_1}{I_2}\right|_{V_2=0}=Z_1\sinh\left(jk_{z1}h\right),$$
$$C=\left.\frac{I_1}{V_2}\right|_{I_2=0}=\frac{\sinh\left(jk_{z1}h\right)}{Z_1}\quad D=\left.\frac{I_1}{I_2}\right|_{V_2=0}=\cosh\left(jk_{z1}h\right)\quad . \tag{A.36}$$

The reflection coefficient at port 1 is

$$\Gamma'=\frac{Z_{in1}-Z_0}{Z_{in1}+Z_0}. \tag{A.37}$$

The current at port 1 is

$$I_1=\frac{V_1}{Z_{in1}}. \tag{A.38}$$

According to transmission line theory, the voltage at port 1 is

$$\begin{aligned}V_1&=V_1'e^{-jk_{z0}d_1}\left(1+\Gamma'\right)\\&=Z_{in}\,\|\,Z_0e^{-jk_{z0}d_1}\left(1+\Gamma'\right).\end{aligned} \tag{A.39}$$

Under *TE* excitation, inserting (A.39), (A.38), (A.30) , (A.36) into (A.35) will yield V_2, and the voltage at the target's position is calculated by using

$$V_2'=V_i^{TM/TE}\,|_{z=z_0}=V_2e^{-jk_{z0}d_3}=V_2e^{-jk_{z0}\left(L/2-x_a\right)}. \tag{A.40}$$

D) Calculation of 2D integrations

As seen in the transfer function, the integration range is from -∞ to +∞ in both the k_x and k_y variables. To shorten the integration time, we transfer the integrand from k_x and k_y into k_t and $\overline{\phi}$ using

$$k_x=\cos\left(\overline{\phi}\right)k_t,\quad k_y=\sin\left(\overline{\phi}\right)k_t. \tag{A.41}$$

In order to overcome the problem of singularities encountered during the integration, the Gaussian quadrature method is applied, and the integration path is redefined as in Fig.

A.12, in which Section 2 is the most important section, and decides the integration accuracy.

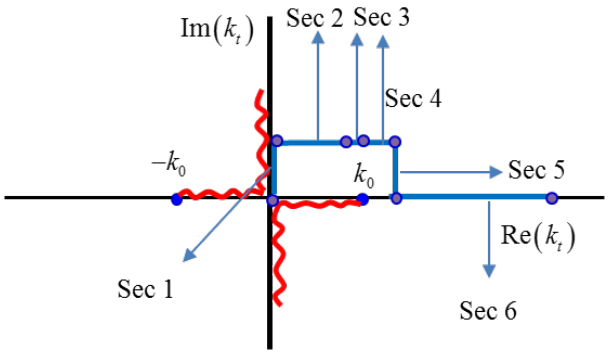

Figure A.12. Integration path in the k_t domain.

A.3 Transfer Function for The 2D Single-Wall Model: SDI Method

The derivation of the 2D single-wall model's transfer function is the same as in Section A.2; the only difference is the current source. In this case, the source is no longer an electric dipole, but an infinite current source. The expression of the current source becomes

$$\underline{J}_s\big|_{z=z_R} = \hat{\underline{x}} I \delta\left(y - y_R\right). \tag{A.42}$$

The finite current sheet can then be represented as a set of infinite phased current sheets as

$$\underline{J}_s\left(x,y\right) = \frac{1}{\left(2\pi\right)^2}\int_{-\infty}^{+\infty}\int_{-\infty}^{+\infty} \tilde{\underline{J}}_s\left(k_x,k_y\right) e^{-j\left(k_x x + k_y y\right)} dk_x dk_y. \tag{A.43}$$

We denote

$$\underline{J}_s^p\left(x,y\right) = \underline{J}_{s0}^p\, e^{-j\left(k_x x + k_y y\right)}, \tag{A.44}$$

where

$$\underline{J}_{s0}^{p} = \frac{1}{(2\pi)^2}\tilde{\underline{J}}_s\left(k_x, k_y\right)dk_x dk_y. \tag{A.45}$$

Then the phased current sheet launches a pair of plane wave as was shown in Fig. A.7. In the space domain,

$$\begin{aligned}\tilde{\underline{J}}_s\left(k_x, k_y\right)|_{z=z_R} &= \int_{-\infty}^{+\infty}\int_{-\infty}^{+\infty}\underline{J}_s e^{j\left(k_x x + k_y y\right)}dxdy \\ &= \int_{-\infty}^{+\infty}\int_{-\infty}^{+\infty}\hat{\underline{x}}\left(I\delta\left(y - y_R\right)\right)e^{j\left(k_x x + k_y y\right)}dxdy \\ &= \hat{\underline{x}}2\pi I\delta\left(k_x\right)e^{jk_y y_R}.\end{aligned} \tag{A.46}$$

Inserting (A.46) into $\underline{J}_{s0}^{p}$ yields $\underline{J}_{s0}^{p}|_{z=z_R} = \hat{\underline{x}}\frac{I}{2\pi}\delta\left(k_x\right)e^{jk_y y_R}dk_x dk_y$; thus the phased current sheet can be represented as

$$\begin{aligned}\underline{J}_s^{p}\left(x, y\right)|_{z=z_R} &= \underline{J}_{s0}^{p}|_{z=z_R}\ e^{-j\left(k_x x + k_y y\right)} \\ &= \hat{\underline{x}}\frac{I}{2\pi}\delta\left(k_x\right)e^{-j\left(k_x x + k_y\left(y - y_R\right)\right)}dk_x dk_y.\end{aligned} \tag{A.47}$$

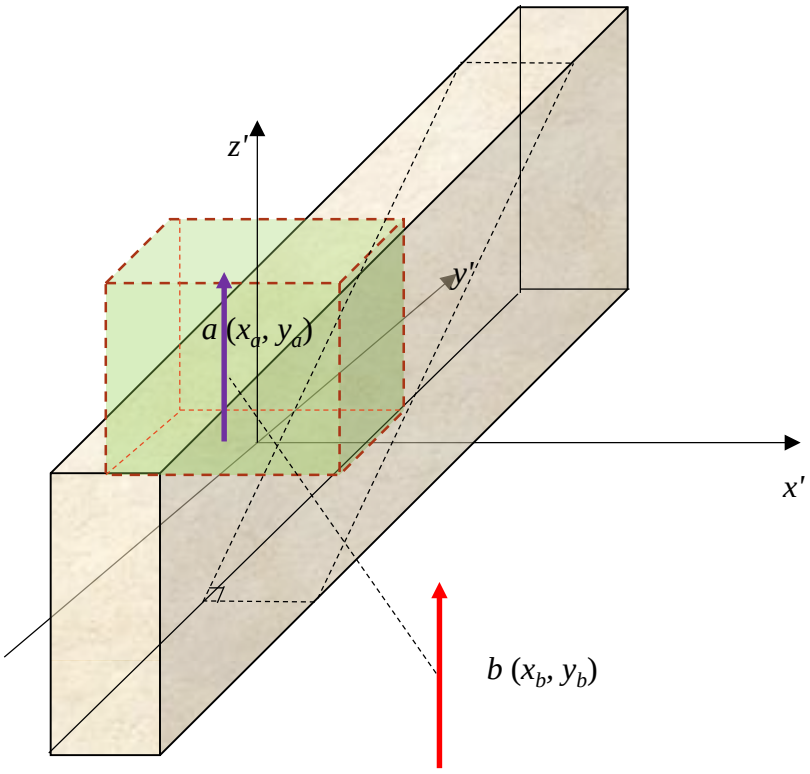

Figure A.13. 2D single-wall model.

The rest of the derivation is the same as in Section A.2. We can obtain E_x by using

$$\begin{aligned} E_x &= \frac{1}{(2\pi)^2}\int_{-\infty}^{\infty}\int_{-\infty}^{\infty} -\frac{1}{k_t^{\,2}}\tilde{J}_{sx}\left[k_x^2 V_i^{TM}(z) + k_y^2 V_i^{TE}(z)\right] \\ &\qquad \cdot e^{-j\left(k_x x + k_y y\right)} dk_x dk_y \\ &= \frac{I}{2\pi}\int_{-\infty}^{\infty}\int_{-\infty}^{\infty} -\frac{1}{k_t^{\,2}}\delta(k_x)\left[k_x^2 V_i^{TM}(z) + k_y^2 V_i^{TE}(z)\right] \\ &\qquad \cdot e^{-j\left(k_x x + k_y (y - y_R)\right)} dk_x dk_y . \end{aligned} \tag{A.48}$$

The transfer function equals E_x when the equivalent source is an electric dipole; thus transferring back to the original coordinate system yields

$$
\begin{aligned}
T &= -\int_{-\infty}^{\infty}\int_{-\infty}^{\infty} \frac{\delta(k_x)}{2\pi k_t^{\,2}}\left[k_x^2 V_i^{TM}(z) + k_y^2 V_i^{TE}(z)\right] \\
&\qquad \cdot e^{-j\left(k_x x + k_y (y - y_R)\right)} dk_x dk_y \\
&= -\int_{-\infty}^{\infty} \frac{1}{2\pi k_t^{\,2}}\left[k_y^2 V_i^{TE}(x' - L/2 - h)\right] \\
&\qquad \cdot e^{-jk_y(-y' + y_b)} dk_y .
\end{aligned}
\tag{A.49}
$$

At the target's position ($k_x = 0$ means $\bar{\phi} = \pi/2$ or $3\pi/2$, and hence $k_y = k_t$), the transfer function is

$$
\begin{aligned}
T(x_a, y_a, z_a) &= -\int_{-\infty}^{\infty} \frac{k_y^2 V_i^{TE}\,|_{x'=x_a}}{2\pi k_t^{\,2}} e^{-jk_y(-y_a + y_b)} dk_y \\
&= -\int_0^{\infty} \frac{V_i^{TE}\,|_{x'=x_a}}{2\pi} e^{-jk_t(-y_a + y_b)} dk_t \\
&\quad -\int_0^{\infty} \frac{V_i^{TE}\,|_{x'=x_a}}{2\pi} e^{+jk_t(-y_a + y_b)} dk_t .
\end{aligned}
\tag{A.50}
$$